Title
Unveiling Supermassive Black Hole Growth and Co-Evolution Using X-rays

Permalink
https://escholarship.org/uc/item/9g80z3bj

Author
Saade, Mary Lynne

Publication Date
2023

UNIVERSITY OF CALIFORNIA
Los Angeles

Unveiling Supermassive Black Hole Growth and Co-Evolution Using X-rays

A dissertation submitted in partial satisfaction
of the requirements for the degree
Doctor of Philosophy in Astronomy and Astrophysics

by

Mary Lynne Saade

2023

ABSTRACT OF THE DISSERTATION

Unveiling Supermassive Black Hole Growth and Co-Evolution Using X-rays

by

Mary Lynne Saade
Doctor of Philosophy in Astronomy and Astrophysics
University of California, Los Angeles, 2023
Professor Steven R. Furlanetto, Chair

Supermassive black holes (SMBHs) are thought to co-evolve alongside their host galaxies both through mergers with other SMBHs, and through accretion and the active galactic nucleus (AGN) emission it powers. Binary SMBHs are a step along the way to SMBH mergers, and so are important for understanding SMBH-galaxy co-evolution. Understanding the activity period of AGN (the AGN duty cycle) is also important for understanding how much of an impact AGN can have on their host galaxies. It is for these reasons in my thesis that I studied binary SMBHs and the AGN duty cycle. In my thesis I investigated whether candidate binary SMBHs had distinct spectra from single SMBHs, a phenomenon predicted by many theoretical models. I found that they do not, which could mean that the theoretical models are incorrect, or that the candidates were not truly binary SMBHs. This null result motivates additional theory development as well as future observational campaigns to find or confirm binary SMBHs. I also searched for recently deactivated AGN in a sample of obscured AGN, to see if that could shed light on the time periods over which AGN turn off and on. I found one AGN that deactivated no more than 87-220 years ago, indicating that perhaps AGN flicker on timescales of decades and centuries.

The dissertation of Mary Lynne Saade is approved.

Alice E. Shapley

Tomasso L. Treu

Matthew A. Malkan

Daniel Stern

Steven R. Furlanetto, Committee Chair

University of California, Los Angeles

2023

Dedicated to my parents, without whose support I would never have gotten this far. And to Daniel Stern, for being so kind and understanding to me, and rekindling my love of science.

TABLE OF CONTENTS

LIST OF FIGURES

LIST OF TABLES

ACKNOWLEDGMENTS

I once again want to thank Daniel Stern for his immense patience and willingness to see the good in me. And to Murray Brightman, too, for the same. I owe Thomas Connor a lot for his help on my *NuSTAR* proposal and on fixing my LaTeX code numerous times. I want to thank the coauthors on my papers for the advice they gave on improving them. Most of this thesis is from my papers, and I wouldn't have been able to make the papers as good as they could be without their input and feedback.

In addition to the people who helped me directly with my research, there are people who provided me with social and emotional support. I want to thank Veronica Dike for being a very good friend to me during my time here in graduate school. I also want to thank my family for cheering me on and always believing in me. Lastly I want to thank my life coach Joanne Rolston for all that she has done for me during these years. Her help has been immeasurable.

VITA

2014-2015	**Undergraduate Researcher**, Department of Physics and Astronomy, Rice University, Houston, TX
2015	**B.S., Astrophysics**, Rice University, Houston, TX
2015-2017, 2022	**Teaching Assistant**, Department of Physics and Astronomy, UCLA, Los Angeles, CA. Astronomy 5 – Life in the Universe (2015, 2016), Astronomy 3 - Nature of the Universe (2016, 2022), Physics 5C - Physics for Life Science Majors: Electricity, Magnetism, and Modern Physics lab (2017)
2016–present	**Graduate Student Researcher**, Department of Physics and Astronomy, UCLA, Los Angeles, CA
2017	**M.S., Astronomy**, UCLA, Los Angeles, CA
2017-2020	**Grader/Reader**, Department of Physics and Astronomy, UCLA, Los Angeles, CA. Astronomy 5 – Life in the Universe (2017, 2020), Physics 1A: Mechanics (2019), Physics 140A: Introduction to Solid State Physics (2017-2018)

PUBLICATIONS

The haloes and environments of nearby galaxies (HERON) - I. Imaging, sample characteristics, and envelope diameters

Rich, R. M. ; Mosenkov, A. ; Lee-Saunders, H.; Koch, A. ; Kormendy, J. ; Kennefick, J. ; Brosch, N. ; Sales, L. ; Bullock, J. ; Burkert, A. ; Collins, M. ; Cooper, M.; Fusco, M. ;

Reitzel, D. ; Thilker, D. ; Milewski, D. G. ; Elias, L. ; Saade, M. L. ; De Groot, L., 2019, MNRAS, 490, 2, id p.1539-1569

Chandra Observations of Candidate Subparsec Binary Supermassive Black Holes

Saade, M. L.; Stern, D.; Brightman, M.; Haiman, Z.; Djorgovski, S. G.; D'Orazio, D.; Ford, K. E. S.; Graham, M. J.; Jun, H. D.; Kraft, R. P.; McKernan, B.; Vikhlinin, A.; Walton, D., 2020, ApJ, 900, 2, id 148

NuSTAR Observations of AGNs with Low Observed X-Ray to [O III] Luminosity Ratios: Heavily Obscured AGNs or Turned-off AGNs?

Saade, M. L. ; Brightman, M. ; Stern, D. ; Malkan, M. ; García, J. A., 2022, ApJ, 936, 2, id 162

NuSTAR Observations of Candidate Supbarsec Binary Supermassive Black Holes

Saade, M. L.; Brightman, M.; Stern, D.; Connor, T.; Djorgovski, S. G.; D'Orazio, D.; Ford, K. E. S.; Graham, M. J.; Haiman, Z.; Jun, H. D.; Kammoun, E.; Kraft, R. P.; McKernan, B.; Vikhlinin, A.; Walton, D., arXiV: 2304.06144

Discovery of a Low-Redshift Hot Dust-Obscured Galaxy

Li, G.; Tsai, C-W.; Stern, D.; Wu, J.; Assef, R. J.; Blain, A. W.; Díaz-Santos, T.; Eisenhardt, P. R. M.; Griffith, R. L.; Jarret, T. H.; Jun, H. D.; Lake, S. E.; Saade, M. L., arXiV: 2305.13739

CHAPTER 1

Introduction

For several decades after they had been found as a solution to Einstein's field equations, black holes were considered theoretical objects. Today, we know that not only do black holes exist, but that enormous ones, millions to tens of billions the mass of the Sun, are present in the heart of most galaxies. This is one of the most important results of the past few decades in astrophysics.

The masses of these supermassive black holes (SMBHs) are known to be tightly correlated with many properties of their host galaxy, such as the velocity dispersion of the host galaxy bulge (the $M_{\rm BH} - \sigma$ correlation; e.g., Ferrarese & Merritt, 2000; Gebhardt et al., 2000; Kormendy & Ho, 2013), and the mass and luminosity of the host galaxy bulge (e.g, Merritt & Ferrarese, 2001; Marconi & Hunt, 2003; Kormendy & Ho, 2013; Saglia et al., 2016). These correlations are considered evidence for SMBHs co-evolving with their host galaxies. That is, both galaxy and SMBH grow together, with each potentially influencing the other in turn. This would mean that understanding SMBH growth and evolution is essential for providing a complete picture of how galaxies themselves have formed and evolved, and hence, important for understanding our own origins as well.

1.1 Black Hole Merger-Induced Growth and Co-evolution

One possible reason for co-evolution between SMBHs and their host galaxies is galaxy mergers. When two galaxies merge, their respective black holes will sink to the center of the merged galaxy on the timescale of a few billion years due to dynamical friction (Bogdanović et al., 2022). These SMBHs can then pair up into binaries. The binary separation will shrink over time through interactions with the merged galaxy's stars and gas until they reach sub-parsec separations. Then, the binary can further shrink by releasing gravitational waves, eventually leading to the two black holes coalescing (Begelman et al., 1980). Galaxy bulges are thought to be built over time by galaxy mergers (Kormendy & Ho, 2013; Saglia et al., 2016) so in this manner the merger will result in both a larger galaxy bulge and a larger SMBH, helping to create the correlations observed.

Jahnke & Macciò (2011) argued that repeated dry (i.e. gasless) galaxy mergers can explain the correlations alone, with only SMBH mergers being the source of SMBH growth and no need for SMBH accretion. Mergers between galaxies' central black holes likely plays a role in the early growth of SMBHs (e.g., Volonteri et al., 2003; Sesana et al., 2007; Dayal et al., 2019; Piana et al., 2021). The IllustrisTNG simulation (Weinberger et al., 2018) shows that black holes with masses greater than $10^{8.5}$ $M_\odot$ grow beyond this mass primarily by mergers with other SMBHs. However, the majority of SMBH growth since $z \sim 1$ happens through accretion of gas unrelated to mergers (Cisternas et al., 2011), and the total energy release of quasars is evidence that most SMBH growth is through accretion (Soltan, 1982). Furthermore, observations of the early Universe indicate that bulges and their SMBHs grow in lockstep, something difficult to accomplish from random mergers alone (Yang et al., 2019). Therefore, significant evidence shows that SMBH mergers cannot explain the entirety of SMBH growth and co-evolution (Hirschmann et al., 2010), though they play an important role.

1.1.1 Binary SMBHs

Binary SMBHs are an essential step along the process to SMBH mergers. Understanding them is therefore key to understanding how SMBHs merge, and hence how they grow along with their galaxies. Finding and confirming binary SMBHs would also help constrain galaxy evolution models, which predict that binary SMBHs should be be fairly ubiquitous ($\sim 1\%$ of AGN at $z < 0.6$; Kelley et al., 2019).

There have been both observational and theoretical difficulties in understanding binary SMBHs. For one thing, two black holes cannot merge through gravitational radiation on timescales shorter than the age of the Universe until they reach subparsec separations ($10^{-2} - 10^{-3}$ pc; Bogdanović et al., 2022). However, many early theoretical studies indicated that when the two black holes sink to the center of the merged galaxy, their separation will stall out and fail to shrink to a scale where gravitational radiation becomes important (the "final parsec problem"; Milosavljević & Merritt, 2003; Makino & Funato, 2004). It is unknown precisely how SMBH binaries shrink below parsec scales, but gas dynamics (Mayer et al., 2007), non-spherically-symmetric distributions of stars (Gualandris et al., 2017), and multi-body interactions with other SMBHs (Ryu et al., 2018) could play a role. In particular, triaxial star distributions can lead to binary SMBH formation and coalescence on a timescale of a few hundred million years (Khan et al., 2018).

Observations of binary SMBHs would help resolve this puzzle, but until recently, few candidates were known. For many decades the only robust candidate binary SMBH was the blazar OJ 287, which displays optical flares every 11 years (Lehto & Valtonen, 1996). Valtonen et al. (2012) show that this behavior is consistent with a $1.4 \times 10^8\,M_\odot$ secondary SMBH repeatedly plunging through the accretion disk of a $1.8 \times 10^{10}\,M_\odot$ primary SMBH. This model was used to predict the timing of the flare in 2019 with a precision of 3 hours (Laine et al., 2020). It should be noted, however, that a predicted October 2022 outburst failed to materialize, suggesting the masses of the component black holes are significantly lower than this, though a binary explanation is still favored (Komossa et al., 2023). While OJ 287 remains the strongest candidate binary SMBH to date, many more candidates have since been identified. Some of the best candidates are active galactic nuclei (AGN) with periodic lightcurves. There are many ways periodicity can arise in a binary SMBH, such as through Doppler effects and relativistic beaming of one black hole's accretion flow as it goes around the other black hole (e.g., D'Orazio et al., 2015b), oscillations in accretion between the primary and secondary black hole (D'Orazio et al., 2013; Farris et al., 2014; Shi & Krolik, 2015), and gravitational lensing of one black hole's accretion flow by the other (Haiman, 2017; D'Orazio & Di Stefano, 2018) . In contrast, few if any plausible explanations for periodicity without invoking binarity have been identified; for instance, Lense-Thirring precession would be damped on timescales shorter than the AGN lifetime (Graham et al., 2015b).

Identifying candidate binary SMBHs is challenging. AGN are known to vary stochastically. The power spectrum of these fluctuations is broad, with the power increasing at low frequencies ("red noise"). This spectrum is often approximated as a power law, $P(f) \propto f^{-\alpha}$, with $\alpha \gtrsim 1$ over long timescales (Vaughan, 2012). Red noise can generate apparent periodicity when there is none (Vaughan et al., 2016), leading to false claims of periodicity in an AGN's light curve even for well-sampled data if the number of period cycles is small and the false alarm probability is improperly calculated (Barth & Stern, 2018). This is the case for many binary SMBH candidates reported to date.

Theoretical models of accreting binary SMBHs are also challenging. Initial attempts to investigate binary SMBHs assumed axisymmetry, and concluded that the larger scale accretion flow would not reach the individual SMBHs (e.g. Armitage & Natarajan, 2002; Chang et al., 2010; Kocsis et al., 2012b,a; Rafikov, 2013). However, later models found that relaxing this assumption allowed the SMBHs to accrete at rates similar to a single SMBH in a regular AGN (e.g. Baruteau et al., 2012; D'Orazio et al., 2013; Farris et al., 2014; Shi & Krolik, 2015).

Models are in general agreement that the two black holes are surrounded by a circumbinary disk, from which accretion streams feed onto mini-disks surrounding each individual black hole. In the interior of the circumbinary disk, a cavity is cleared out by tidal torques from the binary (Artymowicz & Lubow, 1994, see Figure 1.1). Some of the material that falls into the cavity is flung back out by the binary, creating an overdense lump at the inner edge of the circumbinary disk that can cause periodic modulations of the accretion rate into the cavity (e.g. Noble et al., 2012; Shi et al., 2012; Farris et al., 2014; Gold et al., 2014). There can also be transfer of material between the two mini-disks at peribothron (Bowen et al., 2017). Periodic signals identified by observers are expected to come primarily from mini-disk emission (Bogdanović et al., 2022), through accretion rate modulations, Doppler shifts, and self-lensing. However, it is unclear what fractions of the emitted radiation comes from the mini-disks, accretion streams, and circumbinary disks. Naïvely, one would expect the mini-disks to dominate the luminosity as they reach down to the innermost stable circular orbit (ISCO) where more of the infalling energy can be converted into radiation. However, the mini-disks might contribute only a small fraction of the total luminosity (e.g. d'Ascoli et al., 2018) and only might be 25-75% as radiatively efficient as accretion disks around single SMBHs (Bogdanović et al., 2022). Roedig et al. (2014) also investigated how accretion streams striking the mini-disks might contribute a significant portion of the hard X-ray spectrum, though Bogdanović et al. (2022) noted that given their further distance from the black hole, this mechanism might be subdominant . It is clear that much uncertainty still remains in modeling the radiative emissions of binary SMBHs, and new observations are essential to test theoretical models and better motivate theory development. It is for this reason that we investigate observations of candidate binary SMBHs in Chapters 2 and 4.

1.2 Accretion-Induced Growth and Co-evolution

When SMBHs accrete matter, they can convert a substantial fraction of the input mass into energy. A typical SMBH is around a thousandth the mass of its host galaxy, and assuming a

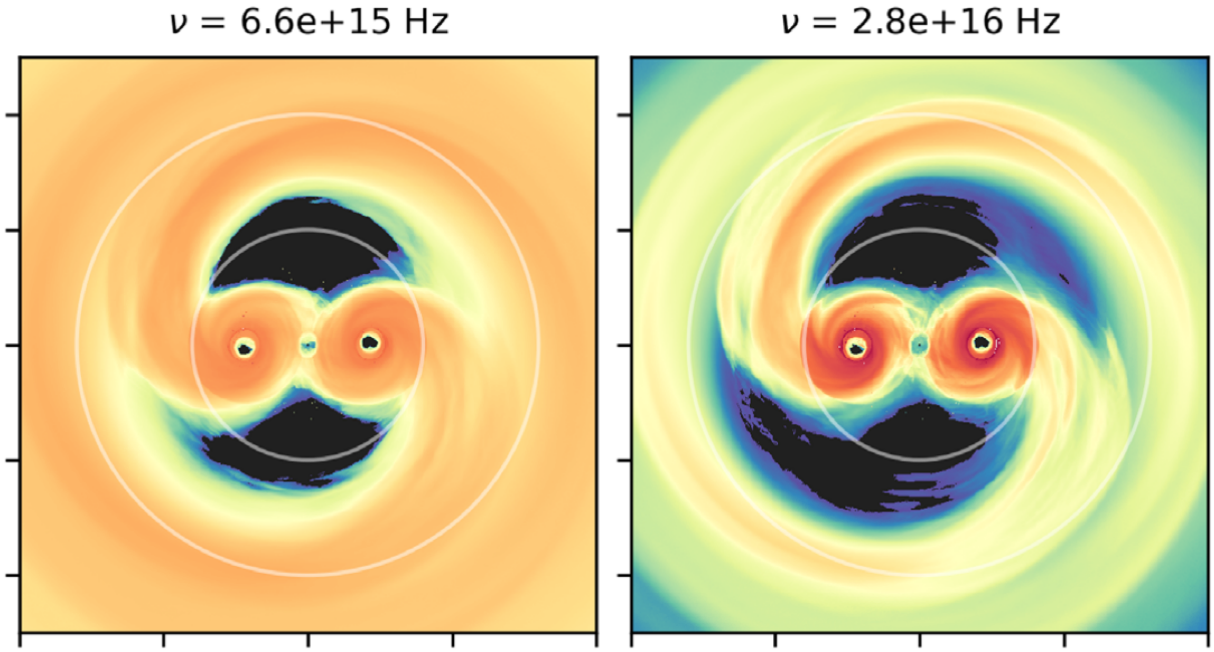

Figure 1.1 Snapshots of the radiative emission of a model binary SMBH at different frequencies. The panel on the left shows far UV emission (455 Å). The panel on the right shows soft X-ray emission (0.12 keV). The circumbinary disk surrounds a central cavity. Within the cavity, the two SMBHs orbit, each surrounded by a mini-disk. The mini-disks are connected to the circumbinary disk by accretion streams. Modified from Figure 8 in d'Ascoli et al. (2018). ©AAS. Reproduced with permission.

radiative efficiency of 10%, the total energy release $0.1\,M_{\rm BH}\,c^2$ of an SMBH's growth exceeds the host galaxy binding energy by a factor of 80 (Fabian, 2012). This strongly implies that AGN have significant influence on their host galaxies, a process termed AGN feedback. Such feedback is one likely way to create the observed correlations between SMBH mass and host galaxy properties (Kormendy & Ho, 2013), and is a necessary process to create the 'red and dead' elliptical galaxies in merger simulations (Di Matteo et al., 2005; Springel et al., 2005).

There are two main kinds of feedback: radiative and kinetic (Alexander & Hickox, 2012). The former is thought to dominate in very luminous AGN (i.e. quasars), and consists of radiation-pressure induced winds. In this picture, the AGN's radiation ionizes and pushes away dust grains, which couple to partially ionized gas and drive it out of the galaxy in a powerful outflow (Ishibashi & Fabian, 2016), leaving behind a galaxy without the cold gas necessary for star formation (Hopkins et al., 2008). This stifles accretion onto the SMBH and quenches star formation, setting limits on the SMBH mass and the size of the host galaxy spheroid (e.g., Steinborn et al., 2015; Hopkins et al., 2016). Radiative feedback is often invoked as a natural aspect of the galaxy merger process, where gas and dust are funneled onto the central SMBH by tidal torques from the merger, both triggering an AGN and obscuring it (e.g., Hopkins et al., 2008; Blecha et al., 2018). The AGN then blows out the dust and becomes visible as a bright quasar.

The primary observational evidence for radiative AGN feedback is outflows too high in velocity to be explained by stellar feedback (i.e., $> 500\,{\rm km\,s^{-1}}$), as measured using absorption lines on the AGN continuum (Fabian, 2012). Some AGN outflows are truly extreme, with line of sight velocities exceeding 10,000 $\rm km\,s^{-1}$ (i.e., ultra-fast outflows, or UFOs; Tombesi et al., 2013) or mass removal rates approaching $1200\,M_\odot\,{\rm yr}^{-1}$ (Sturm et al., 2011).

Kinetic feedback is thought to dominate in low-luminosity AGN, such as radio galaxies. In this case the energy is delivered to the galaxy's circumgalactic medium through relativistic jets. These jets heat up the circumgalactic medium, preventing it from cooling down and falling back onto the galaxy to form stars. Because a low-luminosity AGN can be triggered by even a small amount of cold gas accreting onto the galaxy, this process is a regulatory mechanism that stops a galaxy from being able to form stars after it has already been quenched (Fabian, 2012).

The primary observational evidence for kinetic feedback is the presence of cavities and shocks in the X-ray emitting gas of massive galaxies, galaxy clusters, and groups (e.g., Fabian et al., 2006; Dunn & Fabian, 2008; Shin et al., 2016). These cavities are often filled with radio lobes and so are believed to have been carved by the jets from a central radio galaxy (Dunn & Fabian, 2008). For example, the cavities in the galaxy cluster MS0735.6+7421 are larger in size than the Milky Way and imply an outburst of 10^{62} erg of energy (McNamara et al., 2009).

While AGN feedback is generally thought to be negative in nature (i.e. it stops galaxies from forming new stars), examples of positive feedback are also known, such as Minkowski's object, a starburst triggered by an AGN jet (van Breugel et al., 1985; Croft et al., 2006), and the core of the Seyfert galaxy NGC 5643, which contains stars apparently formed by winds from the AGN (Cresci et al., 2015). Some theoretical models reinforce the idea that AGN jets and outflows can compress and fragment gas within galaxies, thereby triggering star formation (e.g. Gaibler et al., 2012; Bieri et al., 2016; Zubovas & Bourne, 2017).

The case for AGN feedback is strong, given the energy that SMBHs are observed to deposit into their host galaxies. However, it is clear that this feedback is complicated and still not fully understood given that it can have both positive and negative effects. It remains uncertain whether AGN feedback is the dominant cause for the observed SMBH-galaxy correlations. These correlations could be primarily explained through galaxy mergers growing the black hole and the galaxy at the same time without a direct causal link (e.g. Hirschmann et al., 2010; Jahnke & Macciò, 2011). AGN feedback is also likely to be different in magnitude and timing for early-type and late-type galaxies (Schawinski et al., 2014).

1.2.1 AGN Duty Cycles

Understanding how long AGN are active, and hence how long they can impact their host galaxies, is essential for understanding SMBH-galaxy co-evolution. If SMBHs grow most of their mass through AGN accretion (the Soltan argument; Soltan, 1982), the observed spatial density of quasars implies that the total amount of time an SMBH spends in an AGN state is $10^7 - 10^9$ years (Yu & Tremaine, 2002; Marconi et al., 2004). However this does not constrain how the activity period is divided up throughout the entire history of a galaxy. Models indicate that SMBH accretion is likely episodic (Novak et al., 2011; Hickox et al., 2014; Anglés-Alcázar et al., 2017, 2021), perhaps the result of chaotic, randomly oriented accretion events (King & Nixon, 2015) as opposed to long-term, ordered accretion. This would imply that AGN activity is non-continuous, spread out through multiple periods of activity. This process of turning off and on is known as the AGN duty cycle.

One way to constrain the AGN duty cycle is by identifying AGN that have turned off or dramatically declined in luminosity. One example of this is where the AGN luminosity required to produce the distant (kpc-scale) photoionization region (i.e. the [O III] region) is at a mismatch to the current (lower) AGN luminosity. Such optical light echoes left behind by deactivated AGN support episodic activity periods of $10^4 - 10^5$ years (e.g., Lintott et al., 2009; Keel et al., 2012b,a; Schawinski et al., 2015; Sartori et al., 2018). Radio-loud AGN, which generate prominent jets and large lobes of radio-emitting plasma, indicate active phase durations of $10^7 - 10^8$ years based on studies of remnant lobes present around inactive radio cores (Alexander & Leahy, 1987; Liu et al., 1992; Parma et al., 1999; Harwood et al., 2013, 2016). Furthermore, the AGN duty cycle appears to have changed over the history of the Universe, with AGN being active for longer times earlier in cosmic history (Delvecchio et al., 2020).

There is still much uncertainty about the AGN duty cycle. One way to provide further constraints is to search not only for light-echoes or remnant radio lobes from AGN that have died out thousands of years ago, but to search for AGN that have only recently begun to fade away on timescales of years. The broad line region (BLR) is located close to the SMBH's accretion disk and is illuminated directly by the UV photons from that disk, so within a short time after accretion ceases, the BLR will disappear. In contrast the torus and the narrow line region (NLR) are further away from the accretion disk (see Figure 1.2) and so will remain lit up for some time after the AGN deactivates (10s-100s of years in the case of the torus; Ichikawa & Tazaki, 2017). This means a recently deactivated AGN would possess mid-infrared (MIR) emission from the torus, as well as the narrow emission lines of the NLR, but it would lack the signatures of a BLR. This would make the deactivated AGN resemble an obscured AGN, though in fact it intrinsically lacks a BLR, instead of merely having its BLR obscured from our line of sight. This motivates Chapter 3, in which I present a search for recently deactivated AGN in a sample of apparently obscured AGN.

1.3 The Reason for Using X-rays

For all the studies presented in this thesis, we use X-ray observations. X-rays hold unique promise for studying SMBHs because they probe the regions very close to the black hole. X-ray emission in AGN originates from a region called the corona (see Figure 1.2), which is a population of hot electrons that inverse Compton scatters photons from the accretion disk to X-ray energies. While the origin, geometry, and location of the corona is uncertain, it is known to be very close to the central SMBH (e.g., Zoghbi et al., 2012). X-rays therefore are the first region of the AGN emissions to become visible/invisible when an AGN activates/deactivates (e.g., Schawinski et al., 2015), making them very useful for studying AGN duty cycles. Hard X-ray emission, in particular, is a signature sign of an actively accreting AGN that cannot be produced by other processes (like star formation) and has the ability to penetrate obscuring bodies of dust and gas, revealing the presence of even heavily buried AGN. This means that deactivated AGN could be distinguished from an obscured AGN by the lack of hard X-ray emission from the corona. This is explored further in Chapter 3.

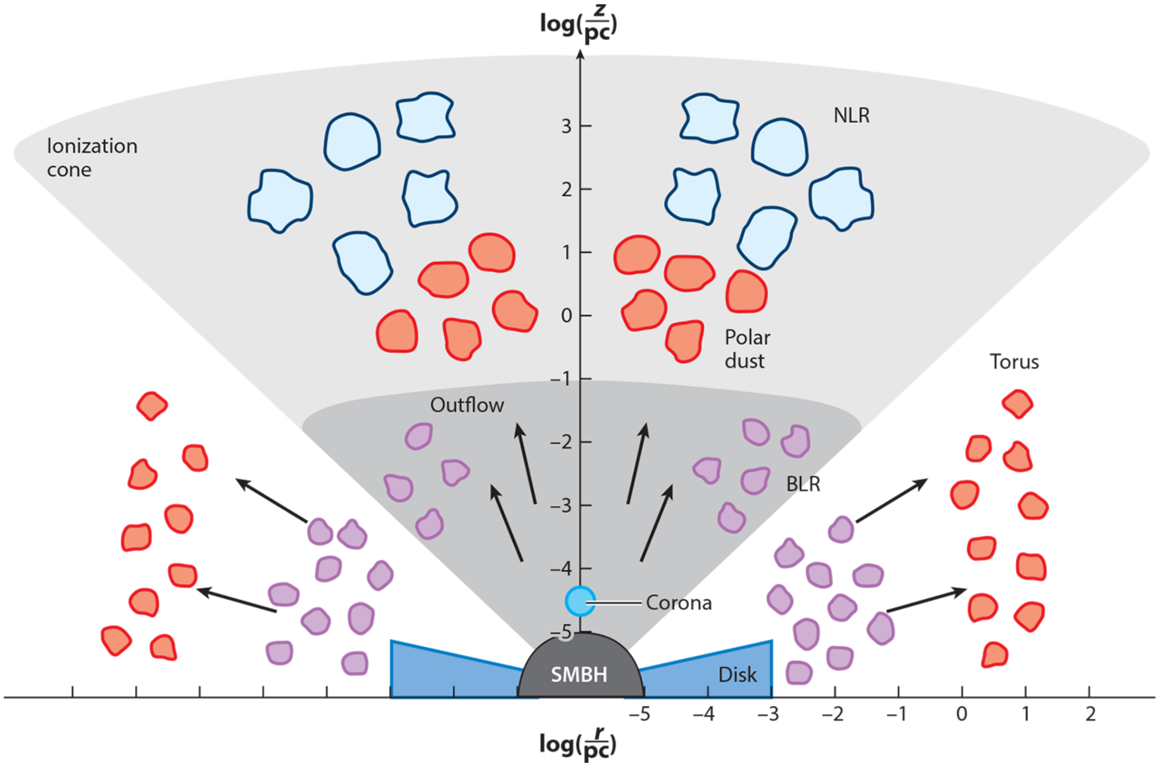

Figure 1.2 Diagram of the parts of an AGN. The corona, where the X-rays originate, is the closest region to the central SMBH, followed by the accretion disk, BLR, torus, and then NLR. If the line of sight to the SMBH runs through the torus, the BLR and accretion disk are obscured and not visible. However the hard X-ray emission from the corona can penetrate the torus and reveal the presence of an actively accreting SMBH. Reproduced with permission from Hickox & Alexander (2018), which itself reused the figure from Ramos Almeida & Ricci (2017).

The innermost regions of the accretion flow are also where a subparsec binary SMBH is expected to exist. Theoretical models generally predict unique X-ray properties for AGN with binary SMBHs, such as harder spectra (e.g., Roedig et al., 2014; Ryan & MacFadyen, 2017; Tang et al., 2018; Krolik et al., 2019) and greater X-ray luminosities compared to AGN with single SMBHs (e.g. Farris et al., 2015a). This raises the possibility of potentially confirming or denying binarity in binary SMBH candidates using X-rays. This is explored further in Chapter 2 and Chapter 4.

1.4 Outline of this Thesis

This thesis is outlined as follows: In Chapter 2 we present our analysis of *Chandra* observations of candidate binary SMBH systems, with the goal of testing theoretical models of these systems and possibly confirming or denying their binary status. In Chapter 3 we present an analysis of broad-band X-ray observations of apparently obscured AGN, with the goal of searching for AGN that have recently deactivated in order to help constrain the AGN duty cycle. In Chapter 4 we present *NuSTAR* follow-up observations to the *Chandra* observations from Chapter 2, with the goal of determining whether predicted X-ray signatures would show up in the hard X-ray band. In Chapter 5 we summarize our results.

CHAPTER 2

Chandra Observations of Candidate Subparsec Binary Supermassive Black Holes[1]

2.1 Introduction

Supermassive black holes (SMBHs) are believed to exist in the nuclei of all large galaxies. When galaxies merge, their respective SMBHs generally pair up to form binaries. The SMBH binary separation will then slowly shrink due to dynamical friction and multi-body interactions in asymmetric stellar distributions, as well as due to gas dynamics (Berczik et al., 2006; Mayer et al., 2007; Gualandris et al., 2017). Multi-body interactions with other SMBHs can also be relevant (Ryu et al., 2018). Once the binary reaches sub-parsec scales, the SMBHs can spiral together and merge on timescales shorter than the age of the Universe (Begelman et al., 1980). In the final months or years, corresponding to the final 100-1000 orbits before merger, binary SMBHs become strong gravitational wave sources that should be detectable by pulsar timing arrays or future observatories such as the *Laser Interferometer Space Antenna* (*LISA*; Amaro-Seoane et al., 2017). Close-separation binary SMBHs are therefore important for a range of astrophysical studies, from black hole growth to AGN triggering to gravitational wave physics. However, few such systems have been conclusively identified to date, and theoretical predictions of their multiwavelength properties

---

[1] This Chapter reproduces Saade et al. (2020; ApJ, 900, 148) subject only to formatting changes to adhere to the PhD thesis stylistic requirements.

vary greatly. In the following, we first review candidate binary SMBHs in the literature (§ 2.1.1), followed by a review of proposed observational signatures of such systems based on theoretical work (§ 2.1.2). We then discuss the motivation behind the work presented here (§ 2.1.3).

2.1.1 Candidate Binary SMBHs in the Literature

The first reported candidate sub-parsec binary SMBH was the blazar OJ 287, which displays quasi-periodic optical outbursts every twelve years that could be explained by a binary SMBH slowly decaying under the effects of gravitational radiation (Lehto & Valtonen, 1996). The binary explanation involves a $1.8 \times 10^{10}\,M_\odot$ primary (Valtonen et al., 2008) with a $1.4 \times 10^{8}\,M_\odot$ secondary (Valtonen et al., 2012) that impacts the primary's accretion disk nearly once per decade. With an optical light curve spanning over 120 years (Valtonen et al., 2012), OJ 287 is considered one of the strongest binary SMBH candidates to date.

Additional strong candidate SMBH merger precursors come from systems where multiple, well-separated active galactic nuclei (AGN) are imaged in the same galaxy, such as the two *Chandra*-detected X-ray AGN in NGC 6240 (Komossa et al., 2003), other dual X-ray sources (e.g., Koss et al., 2011, 2012; Comerford et al., 2015; Satyapal et al., 2017; Pfeifle et al., 2019a,b; Hou et al., 2019; Foord et al., 2020), dual radio sources (e.g., Rodriguez et al., 2006; Fu et al., 2011, 2015; Müller-Sánchez et al., 2015; Kharb et al., 2017; Rubinur et al., 2019), and dual optical sources (e.g., Liu et al., 2011; Comerford et al., 2012, 2013; Goulding et al., 2019). For a recent review paper on dual and binary AGNs, see De Rosa et al. (2019). As reliably distinguishing two AGN from each other requires the AGN to be well-separated, the dual AGN identified through this method have generally had separations greater than 1 kpc. For many years the closest example of a merging SMBH system with multiple AGN detected in imaging was the pair of flat-spectrum radio sources in 0402+379, separated by 7.3 pc (Rodriguez et al., 2006). Recently this has been superceded by a 0.35 pc pair of radio cores in NGC 7674 imaged at 15 GHz using very long baseline interferometry (VLBI; Kharb et al., 2017), and it is possible in the near future that subparsec binaries will be resolved with more advanced VLBI like the Event Horizon Telescope (EHT; D'Orazio & Loeb, 2018).

Unusual radio morphologies can also identify candidate merging SMBH systems, since jet precession is a well-established consequence of binary black hole systems (e.g., Gower et al., 1982). VLBI observations have revealed several examples of AGN with jet morphology suggestive of precession, such as S5 1928+738 (Kun et al., 2014), 3C 345 (Lobanov & Roland, 2005), and BL Lacertae (Caproni et al., 2013). Tsai et al. (2013) and Krause et al. (2019) present additional examples based on Australian Telescope Compact Array (ATCA), Very Large Array (VLA), and Multi-Element Radio Linked Interferometer Network (MERLIN) observations. However, these binary SMBH candidates based on jet morphology are considered controversial since Kelvin-Helmholtz instabilities can also mimic the warping of jets due to precession (e.g., Romero, 1995; Lobanov & Zensus, 2001).

More recently, there have been attempts to identify candidate binary SMBHs based on broad emission line profiles, under the assumption that a binary SMBH would modify the lines in a manner similar to a binary star system. Eracleous et al. (2012) carried out the first systematic search for quasars with broad line peaks substantially shifted from their nominal wavelengths (by thousands of km s^{-1}). They identified 88 such quasars in the Sloan Digital Sky Survey (SDSS), with 14 showing statistically significant changes in Hβ peak velocities. Further candidates from SDSS have been reported based on Mg II and Hβ emission lines (e.g., Shen et al., 2013; Ju et al., 2013; Liu et al., 2014; Guo et al., 2019). However, it might not be possible to identify highly sub-parsec binaries (e.g., ≤ 0.01 pc separation) with spectroscopic techniques, as the broad line region (BLR) would be far larger than the orbit of either SMBH, making it potentially insensitive to their movements (Shen & Loeb, 2010). Furthermore, several phenomena associated with isolated SMBHs could produce velocity offsets claimed as evidence of binary SMBHs, such as asymmetric reverberation-induced velocity shifts (Barth et al., 2015) and unusual BLR geometries (Liu et al., 2016). Wang et al. (2017) updated the analysis of the Ju et al. (2013) candidates, as well as observed 1438 more objects with a baseline of 8 years, and found only one candidate with an outlying velocity shift. Subject to these caveats, Li et al. (2016) reported a candidate close, centi-parsec (0.018 pc) SMBH binary in the galaxy NGC 5548 based on four decades of spectroscopic monitoring.

Binary SMBH systems can also produce cut-offs or notches in their continuum spectra, evident at rest-frame ultraviolet wavelengths, due to the presence of a secondary black hole truncating or clearing a gap or cavity in the circumbinary disk. Guo et al. (2020) recently presented a comprehensive analysis of the spectral energy distributions of ~ 150 published candidate periodically variable quasars, but found that the candidate periodic quasars are similar to the control sample matched in redshift and luminosity.

Perhaps the most promising way to identify highly sub-parsec binary SMBHs is through periodicity in AGN light curves. After OJ 287, the first examples of such objects were found in the Catalina Real-Time Transient Survey (CRTS; Drake et al., 2009). Graham et al. (2015a) reported the first such example, PG 1302-102, and Graham et al. (2015b) presented a sample of 111 candidate periodic quasars selected from a systematic analysis of 243,500 quasars with well-sampled CRTS light curves[2]. Notably, PG 1302-102 shows the same periodicity in ultraviolet (D'Orazio et al., 2015b) and mid-IR wavelengths (Jun et al., 2015a), as well as in the position angle of its radio jet (Qian et al., 2018). D'Orazio et al. (2015b) showed that the periodicity of PG 1302-102 could be well explained by a binary SMBH with a mass ratio of ≤ 0.3 separated by 0.007-0.017 pc (i.e., 1400- 3500 AU).

---

[2] Note that the newly identified periodic quasars are selected on the basis of sinusoidal variability, which is quite distinct from the regular flaring activity seen in OJ 287. The sinusoidal light curves are believed due to two SMBHs sharing a single circumbinary accretion disk, which naturally leads to the lower mass black hole having a higher accretion rate and thus the black holes rapidly becoming near equal mass. OJ 287, on the other hand, has a small secondary SMBH plunging through the accretion disk of a significantly ($\sim 100\times$) more massive primary twice per orbit (Dey et al., 2018). Therefore, many of the tests for a binary SMBH described below (§2.1.2), and, in particular, tests based on X-ray spectral analysis, are not relevant for OJ 287 despite the significant X-ray observations that exist for this system (e.g., Marscher & Jorstad, 2011; Kushwaha et al., 2018; Pal et al., 2020).

Relativistic Doppler boosting and beaming of emission from the secondary SMBH's accretion disk as it orbits a more massive ($\geq 10^{9.1}\, M_\odot$) primary creates the variations observed in the light curve. Liu et al. (2018) argued that including data from the All-Automated Sky Survey for Supernovae (ASAS-SN) weakened the case for true periodicity in PG 1302-102, though Xin et al. (2020) reported on nine additional epochs of simultaneous ultraviolet and optical *Swift* observations, finding light curves roughly consistent with the expected trends for the binary model.

Since the landmark study from Graham et al. (2015b), several other instances of claimed periodicity have been reported in quasar optical light curves, including examples from the optical photometric databases of PAN-STARRs (Liu et al., 2019) and the Palomar Transient Factory (Charisi et al., 2016; Dorn-Wallenstein et al., 2017). At higher energies, there have been reports of quasi-periodicity in the gamma-ray light curves of several blazars (Sandrinelli et al., 2016), suggestive of SMBH binaries akin to OJ 287, and claims of modular *Swift*-BAT and *Swift*-XRT light curves in a local Seyfert galaxy (Severgnini et al., 2018). However, concerns with the statistical analyses have been common, including noting the importance of including 'red noise' stochastic quasar variability when calculating the false alarm probability (Vaughan et al., 2016), as well as proper consideration of the look-elsewhere effect (Barth & Stern, 2018). While some studies have accounted for these effects in full (e.g., Graham et al., 2015b; Charisi et al., 2016), the form of the red noise has sometimes been questioned. For example, Charisi et al. (2016) adopted a damped random walk model with Gaussian red noise. M. J. Graham et al. (in preparation) presents a more in-depth analysis of these issues, as well as updates the Graham et al. (2015b) sample with several more years of photometric monitoring.

2.1.2 Predicted Observational Signatures of Binary SMBHs

Theoretical models predict a variety of features to be present in accreting binary SMBHs. The two black holes are surrounded by a circumbinary disk, from which accretion streams feed onto mini-disks surrounding each individual black hole. In the interior of the circumbinary disk, a cavity is cleared out by tidal torques from the binary (Artymowicz & Lubow, 1994). Figure 8 in d'Ascoli et al. (2018) and Figure 3 in Farris et al. (2014) both provide good illustrations of these features.

Despite the presence of the cavity, the accretion rate onto the SMBHs is not lower than for a single SMBH (D'Orazio et al., 2013), and can temporarily exceed that for a single SMBH (Rafikov, 2016). The total luminosity of the system is also not lower than for a single SMBH (Farris et al., 2015a). For highly unequal mass binaries expected to form as a result of hierarchical galaxy formation (e.g., Volonteri et al., 2003), most of the luminosity arises from accretion onto the secondary black hole (Farris et al., 2014; Duffell et al., 2020).

Since accretion is able to proceed in a binary SMBH system as efficiently as with a single SMBH, binary SMBHs should still be able to launch jets. It is well-established that jets will precess under the influence of a black hole binary, creating a jet morphology that is helical on a conical surface (Gower et al., 1982) or wiggled and knotted (Kaastra & Roos, 1992). The Doppler shift in the synchrotron radiation of the jet will vary periodically due to the precession of the jet, creating periodicity in the radio light curve (Kun et al., 2014).

Multiple mechanisms might also cause the accretion onto binary SMBHs to be periodic as well. D'Orazio et al. (2013) discuss oscillations in accretion rate created by hydrodynamic interactions of the accretion streams with an overdense lump at the inner edge of the circumbinary disk (see also Farris et al., 2014; Shi & Krolik, 2015). The resulting periodicity in emission depends on whether emission arises primarily from the circumbinary disk or from the mini-disks — with implications for the soft vs. hard X-ray light curve as well (Tang et al., 2018). Doppler boosts are another possible source of periodic behavior (e.g., D'Orazio et al., 2015b). For a binary where the primary and secondary have equal mass, $M_1 = M_2$, accretion rate oscillations will dominate over Doppler boost oscillations (Tang et al., 2018). However, hydrodynamical modulations decline in magnitude with decreasing mass ratio, $q \equiv M_2/M_1$, such that for $q \leq 0.05$, Doppler effects dominate the periodicity (D'Orazio et al., 2013; Farris et al., 2014; Duffell et al., 2020). One last additional source of potential periodic behavior is self-lensing of the accretion flow of one SMBH by the gravitational field of the other (Haiman, 2017; D'Orazio & Di Stefano, 2018). It is worth distinguishing the relative shapes these modulations introduce onto the light curve, varying from quasi-sinusoidal (Doppler) to bursty (hydrodynamic) to repeating sharp spikes (self-lensing). Current searches for periodic behavior in AGN light curves may only be able to detect the first of these shapes.

In addition to periodicity, potential spectral signatures of binary SMBHs have been considered in the literature. In the UV/optical portion of the electromagnetic spectrum, Roedig et al. (2014) argued that the central cavity cleared by the binary would generate a deep notch in the thermal continuum. In contrast, Farris et al. (2015b) and d'Ascoli et al. (2018) did not recover the notch, finding that the accretion streams compensate for this gap. Nguyen & Bogdanović (2016) generated a database of Hβ emission line profiles for sub-parsec binary SMBHs assuming both SMBHs possess mini-disks and illuminate the circumbinary disk. Some of the line profiles generated were highly complex and time-variable, including multiple peaks, but they were also highly dependent on the semi-major axis of the binary as well as the alignment between the mini-disks and the observer. Further work by Nguyen et al. (2019) revealed that including the effects of accretion disk winds eliminated the more complex line profiles. This recent work therefore argued that emission line profiles on their own cannot be used to confirm an SMBH binary.

In the X-rays, potential sources of emission in a binary SMBH are the circumbinary disk (Tang et al., 2018), hot spots where the accretion streams from the circumbinary disk collide with the mini-disks around each SMBH (Roedig et al., 2014), and the mini-disks themselves (Farris et al., 2015a). Roedig et al. (2014) predicted that a binary SMBH would have a substantially harder X-ray spectrum than a single SMBH due to thermal emission from the hot spots, with Wien tail emission causing a peak in the spectrum at $\gtrsim 100$ keV. Ryan

& MacFadyen (2017) found a similar hardening of the X-ray spectrum of binary SMBHs compared to a Novikov-Thorne relativistic thin disk model of an isolated accreting SMBH. However, their hardening takes place at lower energies, at $\gtrsim$ 10 keV. Farris et al. (2015a) predicted that the X-ray spectrum of a binary SMBH will be distinctly harder than a single SMBH that results from a merger. Tang et al. (2018) modeled close binaries up until merger, and predicted that the Doppler effect will suppress 1-20 keV emission, while enhancing higher energy emission during the binary phase. They predicted two thermal peaks in the X-ray spectrum, one from the circumbinary disk at $\approx$ 1 keV and another from the mini-disks at $\approx$ 20 keV, with a shallow notch between them. In their simulations of the X-ray spectrum of close binary SMBH systems, d'Ascoli et al. (2018) only recovered a single peak at $\approx$ 20 keV, due to Compton reflection by cold, optically-thick matter in the vicinity of the central engine, as commonly seen in isolated SMBH systems (e.g., George & Fabian, 1991), while emission in the soft X-rays was dominated by the thermal Wien tail from the mini-disks. Their hard X-ray emission was a similar fraction of the total luminosity as that in a single SMBH system, whereas the thermal soft X-ray emission component was more pronounced than in a single SMBH system, though overall they point out their binary SMBH spectrum is more modestly different from a single SMBH spectrum compared to previous models in the literature. Thus, while many results indicate that binary SMBHs should have enhanced X-ray emission relative to single SMBH systems, there is a wide range in the predicted energy at which these enhancements would be seen, ranging from relatively low rest-frame energies of $\sim$ 1 keV (e.g., Farris et al., 2015a) to energies more than two orders of magnitude higher (e.g., Roedig et al., 2014). This raises the possibility of binary SMBH systems having dramatically different X-ray spectral indices or ratios of optical to X-ray luminosity than single SMBH systems, which we investigate in § 2.3.1 and § 2.3.2.

McKernan et al. (2013) also predicted unique patterns of Fe K-α X-ray spectral lines due to the clearing of the central circumbinary disk by the inward migrating secondary. The broad Fe K-α line profile becomes ripple-shaped due to the presence of an annular gap, with dips in both the red and blue wings of the profile. The energy of these dips depends on the orbital separation. If an inner cavity is cleared in the circumbinary disk, the wings of the broad line profile are suppressed, and if gas piles up at the outer edge of the cavity, double peaks will appear in the broad line profile. McKernan et al. (2013) also modelled the effects of having both the primary and secondary accrete, which creates a secondary broad line component that oscillates on an orbital timescale across the Fe K-α line of the primary. This opens the exciting possibility of spectroscopically detecting very compact binary SMBHs through Doppler shifts in the Fe K-α lines.

It should be noted that models in the literature have only considered binaries with close separations less than a few hundred gravitational radii. We discuss the implications of this further in § 2.4.1.

2.1.3 Motivation for this Work

We present the first X-ray spectra for a sample of candidate sub-parsec binary SMBHs. Foord et al. (2017) presented a related analysis of a single candidate binary SMBH system **(see §2.4.1)**. X-rays probe regions of an AGN closer to the central engine than optical and ultraviolet emission, and theoretical work suggests the unique high-energy emission of binary SMBHs could confirm the nature of such systems, as well as provide great promise for probing the compact inner regions where a sub-parsec binary SMBH would be located. However, the wide range of high-energy predictions leaves significant uncertainty on distinguishing features of binary SMBHs. For example, Tang et al. (2018) and d'Ascoli et al. (2018) have very different predictions for modeled binaries of similar separation, with the former predicting two peaks in the X-ray spectrum and the latter predicting a single peak. Indeed, no simulation to date has predicted a spectrum with correct and self-consistent thermodynamics, and the results, including the overall scaling of the spectrum (e.g., photon energy, emerging luminosity) is therefore subject to very large uncertainty. This uncertainty reflects the range of different ad-hoc thermodynamical assumptions in different papers. We therefore crafted our program to provide a first set of observational results to motivate future models, with the goal of searching for any substantial differences in the spectra of candidate binary SMBHs. Specifically, we sought to observe the maximal number of sources in the minimal amount of observing time. While emission lines like Fe K-α are another promising way to use X-ray spectra to confirm and study close binary SMBH systems (McKernan et al., 2013), the requirements for sufficient detections were beyond the scope of this observational program.

The X-ray data come from a combination of guest observer (GO) and guaranteed time observations (GTO) with the *Chandra X-ray Observatory*. The rest of the chapter is structured as follows: § 2.2 presents the sample selection and X-ray observations; § 2.3 discusses the properties of the sample; § 2.4 discusses the results, summarizes our conclusions, and discusses possibilities for future work. Throughout, we adopt the concordance cosmology, $\Omega_{\rm M} = 0.3$, $\Omega_\Lambda = 0.7$ and $H_0 = 70\ {\rm km\,s^{-1}\,Mpc^{-1}}$.

2.2 Sample and X-Ray Data

2.2.1 Sample Selection and *Chandra* Observations

We selected for observation candidate periodic quasars from Graham et al. (2015b). In order to ensure high-quality X-ray spectra for this first investigation of a sample of candidate sub-parsec binary SMBH systems in a reasonable observing program (e.g., $\gtrsim 1000$ counts in $\lesssim 10$ ks, per source), we cross-correlated the 111 sources in Graham et al. (2015b) with the *ROSAT* All-Sky Survey Bright Source Catalogue (Voges et al., 1999). Using an $18''$ matching radius (approximately twice the astrometric uncertainty of that survey), nine sources were found to have *ROSAT* detections. PG 1302-102, the first candidate sub-pc binary SMBH identified from a periodic optical light curve (Graham et al., 2015a), was awarded *Chandra* GTO time in Cycle 18 (P.I. R. Kraft; ObsIDs 19745-19746). Another six sources were awarded GO time in the same cycle (P.I. D. Stern; ObsIDs 19525-19530). Table 2.1 presents basic properties of the target sample and details of the *Chandra* observations. The sources

Table 2.1. Target sample and *Chandra* observation details.

Object	R.A., Dec. (J2000)	z	Obs. Date	Exposure (ks)
2MASSi J0411469+132416	04:11:46.90, +13:24:16.0	0.277	2017 Mar 26	2.7
2MASXi J0729087+400836	07:29:08.71, +40:08:36.6	0.074	2017 Apr 28	7.6
RBS 874	10:30:24.95, +55:16:22.7	0.435	2017 Sep 4	15.4
PG 1302-102	13:05:33.01, −10:33:19.4	0.278	2016 Dec 14	10.3
FBQS J163302.6+234928	16:33:02.66, +23:49:28.5	0.821	2017 May 19	7.4
Mrk 504	17:01:07.76, +29:24:25.0	0.036	2017 Jun 21	5.1
4C +50.43	17:31:03.60, +50:07:34.0	1.070	2018 Apr 17	15.9

range from relatively local (e.g., Mrk 504 at $z = 0.036$; ~ 160 Mpc) to $z > 1$. *Chandra* exposure times range from 2.7 ks to 15.9 ks. The sources were all observed using the ACIS-S instrument.

2.2.2 *Chandra* Data Analysis

We extracted the *Chandra* spectra using the standard *Chandra* software packages CIAO (version 4.10) with the latest calibration files from CALDB (version 4.8.0). We extracted spectra using the default spectral grouping carried out by CIAO `specextract`, where the spectrum is grouped with a minimum of 15 counts per bin. The spectra were extracted in circular source regions with $2''$ radius, with backgrounds measured in source-free annular regions centered on the targets of inner radius $10''$ and outer radius $20''$. The spectra were analyzed using XSPEC with the background subtracted and the χ^2 statistic for fitting. We fit each source to a simple power law, adopting the appropriate Galactic absorption from the National Radio Astronomy Observatory (NRAO; Dickey & Lockman, 1990). We also investigated including an additional absorption component at the source redshift, but the resulting absorption columns were negligible and the changes in χ^2 did not justify this choice of fit. The one exception was 2MASSi J0411469+132416. However, the statistical fitting favored physically implausible values $\Gamma > 5$ and $N_{\rm H} \sim 10^{23}\,{\rm cm}^{-2}$, which were particularly unlikely values given the shape of the 2MASSi J0411469+132416 X-ray spectrum and the

Table 2.2. X-ray properties of the sample.

Object	Counts[a]	Γ[b]	f_{2-10}[c]	χ^2/D.O.F.	α_{OX}
2MASSi J0411469+132416	218	$2.29^{+0.51}_{-0.47}$	$0.57^{+0.09}_{-0.12}$	7.02/5	1.58
2MASXi J0729087+400836	2002	$1.35^{+0.14}_{-0.14}$	$3.74^{+0.26}_{-0.24}$	53.75/65	0.71
RBS 874	1891	$1.53^{+0.12}_{-0.12}$	$1.01^{+0.05}_{-0.06}$	50.76/60	1.39
PG 1302-102	2379	$1.59^{+0.13}_{-0.12}$	$2.00^{+0.12}_{-0.10}$	51.56/64	1.66
FBQS J163302.6+234928	1388	$1.73^{+0.13}_{-0.12}$	$1.35^{+0.08}_{-0.07}$	57.76/56	1.55
Mrk 504	2093	$1.59^{+0.18}_{-0.17}$	$3.90^{+0.27}_{-0.34}$	57.01/48	1.30
4C +50.43	580	$1.74^{+0.21}_{-0.20}$	$0.26^{+0.03}_{-0.03}$	20.52/25	1.56

Note. — D.O.F. stands for 'degrees of freedom'. Error bars represent 90% confidence intervals.

[a] Total counts in the observed 0.5-8 keV band.

[b] Fit in rest-frame 2-10 keV band.

[c] Flux in rest-frame 2-10 keV band, in units of 10^{-12} erg cm^{-2} s^{-1}.

broad Balmer lines in its optical spectrum. Therefore, only Galactic absorption was ultimately included in the final fits for all sources. We did not detect any Fe K-α lines, which is typical for unobscured AGN with with less than $\approx 10^5$ counts (de La Calle Pérez et al., 2010). Table 2.2 presents the results of the spectral fitting and Fig. 2.2 shows the *Chandra* X-ray spectra from this study.

2.3 Properties of Sample

2.3.1 Black Hole Binary and Active Galaxy Properties

We recovered black hole masses for each quasar from Graham et al. (2015b), with the exceptions of Mrk 504 and 4C +50.43 which lacked masses in that paper. For Mrk 504, we use the mass from Ho et al. (2008), while for 4C +50.43, we derived a mass from Palomar optical spectra obtained in September 2019 using the relations in Jun et al. (2015b). Graham et al. (2015b) had a suspiciously low mass listed for 2MASXi J0729087+400836,

$\log(M_{\mathrm{BH}}/M_{\odot}) = 5.71$, leading to a suspiciously high Eddington ratio. We instead use the mass from Oh et al. (2015) for this source. Assuming these single-epoch SMBH masses represent the total binary mass[3], we calculated separations for each binary SMBH assuming circular orbits and a mass ratio $q = M_2/M_1 = 0.5$ where $M_{1,2}$ are the masses of the two SMBHs. The separations are expressed in terms of the gravitational radius r_g where $r_g = GM/c^2$, G is the gravitational constant, M is the total binary mass, and c is the speed of light.

There is a well-established correlation between X-ray spectral index Γ and the Eddington ratio of AGN, $\lambda_{\mathrm{Edd}} = L_{\mathrm{bol}}/L_{\mathrm{Edd}}$, where L_{bol} is the bolometric luminosity and L_{Edd} is the Eddington luminosity (Trakhtenbrot et al., 2017). In addition, AGN variability correlates with Eddington ratio (Guo & Gu, 2014; Rumbaugh et al., 2018). Sources with lower Eddington ratios have harder X-ray spectra and are more variable. As it may have implications for this work, we estimated the Eddington ratios for the sample. Bolometric luminosities were estimated using the 2-10 keV bolometric correction $\kappa_x = L_{\mathrm{bol}}/L_X$, where L_X is the rest frame 2-10 keV X-ray luminosity. L_X was calculated using our measured values of f_{2-10} (listed in Table 2.2) and the luminosity distance for each source listed in the NASA/IPAC Extragalactic Database (NED). A value of $\kappa_x = 23$, the median bolometric correction for unobscured AGN (Lusso et al., 2011), was used to derive the bolometric luminosity. Finally, the bolometric luminosities were divided by the Eddington luminosity for each object, which was estimated using $L_{\mathrm{Edd}} = 1.26 \times 10^{38}\,(M_{\mathrm{BH}}/M_{\odot})\,\mathrm{erg\,s^{-1}}$.

The CRTS quasars vary widely in their binary properties, with SMBH masses ranging from $4.9 \times 10^6 M_{\odot}$ to $7.2 \times 10^9 M_{\odot}$ and binary separations ranging from 57 r_g to more than 8400 r_g. They generally have typical quasar Eddington ratios of a few tenths, with the exception

---

[3] The masses were ultimately calibrated using broad line reverberation relations derived from local Seyfert galaxies. As the extent of a quasar BLR is likely far larger than the sub-parsec SMBH binary separations considered here, taking the measured mass to be the total binary mass is reasonable within the caveat concerning the unclear extent to which the original relations apply to luminous quasars.

Table 2.3. SMBH binary properties, based on Table 2 in Graham et al. (2015b).

Object	$\log M_{\rm BH}$ ($M_\odot$)	r (c)	Period (d)	$L_{\rm bol}/L_{\rm Edd}$	Morphology
2MASSi J0411469+132416	8.16	922	1851	0.18	unresolved; possible close neighbor
2MASXi J0729087+400836	7.74	1799	1612	0.18	nucleated galaxy
RBS 874	8.43	493	1515	0.50	unresolved
PG 1302-102	8.50	516	1694	0.30	unresolved; merger features (Hong et al., 2015)
FBQS J163302.6+234928	9.86	57	2040	0.12	unresolved
Mrk 504	6.69	8437	1408	0.46	nucleated ring galaxy (Buta, 2017)
4C +50.43	8.18	677	1975	2.22	unresolved

Note. — Masses are single-epoch mass measurements based on scaling relations for non-binary AGN and are assumed to be the total binary mass (e.g., $M_1 + M_2$) (see text for details). Separations (r) assume mass ratios of $q = M_2/M_1 = 0.5$. Morphologies are based on PanSTARRS, supplemented with SDSS when available.

of 4C +50.43, which has an Eddington ratio of ≈ 2 according to our methodology. However, 4C +50.43 is radio-loud, and radio-loud quasars are known to have elevated X-ray emission (e.g., Zamorani et al., 1981; Miller et al., 2011), implying that 4C +50.43 is unlikely to be super-Eddington. All the other sources in our sample are radio-quiet, with radio fluxes several orders of magnitude lower than 4C +50.43.

These properties, as well as the observed period from CRTS and galaxy morphology, are listed in Table 2.3. The morphologies are based on visual inspection of PanSTARRS images, supplemented by SDSS images when available. Five of the sources appear unresolved in the ground-based imaging, with the AGN outshining the host galaxy. The two lowest redshift sources show a bright, compact nucleus within a disk-like host galaxy. The table cites published literature that discusses the morphologies of two of the galaxies, both of which show morphological evidence of recent merger activity.

2.3.2 X-Ray Spectral Indices

Several of the theoretical models discussed in § 2.1.2 predict that merging SMBH systems should have harder X-ray spectra than isolated accreting SMBHs. We therefore first analyzed the X-ray spectra to determine if the candidate merging SMBH systems had unusual X-ray spectral indices. Table 2.2 presents the results from our fitting, showing that the spectral indices range from 1.35 to 2.29, with a mean value of 1.68 ± 0.27. Such a mean value is on the low (or hard) side for AGN in general, which typically have $\Gamma \sim 1.9$, but not inconsistent with their full range of $\sim 1.5 - 2.0$ (e.g. Nandra & Pounds, 1994; Shemmer et al., 2008; Brightman et al., 2013).

To make this comparison more quantitative, we used a two-sample Kolmogorov-Smirnov (KS) test to compare the spectral indices of our sample with the spectral indices of accreting SMBHs in the BAT AGN Spectroscopic Survey (BASS; Ricci et al., 2017a), using their tabulated values of $\Gamma_{0.3-10}$ in Table 15. PG 1302-102 was present in the BASS dataset, so it was discarded from the BASS sample before the KS test was performed. The KS test resulted in a p-value of 0.272, which is too large to reject the null hypothesis that our source spectral indices were drawn from the same distribution as the BASS sample. Cutting the BASS sample to only include unobscured AGN (i.e. with $N_{\mathrm{H}} < 10^{22}\,\mathrm{cm}^{-2}$) and AGN with Eddington ratios similar to our sample ($0.1 < L/L_{\mathrm{Edd}} < 1$) resulted in a p-value of 0.107, not changing the results of the KS test. Further cuts on the BASS control sample based on parameters such as SMBH mass and redshift are inadvisable as our sample is too hetergeneous for this to be warranted (see Table 2.1 and Table 2.3). We therefore conclude that these seven candidate merging SMBH systems have X-ray colors, or spectral indices, typical of isolated quasars, at least over the observed $0.5 - 8$ keV range probed by *Chandra*. To investigate spectral hardening at higher energies would require observations with a satellite sensitive to to > 10 keV photons, such as the *Nuclear Spectroscopic Telescope Array* (*NuSTAR*; Harrison et al., 2013).

2.3.3 Optical-to-X-Ray Luminosities

We next investigated whether the candidate merging SMBH systems had unusually strong (or weak) X-ray emission, as suggested by some theoretical models. For this analysis, we considered the relationship between the X-ray luminosity and UV/optical luminosity, as quantified by the $\alpha_{\rm OX}$ parameter (e.g., Tananbaum et al., 1979; Just et al., 2007; Lusso et al., 2010). The relation between the two quantities is typically expressed as a linear correlation $\log(L_{2\ {\rm keV}}) = \gamma \log(L_{2500\text{Å}}) + \beta$ (Lusso & Risaliti, 2016), or in terms of the parameter $\alpha_{\rm OX}$, defined as

$$\alpha_{\rm OX} = -\frac{\log(f_{2\ {\rm kev}}/f_{2500\text{Å}})}{2.605}. \tag{2.1}$$

The mean value for $\alpha_{\rm OX}$ is typically around 1.5 (e.g. Lusso & Risaliti, 2016).

We recovered the monochromatic rest-frame 2 keV flux density from the XSPEC model. For the rest-frame 2500 Å flux density, we linearly interpolated between the two nearest effective wavelengths present in public archives of large surveys. For most of the sources, this was the FUV and NUV observations from the *GALEX* All-Sky Imaging Survey (Bianchi et al., 2017), but for the higher redshift sources FBQS J163302.6+234928 and 4C +50.43, we used u- and g-band data from the Sloan Digital Sky Survey and g- and r-band data from PanSTARRS, respectively. To correct for Galactic extinction, we used the Schlafly & Finkbeiner (2011) reddening map to determine $E(B-V)$ at the location of each source. For the SDSS and PanSTARRS photometry, we used the NASA/IPAC Extragalactic Database (NED) on-line extinction calculator to determine the implied extinction in the optical bands for the Fitzpatrick (1999) mean extinction curve. For the *GALEX* bands, we used the same NED extinction calculator to determine the CTIO V-band extinction, and then converted this to *GALEX* FUV and NUV extinctions using the Fitzpatrick & Massa (1990) parameterization of the UV extinction curve.

We then computed the luminosity of each source at 2500 Å and 2 keV using the luminosity distances listed in NED for each source. Our calculated values of $\alpha_{\rm OX}$ for each source are listed in the final column of Table 2.2. The values range from 0.71 to 1.66, with a mean value of 1.39. Figure 2.1 plots $L_{\rm 2keV}$ as a function of $L_{2500\text{Å}}$ for our sources, with the corresponding relations from Lusso et al. (2010) and Lusso & Risaliti (2016). Out of all the candidate binary SMBH systems investigated here, none are outside the error bars of Lusso et al. (2010) and only one (2MASXi J0729087+400836) is more than 1σ away from the mean trendline of Lusso & Risaliti (2016). We therefore conclude that these seven candidate merging SMBH systems have optical-to-X-ray luminosities typical of isolated AGN, at least over the observed $0.5-8$ keV range probed by *Chandra*.

2.4 Discussion

We find no obvious differences between the X-ray spectra of the seven sub-parcsec binary quasar candidates in our sample and the X-ray spectra of the quasar population at large, at least over the energies observed by *Chandra*. However, the meaning of this result is unclear. Due to the small sample size studied, unless the differences between binary SMBH and single SMBH spectra are large, there is little chance of detecting a statistically significant difference between binary SMBH quasars and the larger quasar population. We first discuss how details of the binary SMBH models might affect the interpretation of our X-ray results (§ 2.4.1), and we then discuss potential concerns with the sample itself (§ 2.4.2).

2.4.1 Concerns with Binary SMBH Models

Assuming the models in the literature are correct, there are several reasons why our sources might truly be sub-parcsec binary SMBH systems but we still would not have expected to observe differences between the *Chandra* spectra of our sources and single SMBH systems. The Roedig et al. (2014), Tang et al. (2018), and d'Ascoli et al. (2018) models of SMBH binaries have distinct peaks in their X-ray spectra outside the rest-frame 2-10 keV range of energies we observed for most sources, while Figure 3 of Roedig et al. (2014) and Figure 17 of Ryan & MacFadyen (2017) show only very slight hardening of the X-ray spectra in the 2-10 rest frame keV band. We note that the binary SMBH candidate PSO J334.2028+01.4075 (identified as a candidate by Liu et al., 2015) was observed by Foord et al. (2017) using

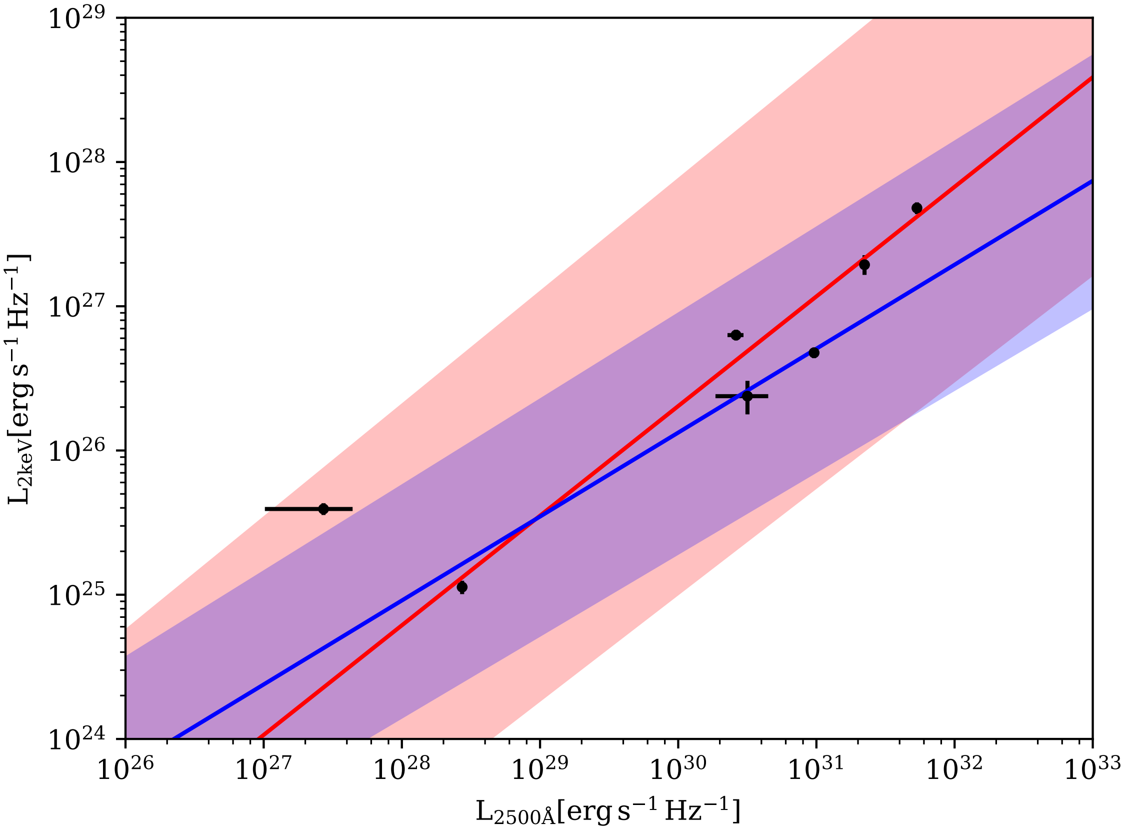

Figure 2.1 $L_{2500\text{Å}}$ vs. $L_{2\mathrm{keV}}$ for our seven sources. Error bars represent propagated 1σ uncertainties for optical fluxes, and 90% confidence intervals for X-ray fluxes. In red is the relation from Eq. 6 of Lusso et al. (2010) and in blue is the relation for the main sample from Table 2 of Lusso & Risaliti (2016). The shaded regions represent 1σ deviations from the mean relation.

Chandra, and no peculiarities in the X-ray spectrum were found[4]. It is therefore possible that the signatures of a binary SMBH lie outside the energy range of *Chandra*.

Farris et al. (2015b) found that the enhancement of emission in binary SMBH systems likely extends to energies lower than the soft X-ray band due to thermal emission from the accretion streams that thread the central cavity. If this emission is enhanced in binary SMBH systems relative to single SMBH systems across the entire optical-UV-X-ray range, then we might not expect our sources to have α_{OX} values distinct from the larger quasar population.

The binary separations, a, are also likely an issue for this set of targets being compared to theoretical models. d'Ascoli et al. (2018) find that changing the separation of an SMBH binary alters the temperature ratio of the mini-disks relative to the circumbinary disks, with implications for the high-energy spectra. Roedig et al. (2014) specifically highlight that their predicted excess thermal X-ray emission would only be clearly distinguishable from ordinary coronal X-rays for binary separations less than 100 gravitational radii, i.e., $< 100\,r_g$. Many of the published models examine very tight sub-parsec binary systems. For example, d'Ascoli et al. (2018) modeled a binary with $a = 20\,r_g$, while Tang et al. (2018) start with a separation $a = 60\,r_g$ and evolve it to merger. Roedig et al. (2014), Ryan & MacFadyen (2017), and Farris et al. (2015b) considered wider binaries with $a \leq 300\,r_g$, $a \approx 100\,r_g$, and $a = 100\,r_g$, respectively. Farris et al. (2015a) started with a binary at around the same separation as Farris et al. (2015b) and evolved it until merger.

Considering the binary separations in Table 2.3, only one of our sources has a binary separation $a < 300\,r_g$ (FBQS J163302.6+234928), and two are separated by more than 1000 r_g (2MASXi J0729087+400836 and Mrk 504). Therefore, it is possible that our sources indeed contain binary SMBHs, but with larger separations than what theorists have modeled to

---

[4] Note, however, that recent work on PSO J334.2028+01.4075 has weakened the case for periodicity in its optical light curve (e.g., Liu et al., 2016) and disfavored its status as a binary SMBH system (e.g., Benke et al., 2018).

date, and at separations where the X-ray spectra are largely indistinguishable from isolated SMBHs.

Furthermore, modeling the extreme regions around isolated accreting SMBHs has many uncertainties, such as the value of the disk viscosity, α, in the Shakura & Sunyaev (1973) accretion disk model (e.g., King et al., 2007), or understanding the geometry of the X-ray emitting corona. Extending these simulations to binary quasars with relativistic velocities is clearly pushing the theoretical models to new, uncertain regimes. Many uncertainties in models of binary SMBHs arise due to simplifying assumptions. Numerical constraints mean modeled accretion disks are often thicker than AGN disks are in actuality. This shifts the disk Mach number and therefore the frequency of emitted radiation (Tang et al., 2018). Effectively, these simulated disks are much hotter than in reality and so the thermal X-ray emission predicted in these simulations needs to be scaled down to lower photon energies.

Similarly, coronae, which are believed responsible for AGN X-ray emission through inverse Compton up-scattering of thermal disk photons, are generally not modeled, but are simply either painted on (e.g., d'Ascoli et al., 2018) or modeled as thermal emission (e.g., Farris et al., 2015b,a; Tang et al., 2018). d'Ascoli et al. (2018) note that the manner in which they introduce the corona into their model would lead to an underestimate of hard inverse Compton X-rays and an overestimate of softer thermal X-rays, while Tang et al. (2018) note their lack of a true corona would overestimate the ability of the Doppler effect to suppress lower energy X-rays. A first principles description of AGN coronae is not present at this time, and models have difficulty generating observed spectral energy distributions (SEDs) even for single isolated SMBHs. This lack of understanding of the corona introduces complications for direct comparisons of the theoretical SEDs of binary SMBHs to the SED of a single SMBH. Finally, we note that most of the theoretical models use a fiducial SMBH mass of $10^8\,M_\odot$, while our sample ranges from 10^6 to $10^9\,M_\odot$. This likely has some implications in terms of the expected slope and peak energy of the disk emission. However, it should be noted the dependence of the disk thermal emission on SMBH mass is not as strong as the dependence on binary separation and disk Mach number (e.g., Farris et al., 2015b,a).

2.4.2 The True Nature of the Sources

It is uncertain whether or not the seven CRTS quasars in our sample are truly periodic sources. Quasars are known to vary stochastically. The power spectrum of these fluctuations is broad, with the power increasing at low frequencies ("red noise"). The spectrum is often approximated as a power law, $P(f) \propto f^{-\alpha}$, with $\alpha \gtrsim 1$ over long timescales (Vaughan, 2012). It is possible for this noise to generate apparent periodicity when there is none; e.g., Vaughan et al. (2016) generated false periodicity in simulated CRTS light curves of PG 1302-102 even though the quasar's output was generated as a damped random walk (DRW) or Gaussian noise. This can occur even for well-sampled data as long as the number of period cycles observed is small (Barth & Stern, 2018). It is also the case when searching for an effect within a wide parameter space where the true location of the effect is unknown, statistically significant detections will happen by pure chance, the so-called "look-elsewhere effect" (Gross & Vitells, 2010). Properly accounting for the false alarm probability due to the look-elsewhere effect requires a noise model, and if the true stochastic variability contains more power than the best-fit DRW light curves, the purported periodicity can disappear with further observations.

The original Graham et al. (2015b) survey considered CRTS light curves for 243,500 quasars, looking for a strong Keplerian periodic signal with at least 1.5 cycles over a baseline of nine years. Though simulated data sets assuming stochastic variability (e.g., red noise) produced no equivalent candidates, implying a low likelihood of spurious detections, the short sampling time relative to the best-fit periods raises a natural concern for false positives.

In addition, even if the periodic behavior observed by CRTS is real, this does not necessarily mean that the quasars in our sample are all sub-parsec binaries. A hotspot on the accretion disk could produce a periodic light curve, with the caveat that many of the mechanisms that might produce a disk hotspot involve an SMBH binary (see D'Orazio et al., 2015a, and references therein). There are alternative explanations for periodicity that involve only a single SMBH. For example, SMBHs are all expected to have non-zero angular momentum, and so Lense-Thirring precession will be important if the accretion disk is offset from the equatorial plane of the rotating black hole (Bardeen & Petterson, 1975). This could cause both the relativistic jet and the inner accretion disk to precess and create periodic (or quasi-periodic) variability in the optical light curve. Frequent misalignments between the accretion disk and black hole axis are theoretically expected to occur (Hopkins & Quataert, 2010; Hopkins et al., 2012). Graham et al. (2015b), using the results of Ulubay-Siddiki et al. (2009) and Tremaine & Davis (2014), find the precession period of a warped AGN disk is within an order of magnitude of the potential periods of our sources (assuming an SMBH mass of $10^8 M_\odot$). However, the precession is damped on a timescale that is short compared to typical AGN lifetimes (Tremaine & Davis, 2014; Graham et al., 2015b). Thus, Lense-Thirring precession in an AGN would be rarely observed.

Finally, and perhaps relatedly, the observed quasar periodicity might be caused by the same processes that cause quasi-periodic oscillations (QPOs) in black hole X-ray binaries (BHXBs—i.e., binary systems including a stellar mass black hole; for a recent review of black hole QPOs, see Motta, 2016). Graham et al. (2015b) noted that naively scaling the low-frequency ~ 1 Hz QPO of the $\sim 12 M_\odot$ microquasar GRS 1915+105 (see Yan et al., 2013, and references therein) to the estimated mass of PG 1302-102 yields a QPO period that overlaps the observed periodicity of PG 1302-102's optical light curve. On the other hand, with the physics of QPOs still uncertain, and the wide range of frequencies spanned by low-frequency QPOs for a given source (Wijnands & van der Klis, 1999), it is not clear that low-frequency QPOs scale linearly with black hole mass. As one example, Menou & Quataert (2001) note that ionization instabilities, one postulated source of QPOs in BHXBs, will be much more important for stellar mass binary black holes than for SMBHs. In addition, we note that recent work shows that QPOs in BHXBs appear more associated with the inverse Compton X-ray emission from the corona, and not with the thermal accretion disk component (e.g., Remillard & McClintock, 2006; Ingram et al., 2009; Ingram & Done, 2011). Quasars also have cooler accretion disks than BHXBs, with emission that peaks at rest-frame UV energies rather than the X-ray energies of BHXBs. Therefore, naively scaling the physics of QPOs from BHXBs to SMBHs might not produce periodic light curves at optical wavelengths.

2.4.3 Conclusions

We find no obvious differences between the X-ray spectra of the seven candidate sub-parcsec binary SMBHs in our sample and the X-ray spectra of the quasar population at large, at least over the energies observed by *Chandra*. Many theoretical models predict differences in the X-ray spectra of close binary SMBHs, though the models have a wide range of predictions, and the models are not all consistent with each other. Furthermore, most of the models investigate binaries with closer separations than we estimate for our sample. This implies inconclusive results from our survey: the observed sample may or may not indeed be sub-parsec binary SMBH systems.

For future work, analyses at other wavebands might be useful, such as monitoring the UV/optical spectra of candidate binary SMBHs for kinematic variability and periodicity, and/or searching for the proposed UV/optical "notch" in the spectral energy distribution due to the inner gap in the circumbinary accretion disk (Roedig et al., 2014). Note, however, that more recent simulations have failed to recover that gap (e.g., Farris et al., 2015a; d'Ascoli et al., 2018). Several models predict spectral hardening of binary SMBHs might lie at higher energies than the bands investigated by *Chandra*, so further investigations of candidate binary SMBH sources with *NuSTAR* is an enticing option. However, as some predicted signatures lie as far out as 100 keV (Roedig et al., 2014), it is unclear whether even *NuSTAR* will be able to detect them.

2.5 X-Ray Spectra of Sample

We include X-ray spectra for the full sample here, including the best fit models and resulting residuals (Figure 2.2).

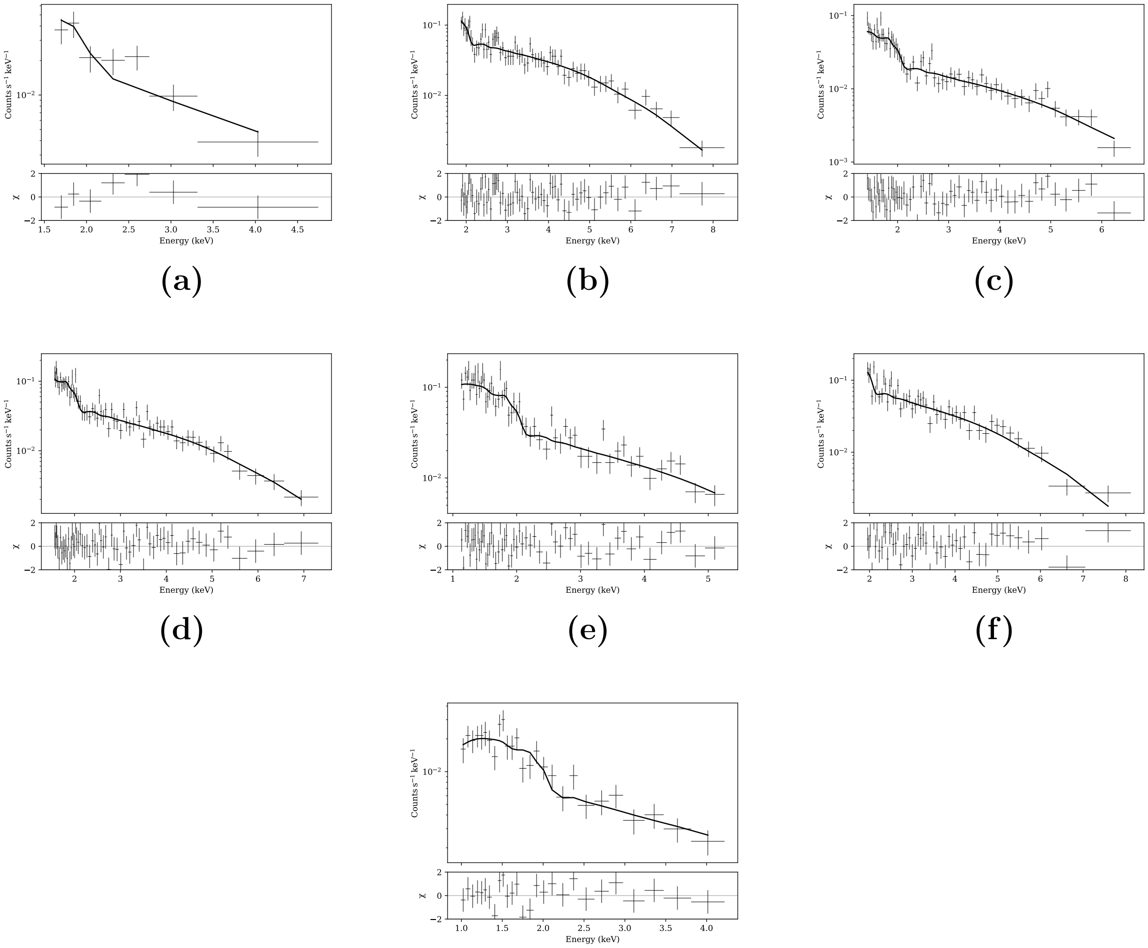

(a) **(b)** **(c)**

(d) **(e)** **(f)**

(g)

Figure 2.2 The *Chandra* X-ray spectra and best fit models of the seven quasars in the sample. The quasars are (a) 2MASSi J0411469+132416, (b) 2MASXi J0729087+400836, (c) RBS 874, (d) PG 1302-102, (e) FBQS J163302.6+234928, (f) Mrk 504, and (g) 4C +50.43. The spectra are plotted over the rest frame 2-10 keV band appropriate for each source's redshift. Error bars show 1σ confidence intervals.

CHAPTER 3

Searching for Newly Turned Off AGN in the 12μm Galaxy Sample[1]

3.1 Introduction

The presence of an actively accreting supermassive black hole (SMBH) in a galaxy is demonstrated through signatures of energetic processes near the central engine. In order of increasing distance from the black hole, the primary signs closest to the black hole are X-ray continuum from the hot corona (found within a few Schwarzschild radii of the SMBH; e.g., Zoghbi et al., 2012), and ultraviolet and optical emission lines with widths greater than $\sim 1500\,\mathrm{km\,s^{-1}}$ from the broad line region (BLR – found within 10s to 100s of light days from the SMBH; e.g., Kaspi et al., 2000, 2005). However, in heavily obscured active galactic nuclei (AGN) for which the line of sight hydrogen column density to the nucleus (N_{H}) exceeds $10^{23}\,\mathrm{cm^{-2}}$, these signatures are not visible. For AGN with a characteristic luminosity of $10^{43}\,\mathrm{erg\,s^{-1}}$ (i.e., Seyfert galaxies), 60% of sources are in this category (e.g., Burlon et al., 2011; Ricci et al., 2015).

Obscured AGN can still be identified through emission from further out from the central black hole, such as mid-infrared (MIR) thermal continuum from the dusty torus that is thought to surround the AGN accretion disk at distances of 0.1 pc − 10s of pc (e.g., Packham et al.,

---

[1] This Chapter reproduces Saade et al. (2022; ApJ, 936, 162) with the exception of an unrelated appendix, subject to formatting changes to adhere to the PhD thesis stylistic requirements.

2005; Radomski et al., 2008; Pott et al., 2010; Burtscher et al., 2013; Imanishi et al., 2016; García-Burillo et al., 2016; Gallimore et al., 2016), and the high ionization forbidden lines of the narrow line region (NLR) which occupies 100s to 1000s of pc scales (e.g., Netzer & Laor, 1993; Bennert et al., 2002, 2006; Müller-Sánchez et al., 2011; Ramos Almeida & Ricci, 2017). However, because the torus and NLR are further away from the black hole, it is possible for accretion onto the SMBH to be recently shut off but still preserve the MIR and NLR emission (e.g., within the last 10s to 100s of years; Ichikawa & Tazaki, 2017), creating an AGN that looks like a classical Seyfert 2 with the BLR obscured, but that in truth intrinsically lacks a BLR. This could be related to a so-called 'true' Seyfert 2 galaxy (e.g., Bianchi et al., 2008b). While so far in the literature these sources have been assumed to be actively accreting, the lack of a BLR could also be due to an AGN that has recently deactivated.

X-rays with energies greater than 10 keV can penetrate thick obscuring columns and reveal the presence of an actively accreting central engine even in a heavily obscured Seyfert 2 galaxy. As the first focusing X-ray telescope in orbit with sensitivity above 10 keV, the *Nuclear Spectroscopic Telescope Array* (*NuSTAR*; Harrison et al., 2013) has identified and studied actively accreting SMBHs obscured by even Compton-thick levels of absorption ($N_{\rm H} > 1.5 \times 10^{24}$ cm^{-2}; e.g., Annuar et al., 2015; Ricci et al., 2016; Boorman et al., 2016). *NuSTAR* thus gives us an opportunity to measure what fraction of the local Seyfert 2 population is currently accreting, and thereby constrain the AGN duty cycle.

To find Seyfert galaxies without a BLR requires a large sample of galaxies selected based on AGN signatures not blocked by obscuration, such as the warm dust from the torus. The most complete and brightest sample of such galaxies in the local universe are found in the 12 μm sample of galaxies (Spinoglio & Malkan, 1989; Rush et al., 1993). This sample contains all galaxies in the second *Infrared Astronomical Satellite* (*IRAS*; Neugebauer et al., 1984) point source catalogue that exceed 0.3 Jy in flux density at 12 μm that are also (a) brighter at 60 and 100 μm than at 12 μm, and (b) located at declinations $|\delta| \geq 25°$. Brightman &

Nandra (2008) investigated a subset of Seyfert 2 galaxies from this sample that appeared to be unabsorbed in the X-rays, finding two strong 'true' Seyfert 2 candidates, NGC 3147 and NGC 3660. The X-ray spectral properties of the full galaxy sample with *XMM-Newton* data were presented in Brightman & Nandra (2011a) and Brightman & Nandra (2011b). Of the Seyfert 2 galaxies in this sample, 10 showed anomalously low observed (i.e., not absorption-corrected) 2-10 keV X-ray luminosities compared to their nuclear [O III] luminosities. That is, these galaxies had observed 2-10 keV X-ray luminosities significantly less than expected for their observed [O III] luminosities based on our fit to the L_{2-10} to $L_{[\mathrm{OIII}]}$ relation for the 39 Seyfert 1 galaxies in the *IRAS* 12 μm sample with X-ray observations:

$$\log(L_{2-10}) = 0.95\ \log(L_{[\mathrm{OIII}]}) + 3.89, \tag{3.1}$$

where the luminosities are in units of $\mathrm{erg\,s^{-1}}$. The X-ray luminosities were derived directly from the observed 2-10 keV fluxes listed in Panessa et al. (2008), Brightman & Nandra (2011a), and Brightman & Nandra (2011b), while the [O III] luminosities were derived from fluxes listed in Malkan et al. (2017).

The 10 anomalously X-ray faint Seyfert 2 galaxies were an order of magnitude below this relation. This made them candidate Compton-thick AGN, but also potentially turned-off Seyfert 2 AGN if the central engines were inactive. High-energy X-ray observations, as possible with *NuSTAR*, can distinguish between these two scenarios. Of the 10 outlier galaxies, all but NGC 5953 had *NuSTAR* observations (Table 3.2.6) at the time of writing through a combination of archival data and dedicated observations from our Cycle 3 observing program (PID 3321). Three of the galaxies have already been reported as Compton-thick AGN in the literature based on these *NuSTAR* observations: NGC 1386 (Brightman et al., 2015), NGC 4922 (Ricci et al., 2017b), and IC 3639 (Boorman et al., 2016). However, since those publications, Baloković et al. (2018) has released the BORUS X-ray spectral model which is designed for analyzing high-energy observations of heavily obscured AGN, allowing us to more accurately constrain the parameters of the obscuring torus. Therefore, we analyze all 9 outlier galaxies with *NuSTAR* data, including those that have already appeared in the literature.

The 9 galaxies of the sample are plotted as the blue squares in Figure 3.1 alongside the solid red line of Equation 3.1. The dashed red line represents an order of magnitude below Equation 3.1. We use updated $L_{\text{[OIII]}}$ values from the literature instead of the original values from Malkan et al. (2017) from this point on, though we did use the original Malkan et al. (2017) values in the sample selection. For consistency's sake we use the reddening-corrected Brightman & Nandra (2011b) values for the [O III] luminosities when available. With the revised [O III] luminosities, NGC 5005 no longer lies more than an order of magnitude below the mean relation from Equation 3.1, though it did when using the Malkan et al. (2017) values for the original sample selection. Since the revised value is still very close to the selection line (see Figure 3.1), we keep this galaxy in the sample. NGC 5953 is plotted as an open blue square because it did not have *NuSTAR* observations at the time of writing and so did not end up in the final sample. The source of its [O III] luminosity is LaMassa et al. (2010). In addition to Equation 3.1 which is plotted in red, we also plot the intrinsic L_{2-10} vs intrinsic $L_{\text{[OIII]}}$ relation for Seyfert galaxies from Berney et al. (2015) in dark cyan. This relation is derived from 340 Seyfert 1 and Seyfert 2 galaxies in the BAT AGN Spectroscopic Survey Data Release 1 (Koss et al., 2017), and its RMS scatter is 0.59 dex, shown as the light blue shaded region.

For calculating the distance scales on our images, we adopt the concordance cosmology, $\Omega_{\text{M}} = 0.3$, $\Omega_{\Lambda} = 0.7$ and $H_0 = 70\ \text{km}\,\text{s}^{-1}\,\text{Mpc}^{-1}$. For computing luminosities in XSPEC (**Arnaud, 1996**), we use the default cosmology, which is $\Omega_{\text{M}} = 0.27$, $\Omega_{\Lambda} = 0.73$ and $H_0 = 70\ \text{km}\,\text{s}^{-1}\,\text{Mpc}^{-1}$. The 9 galaxies in this sample are very low redshift so the differences between the two cosmologies are negligible.

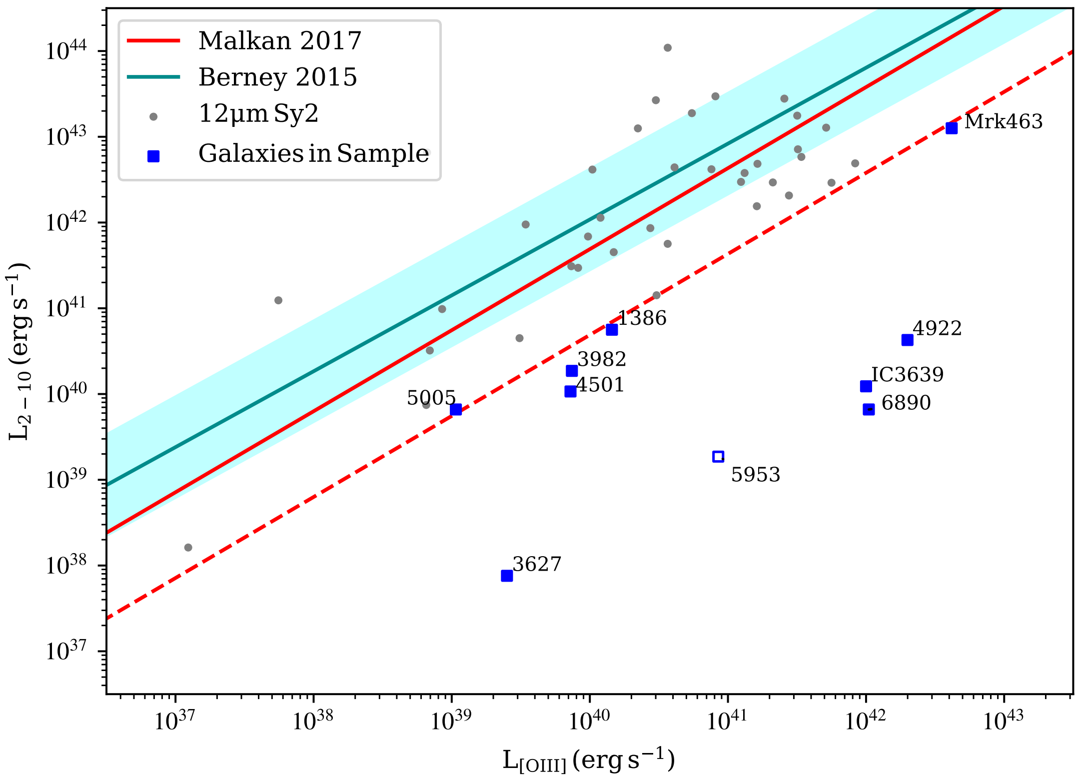

Figure 3.1 Observed 2-10 keV X-ray luminosity vs. [O III] luminosity for the 9 Seyfert 2 galaxies in our sample. The 12 μm sample, based on data from Malkan et al. (2017). The solid red line shows the mean L_{2-10} vs $L_{\mathrm{[OIII]}}$ relation for the Seyfert 1 galaxies in the 12 μm sample (Eq. 3.1). The dashed red line is the same line shifted by an order of magnitude down in observed 2-10 keV X-ray luminosity. The 9 galaxies of the sample are labeled as blue squares. NGC 5953 is plotted as an open square as it had no *NuSTAR* data available, and so was left out of the final sample. The L_{2-10} vs $L_{\mathrm{[OIII]}}$ relation for Seyferts from Berney et al. (2015) is plotted in dark cyan for comparison, with the shaded region corresponding to its RMS scatter of 0.59 dex.

3.2 X-Ray Observations and Analysis

The X-ray observations used in this paper are listed in Table 3.2.6. We include all available *NuSTAR* data for the 9 X-ray faint galaxies. *NuSTAR* observes at 3-79 keV, though most sources are not detected out to the highest energies where the sensitivity of *NuSTAR* declines. Lower energy X-ray data are important for the spectral analysis, and several telescopes provide focused soft X-ray observations (0.5-10 keV). Where available, we preferentially use archival *Chandra* observations, due to their sensitivity and high spatial resolution. With its $1'$ beam (half-power diameter), *NuSTAR* suffers confusion of off-nuclear point sources with the central AGN, which is particularly problematic for faint nuclei, as is the case for several of the galaxies analyzed here. When *Chandra* data were not available or were insufficient for understanding the true nature of some spectral features, we use archival *Swift* and/or *XMM-Newton* data.

All X-ray spectra were grouped with a minimum of one count per bin. We fit the data in XSPEC (version 12.11.1). Due to the low number of counts for all sources, the C-statistic was used for fitting. We subtracted the background instead of modeling it separately, in which case XSPEC uses the modified W-statistic. We next describe the X-ray observations by each satellite in more detail.

3.2.1 *NuSTAR*

By design, the entire sample presented here has *NuSTAR* observations obtained from the HEASARC archive[2]. The *NuSTAR* data were reduced, filtered, and extracted using HEASOFT[3] (Nasa High Energy Astrophysics Science Archive Research Center (Heasarc), 2014) version 6.28, the *NuSTAR* Data Analysis Software[4] (NUSTARDAS; version 2.0.0), and the

---

[2] `https://heasarc.gsfc.nasa.gov/docs/archive.html`

[3] `https://heasarc.gsfc.nasa.gov/ftools/`

[4] `https://heasarc.gsfc.nasa.gov/docs/nustar/analysis/`

NuSTAR calibration database[5] (CALDB; version 20200826). For the extractions, we used circular source regions 40" in radius centered on the galaxy nucleus positions and circular background regions 100" in radius. In the spectral fitting, we fixed the *NuSTAR* normalization constant to unity for FPMA and 1.04 for FPMB, where the latter is based on calibration observations of the bright source 3C 273 reported in Madsen et al. (2015). When multiple FPMA and FPMB observations were available, the normalization constants in the later observations were left as free parameters to account for variability. We used energies from 3 keV to 30 keV from the *NuSTAR* data for the spectral fitting. Above 30 keV background dominates over AGN emission for our sample.

3.2.2 *Chandra*

Chandra ACIS observations were available for 8 of the 9 galaxies from the Chandra Data Archive[6], with the exception being NGC 6890. For most of this sample of X-ray faint, nearby galaxies, the sensitive, higher angular resolution *Chandra* observations identify multiple sources within the *NuSTAR* beam, primarily due to X-ray binaries within the target galaxies. Using CIAO (Fruscione et al., 2006) version 4.12 and the *Chandra* CALDB[7] version 4.9.1, we extracted *Chandra* spectra of all sources within a 40" radius circular aperture around the core of each galaxy, matching the *NuSTAR* beam. As discussed in the following discussion of individual sources, the *Chandra* aperture sizes varied depending on whether the source was unresolved and/or if the target was at a larger off-axis angle, for which the *Chandra* point spread function degrades. Sources in the *Chandra* images were identified by eye. A circular background region 10" in radius was used for all *Chandra* data. We used energies from 0.5 keV to 8.0 keV from the *Chandra* data for the spectral fitting, and ignored off-nuclear sources with less than 10% the net count rate of the central AGN. We used all

---

[5] https://heasarc.gsfc.nasa.gov/docs/heasarc/caldb/nustar/

[6] https://cxc.harvard.edu/cda/

[7] https://cxc.cfa.harvard.edu/caldb/

archival *Chandra* data available for these sources, with the exception of NGC 3627, which had a 1.3 ks observation (ObsID: 394) that was ultimately discarded in favor of a much deeper observation (50.3 ks; ObsID: 9548).

3.2.3 *Swift*

Because NGC 6890 lacked *Chandra* observations, we analyzed data from the X-Ray Telescope (XRT) on *Swift* for this galaxy. The data were obtained from the HEASARC archive. We extracted the data using HEASOFT version 6.28, the *Swift* XRT Data Analysis Software[8] (SWXRTDAS; version 3.6.0), and the *Swift* CALDB[9] version 20200724. We used circular source regions of 25" radius and background regions of 50" radius for the spectral extraction. We used energies from 0.3 keV to 10.0 keV from the *Swift* data for the spectral fitting.

3.2.4 *XMM-Newton*

We used *XMM-Newton* data from the *XMM-Newton* Science Archive[10] for NGC 5005 and NGC 6890, the former to further investigate unusual spectral features found in the *NuSTAR* data, and the latter because no *Chandra* observations exist for the source. We used all three of the European Photon Imaging Camera (EPIC) CCDs — i.e., pn, MOS1, and MOS2 — in the spectral fitting. We extracted the data using the *XMM-Newton* Scientific Analysis System (SAS, version 18.0.0; Gabriel et al., 2004). Details on the *XMM-Newton* spectral extractions are in the individual notes on each galaxy (§3). We used energies from 0.2 keV to 10.0 keV from the *XMM-Newton* data for the spectral fitting.

---

[8] `https://swift.gsfc.nasa.gov/analysis/`

[9] `https://heasarc.gsfc.nasa.gov/docs/heasarc/caldb/swift/`

[10] `http://nxsa.esac.esa.int/nxsa-web`

3.2.5 X-ray Spectral Models

For each galaxy spectrum we began fitting with a simple CONSTANT*TBABS*POWERLAW model in XSPEC. The constant is to account for source variability and cross-normalization differences between the different telescopes; in the text, we refer to this constant as either the cross-calibration coefficient or the normalization constant. The TBABS (Wilms et al., 2000) component models absorption of X-rays due to the interstellar medium of our own Milky Way galaxy, which we determined using the Galactic hydrogen column densities along the line of sight to each galaxy from HI4PI Collaboration et al. (2016). The POWERLAW[11] component fits a simple powerlaw to the data with two parameters: the spectral index, Γ, and the normalization, defined as the number of photons $\mathrm{keV^{-1}\,cm^{-2}\,s^{-1}}$ at 1 keV in the source reference frame. In luminous, unobscured AGN, Compton upscattering of thermal photons from the accretion disk by the SMBH corona generates a powerlaw X-ray spectrum across our observed range, and this component dominates the X-ray spectrum. In obscured AGN, this component is absorbed by gas, making the observed X-ray spectrum harder (i.e., a lower value of Γ). For heavily absorbed, Compton-thick AGN, few photons from the intrinsic spectrum escape below 10 keV. However, a small fraction of the intrinsic powerlaw generally always escapes (e.g., Gupta et al., 2021). This scattered, unabsorbed powerlaw component is typically just a few percent of the intrinsic spectrum.

In addition to this simple initial model, AGN, especially those with heavy absorption, may exhibit a soft excess in the 0.5-2 keV range that is thought due to thermal emission from hot gas along the line of sight. We account for this by adding an APEC (Smith et al., 2001) model, which simulates X-ray emission from a collisionally ionized plasma. Its parameters are the plasma temperature, elemental abundances, and normalization. The APEC normalization is defined as $\frac{10^{-14}}{4\pi[D_A(1+z)]^2}\int n_e N_{\mathrm{H}} dV$, where D_A is the angular diameter distance to the source, and n_e and N_{H} are the electron and hydrogen number densities, respectively. For this

---

[11] `https://heasarc.gsfc.nasa.gov/xanadu/xspec/manual/node216.html`

analysis, we set the elemental abundances to solar.

Obscured AGN also typically show a prominent neutral Fe K-alpha line at 6.4 keV and a Compton hump at $\sim$ 20 keV. These features arise from reflected emission and scattering off gas around the central engine. The gas is believed to be toroidal in geometry and is presumed related to the cooler, more extended dusty torus that is responsible for AGN obscuration at visible wavelengths and AGN thermal emission at MIR wavelengths. We fit the iron line and Compton hump by adding a BORUS model to the overall spectral model, which allows us to constrain the geometry of the torus. BORUS models torus reprocessing of an intrinsic SMBH corona powerlaw spectrum. Its free parameters are the spectral index of the intrinsic powerlaw (Γ), the high-energy cutoff, the torus hydrogen column density (N_{H}), the torus covering factor (defined as the cosine of the opening angle of the torus), the inclination angle of the torus (θ_{inc}), the relative abundance of iron compared to the solar abundance, and the normalization (which is defined the same as it is for the POWERLAW model). We consistently set the high energy cutoff to 500 keV and the iron abundance to solar. We also set the spectral indices of the BORUS model and the POWERLAW model to be the same in all cases except NGC 6890. In the case of an AGN with a BORUS component, the POWERLAW component represents the fraction of the intrinsic powerlaw that is scattered and transmitted through the torus, and so it should have the same spectral index as the BORUS component.

We also tried including a ZTBABS (Wilms et al., 2000) model in our fits. ZTBABS is similar to TBABS but represents absorption from hydrogen at the source, rather than from our Galaxy. However, though we investigated including a ZTBABS component for all of the AGN in this sample, none of the sources ultimately required it. As noted below, a few of the extranuclear X-ray sources did find improved spectral fitting by including a ZTBABS component.

For NGC 5005 we tried a ZGAUSS[12] component in addition to a BORUS component. This model represents a Gaussian emission line profile. Its free parameters are the source frame line energy in keV, the source frame line width in keV, the redshift to the source, and the normalization (which is defined as the total photons $\mathrm{cm}^{-2}\,\mathrm{s}^{-1}$ in the emission line in the source frame). A ZGAUSS model was ultimately preferred over a BORUS model for this source.

Lastly, for NGC 3627 we used a CUTOFFPL[13] instead of a POWERLAW component for the extranuclear point sources in the *NuSTAR* beam. This model component is the same as the POWERLAW component except it includes an exponential rolloff, $KE^{-\Gamma}\,\exp(-E/\beta)$, where K is the normalization, E is the energy, Γ is the spectral index, and β is the the e-folding energy of the rolloff.

3.2.6 Measuring X-ray Luminosities

We measured the intrinsic X-ray luminosities from the BORUS normalization and Γ (which was fixed to the POWERLAW Γ for all but NGC 6890). We derived the errorbars on the intrinsic luminosities by turning the upper and lower errors on the BORUS Γ and norm into fractional errors and then added fractional errors on each of the two parameters in quadrature to derive the fractional error on the luminosities.

For NGC 3627 and NGC 5005 (for which BORUS components were not used), we added a CFLUX component to the POWERLAW components of their models. This component calculates the flux of the model component it is added to when the spectrum is fitted. We then converted the fluxes to luminosities using the Local-Group-corrected redshift distances listed in NED. The errors on intrinsic luminosity for these galaxies were derived from the 90% confidence intervals reported by the CFLUX component.

---

[12] https://heasarc.gsfc.nasa.gov/xanadu/xspec/manual/node176.html

[13] https://heasarc.gsfc.nasa.gov/xanadu/xspec/manual/node161.html

Table 3.1. List of X-ray observations.

Target	R.A., Dec. (J2000)	Observatory	ObsID	Date	Net Exposure Time (ks)	Net Count Rate (cts ks^{-1})
NGC 1386	03:36:46.18, −35:59:57.87	*Chandra*	4076	2003-11-19	19.6	52.5
		-	12289	2011-4-13	17.3	48.7
		-	13185	2011-4-13	29.7	45.4
		-	13257	2011-4-14	33.8	47.0
		NuSTAR	60001063002	2013-7-9	18.8/18.4	9.2/10.2
		-	60201024002	2016-5-11	25.4/25.8	9.9/9.2
NGC 3627	11:20:14.96, +12:59:29.54	*Chandra*	9548	2008-3-31	49.6	6.1
		NuSTAR	60371003002	2017-12-23	49.1/48.9	3.3/2.3
NGC 3982	11:56:28.13, +55:07:30.86	*Chandra*	4845	2004-1-3	9.2	6.6
		NuSTAR	60375001002	2017-12-5	30.7/31.0	5.8/4.7
NGC 4501	12:31:59.161, +14:25:13.39	*Chandra*	2922	2002-12-9	17.1	11.7
		NuSTAR	60375002002	2018-1-28	58.0/59.4	4.2/3.4
		-	60375002004	2018-5-24	58.5/58.2	3.5/3.7
IC 3639	12:40:52.85, −36:45:21.11	*Chandra*	4844	2004-3-7	8.7	31.5
		NuSTAR	60001164002	2015-1-9	56.1/55.7	8.3/8.1
NGC 4922	13:01:24.90, +29:18:40.0	*Chandra*	4775	2004-11-2	3.8	11.8
		-	15065	2013-11-2	14.9	9.3
		-	18201	2016-3-6	5.8	10.7
		NuSTAR	60101074002	2015-11-9	20.2/20.1	4.2/2.8
NGC 5005	13:10:56.23, +37:03:33.14	*Chandra*	4021	2003-8-19	4.92	54.3
		XMM-Newton	0110930501	2002-12-12	8.7/13.1/13.1	297.5/69.1/70.9
		NuSTAR	60001162002	2014-12-16	48.9/48.3	5.8/5.4
Mrk 463	13:56:02.87, +18:22:19.48	*Chandra*	4913	2004-6-11	49.3	24.3[a]
		-	18194	2016-3-10	9.8	16.1[a]

Table 3.1 (cont'd)

Target	R.A., Dec. (J2000)	Observatory	ObsID	Date	Net Exposure Time (ks)	Net Count Rate (cts ks^{-1})
NGC 6890	20:18:18.10, −44:48:24.21	*NuSTAR*	60061249002	2014-1-1	23.9/23.8	2.3/2.2
		XMM-Newton	0301151001	2005-9-29	0.9/7.5/7.8	131.1/26.3/28.3
		Swift	00088188001	2018-3-6	1.7	11.13
		-	00088188002	2018-5-25	2.0	20.1
		NuSTAR	60375003002	2018-5-25	34.6/34.5	59.5/56.2

Note. — Net count rates for *Chandra* data are for the AGN core only. Exposure times and net count rates for *NuSTAR* observations are FPMA/FPMB. Exposure times and net count rates for *XMM-Newton* observations are pn/MOS1/MOS2.

[a] For the brighter, eastern component of this merger system (see § 3.3.8).

3.3 The Individual Galaxies

We now discuss each of the nine galaxies in our sample individually, providing notes about each one and then details of the X-ray observations and analysis.

3.3.1 NGC 1386

NGC 1386 is a barred spiral galaxy in the Fornax Cluster (Ferguson, 1989) with prominent dust lanes, a ring of H II regions, and AGN-ionized gas plumes visible in *Hubble* imagery of its central regions (Ferruit et al., 2000). It is optically classified as a Seyfert 2 galaxy (e.g., Phillips & Frogel, 1980; Brightman & Nandra, 2011b) but it has also been classified as a S1i by Véron-Cetty & Véron (2006) on the basis of a broad Paschen-beta (Paβ) component evident in its near-infrared (NIR) spectrum. Ruschel-Dutra et al. (2014) did not find polycyclic aromatic hydrocarbon (PAH) features in its *Spitzer* nuclear spectrum, likely attributable to ionization by the AGN. The AGN is a water megamaser source (Braatz et al., 1997); such sources typically show higher levels of obscuration (e.g., Zhang et al., 2006; Masini et al., 2016).

Lena et al. (2015) reports that NGC 1386 has a mass outflow rate of $> 1 M_\odot\,\mathrm{yr}^{-1}$ and shows complex gas kinematics at its center, likely caused by an ionization cone intersecting the galactic disk at an angle. Rodríguez-Ardila et al. (2017) found even stronger outflows, comparable to that of a strong AGN, with a mass loss rate of $11 M_\odot\,\mathrm{yr}^{-1}$. The outflow takes the form of two expanding shells of gas that are coincident with the axis of the radio emission, implying they are likely powered by a radio jet rather than simply by the AGN radiation. Between the broad Paβ emission line and the radio maser activity, the broadband properties of NGC 1386 suggest a currently active, obscured Seyfert 2 galaxy.

In the X-rays, Guainazzi et al. (2005a) concluded the *XMM-Newton* spectrum was best fit by either scattering and transmission components, or by thermal and reflection components. Bianchi et al. (2006) confirmed a reflection-dominated model was the best fit based on

Chandra data, but concluded spectral lines visible in the soft X-ray EPIC observations were more likely due to scattering off of photoionized plasma rather than thermal emission. LaMassa et al. (2012) presented a joint analysis of *Chandra* and *XMM-Newton* data in the 0.5-2.0 keV range and found that it was best fit with a two-temperature APEC model, indicating the presence of two thermal gas components, one with $kT \sim 0.13$ keV and one with $kT \sim 0.67$ keV. They noted this was similar to X-ray observations of starburst galaxies (e.g., Dahlem et al., 1998; Strickland et al., 2004). In addition to two APEC components, their model also contained two powerlaw components with spectral indices tied together, each subject to both Galactic absorption and absorption at the source. The latter was found to be $N_\mathrm{H} = 3.14 \times 10^{23}\,\mathrm{cm}^{-2}$, and LaMassa et al. (2012) measured the AGN contribution to the 0.5-2.0 keV X-ray luminosity to be $\approx 70\%$. Recently, Jones et al. (2021) reported *Chandra* detection of extended hard X-ray emission across the ionization cones of NGC 1386.

Brightman & Nandra (2011a) identified NGC 1386 as Compton-thick on the basis of its *XMM-Newton* data, which shows a strong Fe K-alpha line ($\mathrm{EW}_{6.4} = 1710$ eV in their model). They confirmed it was reflection-dominated, and measured a hydrogen column density of $N_\mathrm{H} = 1.51 \times 10^{24}\mathrm{cm}^{-2}$. Adding data taken by *NuSTAR* to the existing *XMM-Newton* spectra, Brightman et al. (2015) found a slightly higher column density, $N_\mathrm{H} = 5.61 \times 10^{24}\,\mathrm{cm}^{-2}$. Masini et al. (2016) found similar results using a combination of a MyTORUS model (Murphy & Yaqoob, 2009) and an emission line component at 6.5 keV.

3.3.1.1 X-ray Observations and Data Extraction

NGC 1386 was observed twice by *NuSTAR* and four times by *Chandra*; details, including observation dates and exposure times, are in Table 3.2.6. Figure 3.2 presents the third *Chandra* observation and the second *NuSTAR* FPMA observation with the extraction regions overlaid.

The AGN *Chandra* spectrum was extracted with a circular source region 5.7" in radius. In

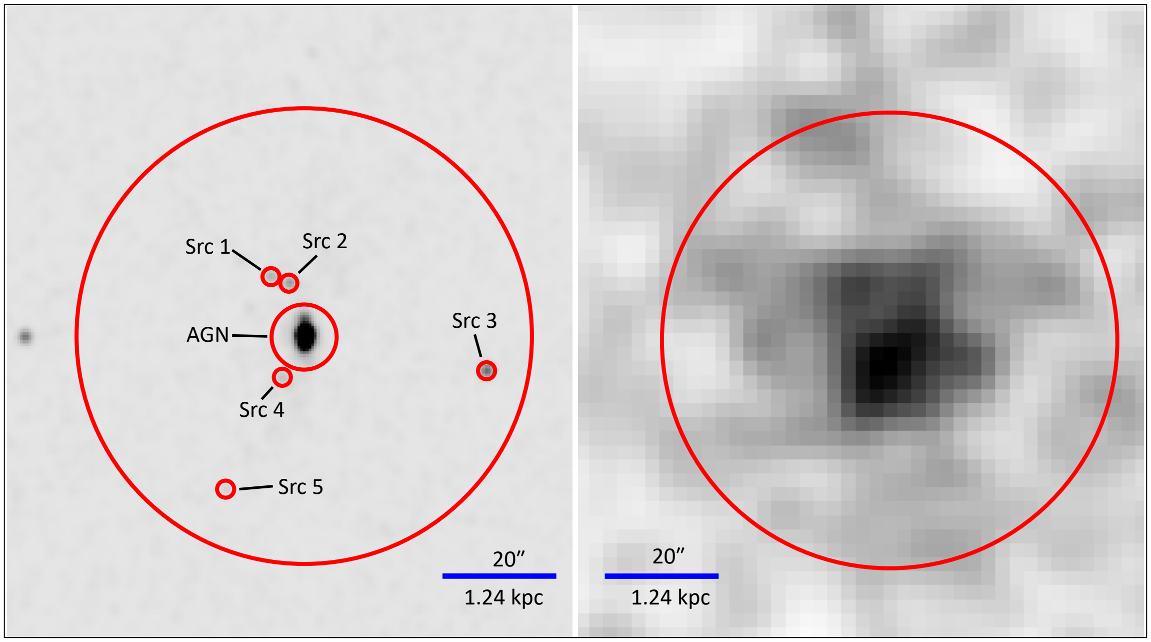

Figure 3.2 *Chandra* (ObsID: 13257) and *NuSTAR* (ObsID: 60201024002) FPMA images of NGC 1386. The larger, 40" radius circle denotes the *NuSTAR* extraction region, while the smaller circles denote the *Chandra* extraction regions. Five extra-nuclear point sources were visible in the *Chandra* observations, though all were sufficiently faint (i.e., $<$ 10% the flux of the nucleus) to be ignored in the AGN spectral analysis.

addition to the AGN core, five extranuclear point sources in the *NuSTAR* beam were present in all four *Chandra* images. They were extracted using circular source regions 1.5" in radius. Since the count rates for all these sources were less than 10% that of the core, they were ignored in the X-ray spectral fitting.

3.3.1.2 X-ray Spectral Fitting

We first modeled the spectrum with TBABS*POWERLAW, which yielded a C-stat/d.o.f. of 2980.46/1698. A strong Fe K-alpha emission line is evident in the unfolded spectrum (Figure 3.3), as well as a prominent Compton hump at 10-20 keV. We added a BORUS component to the original TBABS*POWERLAW fit to account for these reflection features, fixing the spectral index of the BORUS component to that of the POWERLAW component. This improved C-stat/d.o.f. to 2067.40/1694. Strong residuals above the power law component were present at energies 0.5-2.0 keV so an APEC component was added, resulting in C-stat/d.o.f. = 1679.64/1692. While this is a statistically good fit, $N_{\rm H}$ remains unconstrained. We therefore opted to freeze $\cos(\theta_{\rm inc})$ at its model value of 0.45 before refitting. The final fit had C-stat/d.o.f. = 1681.69/1693 and the parameters of the best-fit model are presented in Table 3.3.1.2. The 90% confidence interval for the BORUS parameter $\log N_{\rm H}$ was unconstrained at the upper end, so it is listed as ≥ 24.5. The powerlaw spectral index hit the upper bound of 2.6 in the model, so it is listed as ≥ 2.6. The best-fit model is plotted over the unfolded spectrum in Figure 3.3. The logarithm of the 2-10 keV luminosity (in units of $\mathrm{erg\,s^{-1}}$) measured from the model is 42.29 ± 0.05.

Table 3.2. Parameters for best-fit NGC 1386 model.

APEC		BORUS				POWERLAW	
kT (keV)	Norm (10^{-5} cts s^{-1} keV^{-1})	$\log(N_H)$[a]	CF_{Tor}[b]	$\cos(\theta_{inc})$[c]	Norm (cts s^{-1} keV^{-1})	Γ	Norm (10^{-5} cts s^{-1} keV^{-1})
0.82 ± 0.03	$2.28^{+0.44}_{-0.38}$	≥ 24.5	0.49 ± 0.01	$= 0.45$[d]	0.09 ± 0.01	≥ 2.6	$5.65^{+0.98}_{-0.38}$

Note. — Error bars represent 90% confidence intervals. The *Chandra* normalization constant values were $0.91^{+0.16}_{-0.13}$ (ObsID: 4076), $0.97^{+0.17}_{-0.14}$ (ObsID: 12289), $0.90^{+0.15}_{-0.10}$ (ObsID: 13185), and $0.53^{+0.16}_{-0.08}$ (ObsID:13527). The second *NuSTAR* FPMA and FPMB normalization constants were $0.99^{+0.15}_{-0.11}$ and $0.98^{+0.16}_{-0.11}$ (ObsID: 60201024002).

[a] N_H in units of cm^{-2}.

[b] Covering factor of torus, equivalent to cosine of torus opening angle.

[c] Cosine of torus inclination angle.

[d] Frozen at this value.

3.3.2 NGC 3627

NGC 3627 (also known as Messier 66) is a barred spiral galaxy in the Leo triplet of galaxies, along with NGC 3623 and NGC 3628, and is undergoing tidal interactions with them (Schmelz et al., 1987; Hughes et al., 1991; Zhang et al., 1993; Reuter et al., 1996). It exhibits low-luminosity nuclear activity, though its status as a true SMBH-powered AGN (as opposed to simply having a nuclear starburst) has been the subject of debate in the literature. Its optical activity type has been variously characterized as a transition object (e.g. Dudik et al., 2005), Seyfert 2 (e.g. Brightman & Nandra, 2011b), incapable of being distinguished between the transition object and Seyfert 2 classes (Ho et al., 1997), or simply a LINER (Véron-Cetty & Véron, 2006).

NGC 3627 presents a complex profile in the MIR, with diffuse emission across the entire galaxy (Asmus et al., 2014) from which a compact nuclear source cannot be clearly separated.

In the X-rays, NGC 3627 was first detected by *ASCA* and *ROSAT*. Roberts et al. (2001) examined these observations and found that the spectrum was described well by a soft thermal component (0.5-1 keV) and a powerlaw component (2-5 keV). They measured the flux ratio between these components to be 0.56, and argued that this indicated the two spectral components likely had a common, non-AGN origin. They noted this flux ratio was very similar to the *ASCA* flux ratio in the same energies for the starburst galaxy NGC 253. Therefore, they argued that NGC 3627 was unlikely to be a true AGN.

The first *Chandra* observation of NGC 3627, a 1.3 ks snapshot exposure, was initially published by Ho et al. (2001), who did not detect a dominant unresolved point source in the galaxy's core, only a group of sources. They therefore concluded that NGC 3627 was not a true AGN. Some later papers also suspected NGC 3627 not to be a true AGN, partially on this basis (e.g. Panessa et al., 2006; González-Martín et al., 2009b); Panessa et al. (2006) put an upper limit of $L_{2-10} < 7.6 \times 10^{37}\,\mathrm{erg\,s^{-1}}$ on the nuclear 2-10 keV luminosity. In contrast,

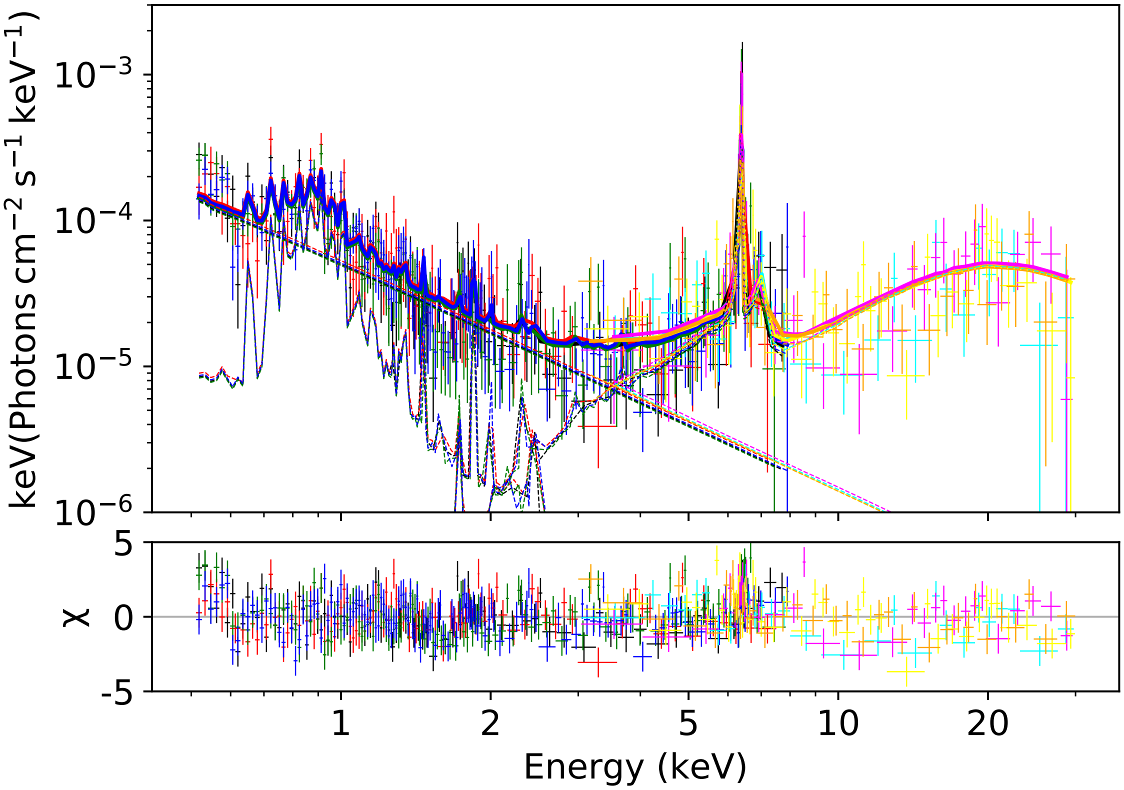

Figure 3.3 Unfolded spectrum and best-fit model for NGC 1386. Black, red, green, and blue denote *Chandra* data (ObsIDs 4076, 12289, 13185, and 13257). Cyan and magenta denote FPMA and FPMB data for *NuSTAR* observation 60001063002. Yellow and orange denote FPMA and FPMB for *NuSTAR* observation 60201024002.

and based on the same observations, Zhang et al. (2009) argued the *Chandra* image does show a dominant central point source within 1” of the galaxy’s center, and they report a significantly higher 0.3-8 keV X-ray luminosity of $L_{0.3-8} = 9.1 \times 10^{39}\,\mathrm{erg\,s^{-1}}$.

In NGC 3627’s sole *XMM-Newton* observation, Panessa et al. (2006) observed a point source at the galaxy nucleus, but noted it was equal in brightness to a second point source 10” away. Indeed, both Panessa et al. (2006) and Hernández-García et al. (2013) agree the *XMM-Newton* data is heavily contaminated by emission from sources other than the galaxy core. González-Martín et al. (2009b) failed to find a unresolved point source in the harder bands observed by *XMM-Newton* (4.5-8.0 keV). Their estimate of the 2-10 keV luminosity is $L_{2-10} \sim 10^{39}$ erg s^{-1} based on the *XMM-Newton* data, assuming a powerlaw index of $\Gamma = 1.8$ and Galactic absorption. They nonetheless identified NGC 3627 as a Compton-thick AGN candidate on the basis of its $L_{2-10}/L_{[\mathrm{OIII}]}$ ratio (González-Martín et al., 2009a). In contrast, Brightman & Nandra (2011a) measured an ionized hydrogen column density of $5.01\times10^{21}\,\mathrm{cm^{-2}}$ in the *XMM-Newton* spectrum, which would clearly place it in the Compton-thin regime. Brightman & Nandra (2011a) modeled the *XMM-Newton* observation of NGC 3627 with a soft thermal emission component and ionized absorber component in addition to Galactic absorption and powerlaw components.

A second, deeper (50.3 ks) *Chandra* observation of NGC 3627 was taken in 2008 (Grier et al., 2011). In this observation, one can see an unresolved nuclear point source embedded in diffuse emission (Cisternas et al., 2013).

Esparza-Arredondo et al. (2020) fit the *NuSTAR* data for NGC 3627 with a partial covering absorber that included Galactic absorption. They measured an absorbing hydrogen column density of $1.8 \times 10^{24}\,\mathrm{cm^{-2}}$, which would put the AGN in the Compton-thick category. After correction for absorption they classified NGC 3627 as an AGN in the early stages of fading based on it being under-luminous in X-rays compared to the MIR. In their interpretation, NGC 3627 is observed at the beginning of the fading arc of the AGN duty cycle.

Brightman & Nandra (2011b) plot NGC 3627 on several Baldwin, Phillips, and Terlevich (BPT) diagrams (Baldwin et al., 1981). The position of NGC 3627 on the BPT diagram is an AGN if using [O III]/Hβ vs. [N II]/Hα, a LINER if it is using [O III]/Hβ vs. [S II]/Hα, and a Seyfert 2 if using [O III]/Hβ vs. [O I]/Hα. We therefore adopt its optical classification as an AGN based on previous work.

3.3.2.1 X-ray Observations and Data Extraction

NGC 3627 has been observed by *Chandra* twice, for 1.3 ks on 1999 November 3 (ObsID: 394) and for 50.3 ks on 2008 March 31. Given that the first, significantly shorter exposure does not clearly detect any sources at the galaxy center, we ignore those data in our analysis. Table 3.2.6 presents details of the latter *Chandra* observation, as well as the single *NuSTAR* observation of this galaxy to date.

The *Chandra* and *NuSTAR* FPMA images of NGC 3627 are shown in Figure 3.4. There are a large number of sources visible in the *Chandra* image, with one diffuse, irregularly shaped source associated with the nucleus. In addition, there is a bright point source approximately $1.5'$ to the southeast whose brightness dwarfs that of the nucleus as well as the numerous point sources within the *NuSTAR* beam (Figure 3.5). This source, associated with the ultraluminous X-ray source (ULX) M66 X-1 (Walton et al., 2011), dominates in the *NuSTAR* image, while the AGN, in contrast, is not clearly visible. Indeed, we used the *Chandra*-derived astrometric offset between the ULX and the AGN to place the AGN extraction aperture in the *NuSTAR* image.

Figure 3.5 presents a zoomed-in version of the *Chandra* image, highlighting the 22 off-nuclear point sources visible within the *NuSTAR* beam. The *Chandra* AGN spectrum was extracted using a circular source region 2.55" in diameter. The off-nuclear point sources were extracted using circular source regions 1.5" in diameter for sources 3, 5, 8, 12, 14, and 20; 1.2" in diameter for sources 4, 11, 15, 18, and 19; and 1" in diameter for the remaining sources.

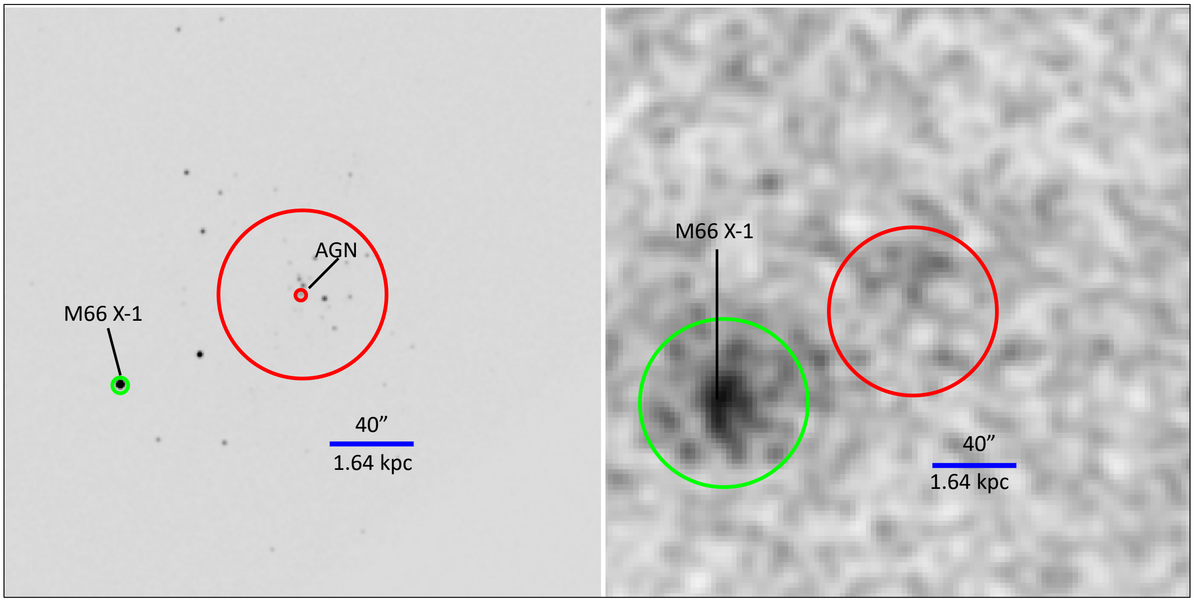

Figure 3.4 *Chandra* (left; ObsID: 9548) and *NuSTAR* FPMA (right) images of NGC 3627. The larger, 40” radius red circle denotes the *NuSTAR* extraction region for the AGN, while the smaller red circle denotes the *Chandra* extraction region for the AGN. The ULX M66 X-1 is highlighted with a green circle (3.75” diameter in *Chandra*; 40” radius in *NuSTAR*). M66 X-1 dominates the *NuSTAR* image, while the AGN is not clearly detected by *NuSTAR*.

Because the nucleus is so faint, 15 *Chandra* point sources within the *NuSTAR* beam are brighter than 10% of its count rate. For all other galaxies in our sample, we do joint fitting of the AGN and all off-nuclear point sources within the *NuSTAR* beam above that threshold. However, fitting this many sources jointly would be prohibitive and most of the *Chandra* flux within the *NuSTAR* beam comes from the brightest of these off-nuclear sources. Therefore, only the ten brightest point sources are included in the spectral fitting (i.e., sources 4, 5, 7, 8, 9, 10, 12, 14, 15, and 20).

3.3.2.2 X-ray Spectral Fitting

Due to the large number of point sources present in the *NuSTAR* beam, we first fit the off-nuclear point sources with their *Chandra* data alone. We then initially fit this galaxy with all

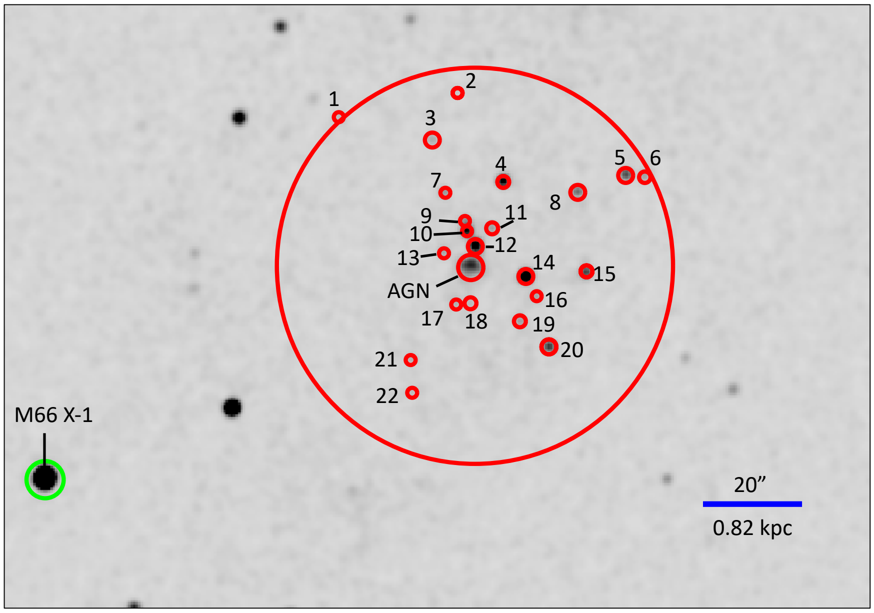

Figure 3.5 Zoomed-in and re-scaled *Chandra* image of NGC 3627 highlighting and labeling the plethora of off-nuclear point sources (small red circles) within the larger 40" radius *NuSTAR* beam. The ULX M66 X-1 is visible to the southeast (green circle).

parameters for the off-nuclear sources frozen based on their *Chandra* data, thereby avoiding having too many free parameters which can lead to parameter values being implausibly high or low.

We started with a simple model consisting of a CONSTANT, a TBABS component frozen to the Galactic hydrogen column density, and 11 POWERLAW components, one for the AGN and one for each of the 10 brightest point sources, where the latter were frozen to the best-fit values from *Chandra*. This yielded a C-stat/d.o.f. of 1422.72/1347. However, this fit substantially overestimated the brightness of the *NuSTAR* data, likely because several of the off-nuclear point sources had hard spectra over the *Chandra* range that overestimated their brightness at the higher energies of *NuSTAR*.

We therefore decided to change the POWERLAW component in the extra point sources to a CUTOFFPL model. We started with the high-energy cutoffs frozen at 500 keV for all the sources, and tested whether thawing each one would decrease C-stat or not. Out of all the sources, only thawing the cutoffs on Sources 5, 8, 12, and 14 improved the fit. This fit had a C-stat/d.o.f. of 1182.16/1318.

We fit the initial model with Sources 5, 8, 12 and 14's high-energy cutoffs thawed, then froze the high-energy cutoffs before refitting. We then added an APEC component to the model, as there is an excess between 0.5 and 2 keV. This led to a C-stat/d.o.f. of 1154.65/1320. The final parameter values are tabulated in Table 3.3.2.2. The spectrum and best fit final model are plotted in Figure 3.6. The logarithm of the 2-10 keV luminosity (in units of $\mathrm{erg\,s^{-1}}$) measured from the model is $38.38^{+0.16}_{-0.10}$.

3.3.3 NGC 3982

NGC 3982 is a barred spiral galaxy, classified as a Seyfert 1.9 since it possesses broad Hα but lacks broad Hβ in its optical spectrum (e.g. Ho et al., 1997; Véron-Cetty & Véron, 2006). Seyfert 1.9 galaxies are believed to be highly obscured, and are often lumped together

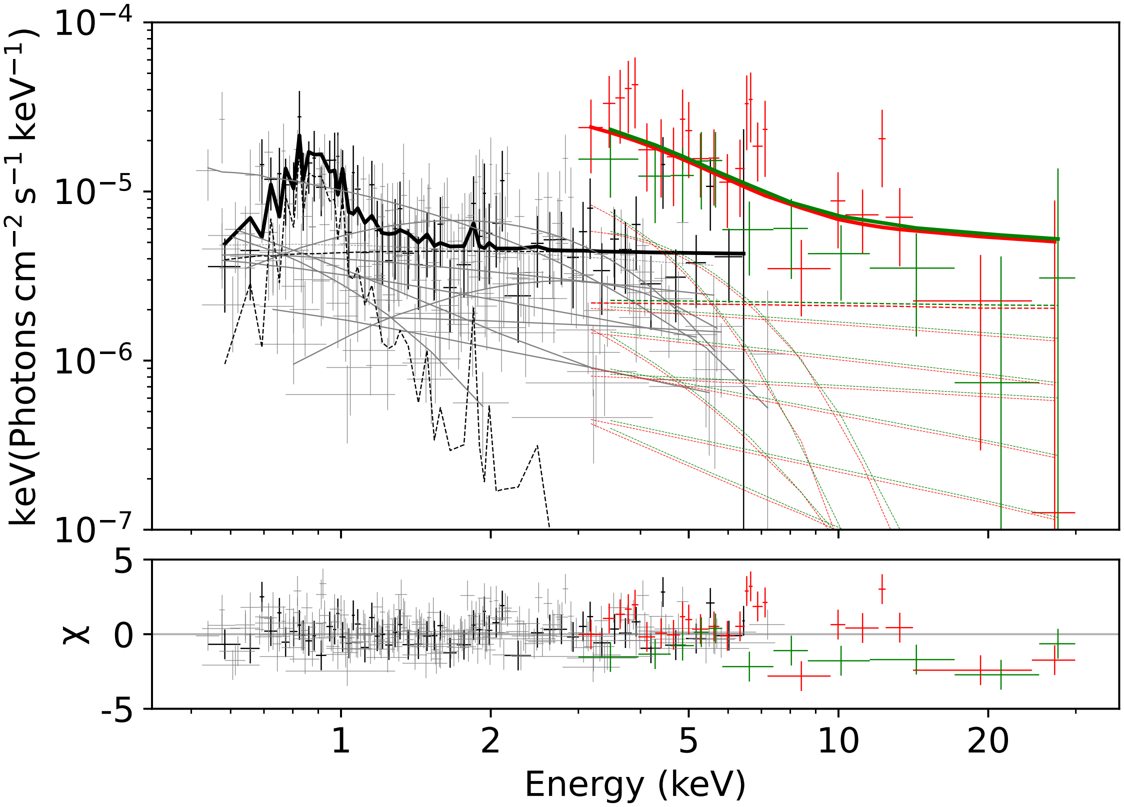

Figure 3.6 Unfolded spectrum and best-fit model for NGC 3627. Black denotes *Chandra* data and model for the AGN core. Red and green denote *NuSTAR* FPMA and FPMB data and models. The *Chandra* data and models for the off-nuclear sources are depicted in light grey.

Table 3.3. Parameters for best-fit NGC 3627 model.

Source	APEC		CUTOFFPL		
	kT (keV)	Norm (10^{-6} cts s^{-1} keV^{-1})	Γ	Cutoff (keV)	Norm (10^{-6} cts s^{-1} keV^{-1})
AGN	$0.83^{+0.12}_{-0.14}$	$1.31^{+0.70}_{-0.43}$	1.04 ± 0.23	–	$2.29^{+1.54}_{-0.57}$
Src 4			$1.31^{+0.22}_{-0.21}$	500^{a}	$2.2^{+2.3}_{-0.4}$
Src 5			-0.97 ± 0.32	1.40^{a}	$5.77^{+2.00}_{-4.68}$
Src 7			$1.61^{+0.51}_{-0.46}$	500^{a}	$0.9^{+4.0}_{-0.2}$
Src 8			$0.9^{+0.65}_{-0.64}$	0.51^{a}	$26.2^{+26.3}_{-17.6}$
Src 9			$1.14^{+0.46}_{-0.41}$	500^{a}	$1.0^{+2.3}_{-0.4}$
Src 10			$1.18^{+0.22}_{-0.20}$	500^{a}	$2.6^{+1.9}_{-0.5}$
Src 12			-0.56 ± 0.23	1.07^{a}	$26.8^{+7.4}_{-20.5}$
Src 14			$1.39^{+0.19}_{-0.18}$	2.76^{a}	$7.7^{+26.2}_{-0.8}$
Src 15			$2.26^{+0.39}_{-0.37}$	500^{a}	$1.84^{+6.89}_{-0.32}$
Src 20			$1.54^{+0.27}_{-0.26}$	500^{a}	$2.7^{+3.4}_{-1.3}$

Note. — The AGN was fit using a POWERLAW model (i.e., not a CUTOFFPL model). The CUTOFFPL normalizations for sources 4, 7, 9, 10, and 20 were estimated with the STEPPAR command. The *Chandra* instrumental normalization constants on each of the sources could not be constrained.

[a] Frozen at this value.

with Seyfert 2 AGN in population studies (e.g. Tran, 2001). The nucleus of NGC 3982 is surrounded by a partial ring of star formation, at a radius of approximately 500 pc (Brum et al., 2017). At MIR wavelengths, NGC 3982 is a compact source with extended emission of unclear origin (Asmus et al., 2014). Tommasin et al. (2010) concluded that 81% of the 19 μm emission originates from the AGN. Esparza-Arredondo et al. (2020) identify NGC 3982 as a candidate fading AGN.

In the X-rays, NGC 3982 was first observed with *ASCA* (Moran et al., 2001) and was later serendipitously observed with *Chandra* as part of the *Chandra* Deep Field North survey (Alexander et al., 2003). The *Chandra* spectrum was first analyzed by Guainazzi et al. (2005b), where the low number of counts hampered attempts to fit the spectrum to a Compton-thick model, though they did report a hydrogen column density $N_{\rm H} > 1.6 \times 10^{24}$ cm^{-2} and a very high Fe K-alpha equivalent width (8 keV based on their “local” fit). These values suggest, though do not confirm, a Compton-thick nature for NGC 3982. Its *Chandra* spectrum was later re-analyzed by Ghosh et al. (2007) in an attempt to determine whether it was a ‘true’ Seyfert 2, but the low number of counts prevented them from making a robust fit to the spectrum. However, because they did find evidence of photoelectric absorption, they concluded the 'true' Seyfert 2 explanation for its 2-10 keV faintness seemed unlikely.

Shu et al. (2007) presented a joint fit of *Chandra* and *XMM-Newton* spectra of NGC 3982, where they measured $N_{\rm H} > 10^{24}\,{\rm cm}^{-2}$ and the Fe K-alpha equivalent width to be 6.31 keV. They therefore classified the AGN as Compton-thick. Akylas & Georgantopoulos (2009) also analyzed these *XMM-Newton* data and measured somewhat less extreme values, finding $N_{\rm H} = 4.32 \times 10^{23}\,{\rm cm}^{-2}$ and an Fe K-alpha equivalent width of 0.8 keV. LaMassa et al. (2011) attempted to update the NGC 3982 Fe K-alpha properties using archival *Chandra* data and a ZGAUSS model, but they were unable to constrain the parameters. LaMassa et al. (2012) fit the 0.5-2 keV spectrum with a single APEC and two powerlaw components with the goal of measuring the relative contributions of star formation (APEC) and the AGN (powerlaw) to the soft X-ray luminosity. The two powerlaws had their spectral indices tied together but separate absorption column densities, representing a partial covering geometry where some of the transmitted X-ray emission is absorbed and the rest is scattered along the line of sight. Adopting a absorption column density of $N_{\rm H} = 4.03 \times\ 10^{23}\,{\rm cm}^{-2}$ for the second powerlaw component, they estimated that 15% of the soft X-ray emission was from the AGN.

Most recently, Kammoun et al. (2020) fit NGC 3982's *XMM-Newton* and *NuSTAR* spectra using a PEXMON model and three variants of a MyTORUS model modified according to the procedures in Yaqoob (2012). The first variant was the standard MyTORUS model, while the other two were decoupled versions where the torus viewing angle was fixed to 90 degrees and the two sides of the torus were modeled separately. One model treated the torus as uniform and the other modeled it as patchy. While the PEXMON model resulted in a Compton-thin column density of $N_{\rm H} = 6 \times 10^{23}\,{\rm cm}^{-2}$, the decoupled MyTORUS models implied significantly higher, Compton-thick values of $N_{\rm H} = 5.3\ \times 10^{24}\,{\rm cm}^{-2}$ for a uniform torus and $N_{\rm H} = 4.5 \times 10^{24}\,{\rm cm}^{-2}$ for a patchy torus.

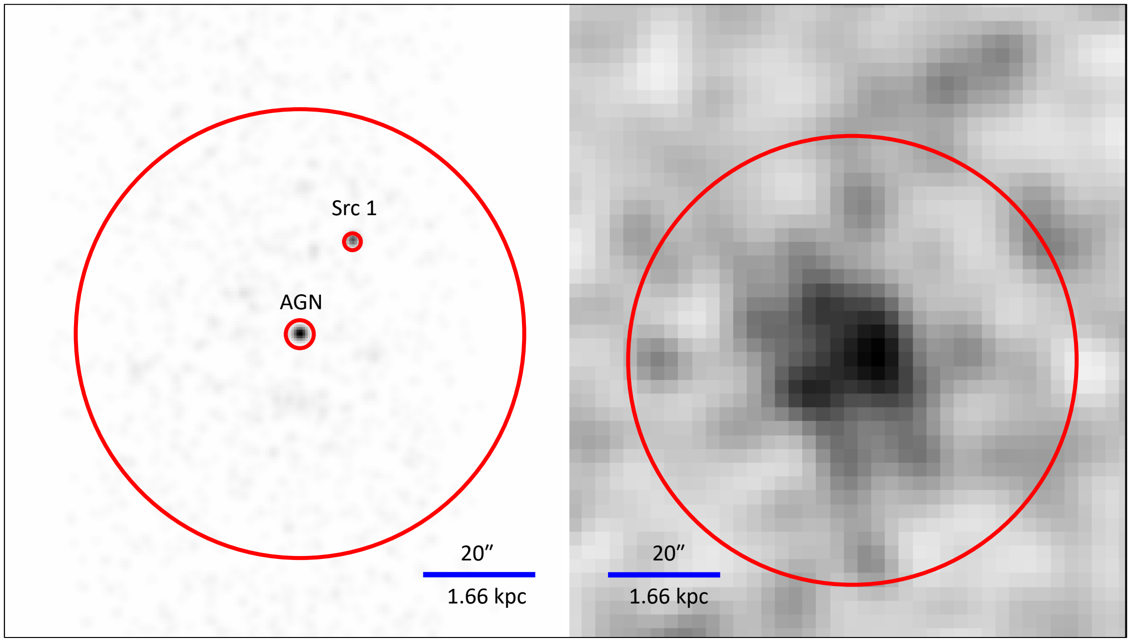

Figure 3.7 *Chandra* and *NuSTAR* FPMA images of NGC 3982. The larger, 40" radius circle denotes the *NuSTAR* extraction region, while the smaller circles denote the *Chandra* extraction regions. An off-nuclear point source (Src 1) is visible in the *Chandra* image, and it was bright enough that it had to be accounted for in the spectral fitting.

3.3.3.1 X-ray Observations & Data Extraction

NGC 3982 was observed once by *Chandra*, on 2004 January 1 (ObsID: 4845), and once by *NuSTAR*, on 2017 December 5 (ObsID: 60375001002). The net exposure times were 9.20 ks and 61.67 ks, respectively. In addition to the AGN, Figure 3.7, which presents these images, shows a bright, off-nuclear *Chandra* point source (Source 1) within the *NuSTAR* beam. For the *Chandra* data, we used a 2.5" radius circular aperture to extract the AGN, and a 1.5" radius circular aperture to extract Source 1. Since the Source 1 net count rate was more than 10% that of the AGN, we included it in the X-ray spectral analysis.

3.3.3.2 X-ray Spectral Fitting

We started by fitting Source 1's *Chandra* spectrum alone with a simple POWERLAW model, finding best-fit values for its POWERLAW spectral index of $\Gamma = 1.17$ and normalization of $5.36 \times 10^{-6}\,\mathrm{cts\,s^{-1}\,keV^{-1}}$. We then fit the AGN and Source 1 jointly, freezing the spectral parameters of Source 1 to the best-fit values from *Chandra*. We started with TBABS*(POWERLAW+POWERLAW) and found C-stat/d.o.f. = 479.68/463. We then added BORUS (C-stat/d.of. = 398.96/459) and APEC (C-stat/d.o.f. = 382.89/457) components to the AGN. $\mathrm{CF_{tor}}$ was unconstrained in this fit, but $\cos(\theta_{\mathrm{inc}})$ was constrained. We froze $\cos(\theta_{\mathrm{inc}})$ to its best-fit value of 0.86 before refitting, which allowed us to place a lower limit on $\mathrm{CF_{tor}}$. The final C-stat/d.o.f. is 396.15/458. The parameters of this final fit are tabulated in Table 3.3.3.2 and the model is plotted over the X-ray data in Figure 3.8. The resulting logarithm of the 2-10 keV luminosity (in units of $\mathrm{erg\,s^{-1}}$) measured from this model is $42.83^{+0.13}_{-0.08}$.

Table 3.4. Parameters for best-fit NGC 3982 model.

Source	APEC		BORUS				POWERLAW	
	kT (keV)	Norm (10^{-5} cts s^{-1} keV^{-1})	$\log(N_{\rm H})$	$\mathrm{CF}_{\rm Tor}$	$\cos(\theta_{\rm inc})$	Norm (cts s^{-1} keV^{-1})	Γ	Norm (10^{-6} cts s^{-1} keV^{-1})
AGN	0.16 ± 0.03	$2.64^{+1.32}_{-1.07}$	≥ 25.3	≥ 0.92	$= 0.86^{\rm a}$	$0.15^{+0.05}_{-0.02}$	$2.48^{+0.06}_{-0.29}$	$9.64^{+12.0}_{-5.72}$
Src 1							$1.18^{\rm a}$	$5.36^{\rm a}$

Note. — The instrumental normalization constant for the *Chandra* AGN data $0.53^{+0.41}_{-0.11}$. The normalization constant for the *Chandra* data of Src 1 was $1.07^{+0.30}_{-0.26}$.

[a] Frozen at this value.

3.3.4 NGC 4501

NGC 4501 (also known as Messier 88) is a spiral galaxy in the Virgo Cluster (Kraan-Korteweg, 1982). In the optical, it has been classified as a Seyfert 2 (e.g., Rush et al., 1993; Véron-Cetty & Véron, 2006) but has occasionally been labeled a LINER (e.g., Carrillo et al., 1999; Brum et al., 2017). The galaxy has a concurrent starburst based on its MIR spectra (Hernán-Caballero & Hatziminaoglou, 2011), though the central regions of the galaxy seem to consist only of evolved stars (Repetto et al., 2017; Brum et al., 2017). The galaxy is approaching the center of the Virgo cluster and has already become depleted of neutral hydrogen due to ram-pressure stripping (e.g., Vollmer et al., 2008; Vollmer, 2009; Nehlig et al., 2016).

NGC 4501 is radio-loud (Videla et al., 2013) and its powerlaw SED across the 1-10 μm range of its *Spitzer* spectrum could include a contribution from synchrotron emission from a jet (Lira et al., 2013). Tommasin et al. (2010) report that 70% of its 19 μm emission comes from the AGN. While these results seem to indicate a strong AGN MIR component, the AGN was barely detectable in subarcsecond MIR images from Asmus et al. (2014), and it was not detected in the *M*-band ($\lambda_c = 4.66\,\mu$m) by the Very Large Telescope (VLT) Infrared Spectrometer and Array Camera (ISAAC; Isbell et al., 2021).

In the X-ray, NGC 4501 was first detected by *ASCA* (Terashima et al., 2000), where its spectrum showed no evidence of heavy absorption or Fe K-alpha emission. Satyapal et al. (2005) analyzed the *Chandra* observation of NGC 4501 and found it contained multiple X-ray components of equal brightness instead of a dominant hard X-ray component. On this basis they classified NGC 4501 as a non-AGN LINER, though they did note a lack of a dominant hard X-ray component could be caused by absorbing column densities of $\geq 10^{24}\,\mathrm{cm}^{-2}$. LaMassa et al. (2012) estimated that approximately 15% of the soft (0.5-2 keV) X-ray emission in NGC 4501 was from the AGN. The *XMM-Newton* observations of NGC 4501 were first analyzed in detail by Cappi et al. (2006), who found its 0.5-10 keV

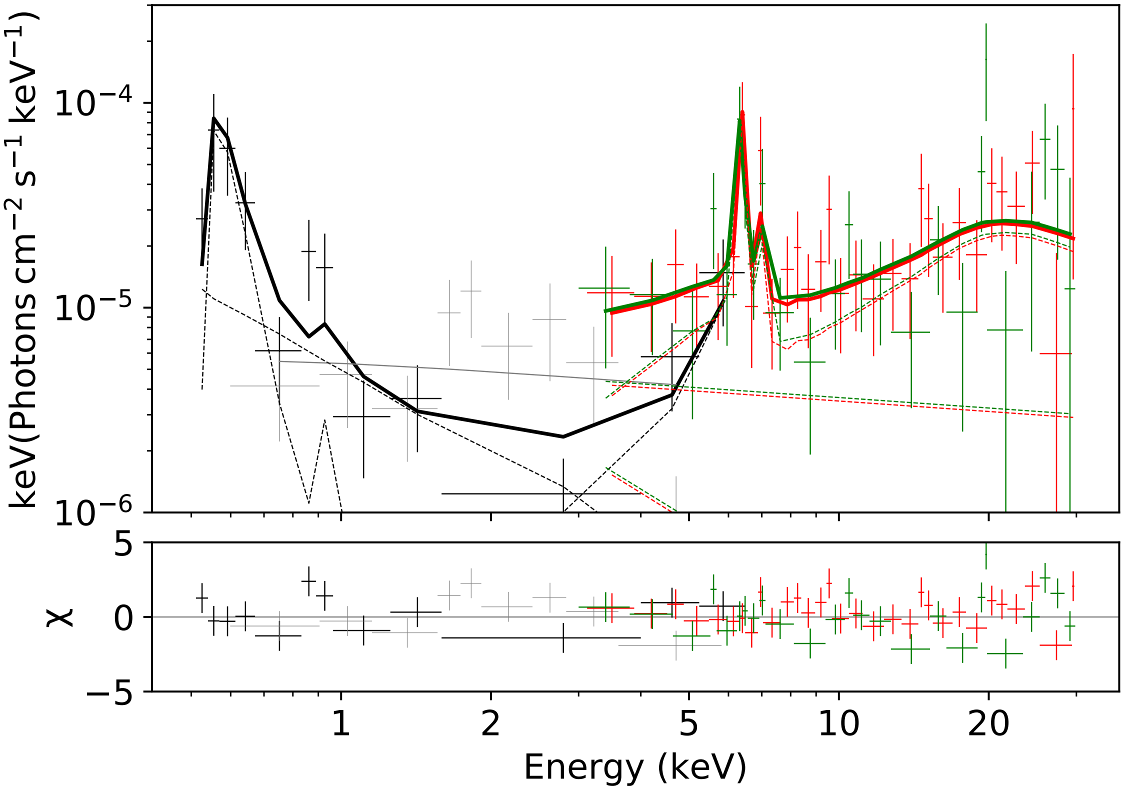

Figure 3.8 Unfolded spectrum and best-fit model for NGC 3982. Black denotes *Chandra* data of the AGN core. Red and green denote FPMA and FPMB data from the *NuSTAR* observation of NGC3982. The *Chandra* data of Src 1 is depicted in light grey.

spectrum could be fit well with a soft thermal component and a powerlaw component. They concurred with Terashima et al. (2000) that there was no evidence of heavy absorption.

In contrast to these researchers' conclusions, Brightman & Nandra (2008) argued that NGC 4501's *Chandra* observation does indeed show a hard X-ray component coincident with the galaxy's optical nucleus. They fit this hard component using a PEXMON model. Using the hard X-ray component to estimate the bolometric luminosity of the AGN, they concluded that the AGN was more likely heavily obscured than intrinsically faint. They also noted that previous studies using *XMM-Newton* data had been hampered by contamination from extranuclear point sources.

3.3.4.1 X-ray Observations and Data Extraction

NGC 4501 was observed twice by *NuSTAR* and once by *Chandra*; details, including observation dates and exposure times, are in Table 3.2.6. The *Chandra* and *NuSTAR* images of NGC 4501 are presented in Figure 3.9, with extraction regions overlaid. The *Chandra* AGN spectrum was extracted with a circular source region 4.78" in radius. In addition to the AGN core, 8 extra-nuclear sources in the *NuSTAR* beam are visible in the *Chandra* image. These were extracted with circular source regions 2" in radius from the *Chandra* data, other than the second and eighth sources which were extracted with circular source regions 1.5" in radius. Of these eight point sources, all but the fifth source (Source 5 in the labeled image) had greater than 10% the count rate of the AGN core, and so they were included in the X-ray spectral fitting.

3.3.4.2 X-ray Spectral Fitting

Because the large number of extra point sources would create too many free parameters for XSPEC to fit, we repeated the procedure we initially attempted in NGC 3627 for the off-nuclear point sources. That is, we fit each off-nuclear source *Chandra* spectrum individually to find the best-fit parameters for its model components. Then, in the joint-fitting step with

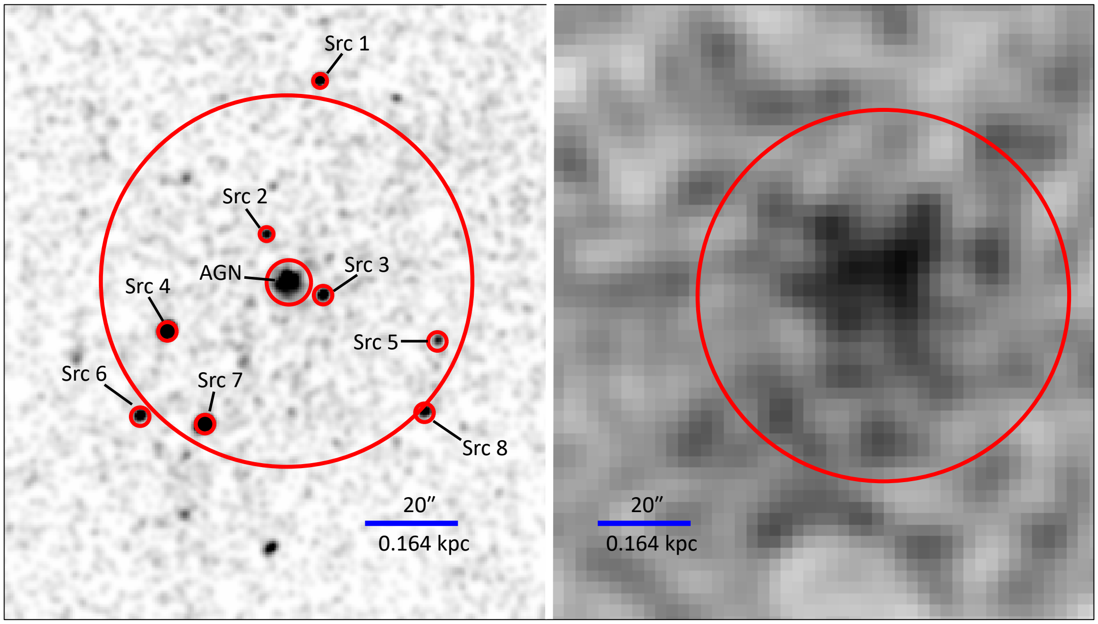

Figure 3.9 *Chandra* and *NuSTAR* FPMA (ObsID: 60375002002) images of NGC 4501. The larger, 40" radius circle denotes the *NuSTAR* extraction region, while the smaller circles denote the *Chandra* extraction regions. Eight off-nuclear point sources are visible in the *Chandra* image; all but Src 5 are sufficiently bright that they are included in the X-ray spectral fitting.

the *NuSTAR* data, model parameters were frozen to their best-fit values from *Chandra*. The only free parameter present for each off-nuclear source in the final fitting was its normalization constant.

In the preliminary *Chandra* fitting, most of the off-nuclear sources were best fit by a simple TBABS*POWERLAW model. The exceptions were Source 1 and Source 4, which both required an additional ZTBABS component, and Source 7, which required an additional APEC component.

We began the joint-fitting with a simple fit consisting of a normalization constant, TBABS, and eight powerlaws, one for the AGN and the rest for the off-nuclear sources. The resulting C-stat/d.o.f. was 1409.95/1489. We then added the other point-source model components and refit each time: the ZTBABS component on Source 4 (C-stat/d.o.f. = 1377.45/1489), the APEC component on Source 7 (C-stat/d.o.f. = 1360.06/1489), and the ZTBABS component on Source 1 (C-stat/d.o.f. = 1345.19/1489).

There is a prominent hard component that rises towards 5 keV in the unfolded *Chandra* spectrum of the AGN (Figure 3.10), as would be expected for an Fe K-alpha line created by an obscuring torus along the line of sight. However this hard component is not seen in the *NuSTAR* data taken 12 years later. This raises two intriguing possibilities. It is possible the AGN has become less luminous in the intervening decade. Modeling all the sources as simple powerlaws, the total *Chandra* 3-8 keV flux within the *NuSTAR* beam was 1.9×10^{-13} erg cm^{-2} s^{-1} with the AGN included, and 1.5×10^{-13} erg cm^{-2} s^{-1} without the AGN. The 3-8 keV flux for the *NuSTAR* observations ranged from 1.4×10^{-13} erg cm^{-2} s^{-1} to 1.6×10^{-13} erg cm^{-2} s^{-1}. As the 3-8 keV *Chandra* flux without the AGN was always closer to the *NuSTAR* fluxes than with it included, this raised the potential for luminosity variation in NGC 4501. It is is also possible that the obscuration of NGC 4501 has changed in the intervening time; if it became very heavily obscured, then even the hard X-ray component could be blocked. Neither possibility is out of the question, as AGN are known to sometimes vary in both luminosity (e.g. LaMassa et al., 2015; Gezari et al., 2017) and obscuration (e.g. Walton et al., 2014; Rivers et al., 2015) over the timescales in question. However, given that 8 point sources other than the AGN are visible in the *NuSTAR* beam it is also possible that the *NuSTAR* spectrum is simply contaminated by them, washing out the AGN's hard X-ray component.

To test the first possibility (that the AGN varied in luminosity) we allowed the normalization of the AGN to freely vary. The AGN spectrum shows a clear soft excess around 1 keV, so we first added an APEC model. We then added a BORUS model to account for the hard component. This rendered kT implausibly large, however, so we set a lower limit of 0.1 keV and an upper limit of 2.0 keV on kT. Because the *NuSTAR* data do not show a reflection/torus component, the inclination angle and covering factor of the AGN torus cannot be measured with much accuracy. For this reason we froze the BORUS $\mathrm{CF}_{\mathrm{Tor}}$ parameter to 0.5, and the BORUS $\cos(\theta_{\mathrm{inc}})$ parameter to 0.17 (corresponding to an inclination angle of 80 deg). The final fit had a C-stat/d.o.f. of 1296.11/1485. The parameters of this fit are tabulated in Table 3.3.4.2. The cross-calibration coefficient of the AGN in this fit was $2.66^{+1.33}_{-0.95}$, which includes 1.71 within its 90% confidence interval. This is not an extreme value for this coefficient to take. As such the claim that the AGN decreased in luminosity cannot be made with confidence. However, this still leaves open the possibility of the obscuration varying between the time of the *Chandra* observation and the time of the *NuSTAR* observations.

To test this second possibility (that the AGN varied in obscuration), we untied the *Chandra* and *NuSTAR* values of the BORUS parameter N_{H} from each other, but did not allow the AGN to vary in luminosity between the *Chandra* and *NuSTAR* data. After refitting with these changes, the C-stat/d.o.f. was 1296.11/1485. The value of $\log(N_{\mathrm{H}}/\mathrm{cm}^{-2})$ in this model changed from $22.91^{+0.28}_{-0.21}$ in the *Chandra* observation to $22.43^{+0.28}_{-0.24}$ in the *NuSTAR* observations, too similar to explain the lack of appearance of a hard component in the *NuSTAR* data. Considering this and the negligible improvement in C-stat/d.o.f. if we let the obscuration vary instead of the luminosity, we conclude that there is no evidence in our data of NGC 4501 obscuration variability.

Given that we have no strong evidence of either luminosity or obscuration variability in this AGN, the most parsimonious explanation for the lack of a hard component in the *NuSTAR* data is contamination from the eight extra point sources. It should be noted, however, that the possibility of variability cannot be ruled out with this data. The best fit with the cross normalization constant on the AGN left to freely vary is plotted in Figure 3.10. The logarithm of the resulting 2-10 keV luminosity (in units of $\mathrm{erg\,s^{-1}}$) measured from the model is $41.50^{+0.25}_{-0.11}$.

Table 3.5. Parameters for best-fit NGC4501 model.

Source	ZTBABS	APEC		BORUS				POWERLAW	
	$N_{\rm H}$ (10^{22} cm^{-2})	kT (keV)	Norm	$\log(N_{\rm H})$	CF$_{\rm Tor}$	$\cos(\theta_{\rm inc})$	Norm	Γ	Norm
AGN		0.75 ± 0.11	$2.65^{+2.56}_{-1.48}$	$22.87^{+0.25}_{-0.15}$	$0.5^{\rm a}$	$0.17^{\rm a}$	$2.03^{+1.60}_{-0.44}$	≥ 1.98	$3.24^{+3.30}_{-1.83}$
Src 1	$0.72^{\rm a}$							$2.25^{\rm a}$	$15.2^{\rm a}$
Src 2								$1.21^{\rm a}$	$1.59^{\rm a}$
Src 3								$1.48^{\rm a}$	$3.05^{\rm a}$
Src 4	$0.21^{\rm a}$							$2.12^{\rm a}$	$31.4^{\rm a}$
Src 6								$1.37^{\rm a}$	$4.17^{\rm a}$
Src 7		$1.09^{\rm a}$	$7.25^{\rm a}$					$2.33^{\rm a}$	$11.7^{\rm a}$
Src 8								$1.30^{\rm a}$	$2.68^{\rm a}$

Note. — The instrumental normalization constants for the *Chandra* data, in the order of sources from the table, are $2.66^{+1.33}_{-0.95}$, $1.03^{+0.27}_{-0.23}$, $1.07^{+0.43}_{-0.34}$, $1.01^{+0.31}_{-0.26}$, $1.00^{+0.12}_{-0.11}$, $0.78^{+0.23}_{-0.19}$, $1.00^{+0.13}_{-0.12}$, and $1.01^{+0.32}_{-0.27}$. The *NuSTAR* normalization constants for ObsID 60375002004A are $0.88^{+0.15}_{-0.14}$ for FPMA and $0.98^{+0.18}_{-0.16}$ for FPMB. The normalizations for the model components are in units of 10^{-6} cts s^{-1} keV^{-1} for APEC, 10^{-3}cts s^{-1} keV^{-1} for BORUS, and 10^{-6} cts s^{-1} keV^{-1} for POWERLAW.

[a] Frozen at this value.

3.3.5 IC 3639

IC 3639 is a barred spiral galaxy containing a Seyfert 2 nucleus, as well as a nuclear starburst within the central 80 pc of the galaxy (González Delgado et al., 1998; Fernández-Ontiveros et al., 2018). It is part of a compact group of galaxies, though it lacks features indicative of recent mergers or interactions (Barnes & Webster, 2001). IC 3639 has polarized broad Hα emission, though the nature of that emission is uncertain: some researchers considerate it as indicative of a hidden broad-line region (Heisler et al., 1997; Lumsden et al., 2001; Temporin et al., 2003), while others claim it is a kinematic feature of the narrow-line region (Ghosh et al., 2007). MIR interferometry reveals a compact, sub-arcsecond, unresolved nuclear point source (Asmus et al., 2014, 2016) surrounded by a halo of MIR emission associated with the compact nuclear starburst (Fernández-Ontiveros et al., 2018). The starburst contributes 70% of the observed MIR flux.

The first published X-ray observations of IC 3639 suggested that it possessed a very high hydrogen column density and a strong Fe Kα line (Risaliti et al., 1999b). A more detailed analysis of *Chandra*, *Suzaku*, and *NuSTAR* data by Boorman et al. (2016) confirmed it has a hydrogen column density of $10^{25}\,\mathrm{cm}^{-2}$ and an extreme Fe Kα equivalent width of 2.29 keV. They also found it has a 2-10 keV luminosity well below the expected value based on the luminosity of its [O III] line, assuming the relations of Panessa et al. (2006) and Berney et al. (2015). Overall, Boorman et al. (2016) conclude that IC 3639 is a Compton-thick AGN possessing an active central engine generating a strong reflection component in its X-ray spectrum.

3.3.5.1 X-Ray Observations & Data Extraction

IC 3639 was observed once by both *NuSTAR* and *Chandra*. The observation dates and exposure times are in Table 3.2.6 and Figure 3.11 presents the images. The higher resolution *Chandra* data reveal a faint, off-nuclear point source (labeled “Src 1” in Figure 3.11) as well

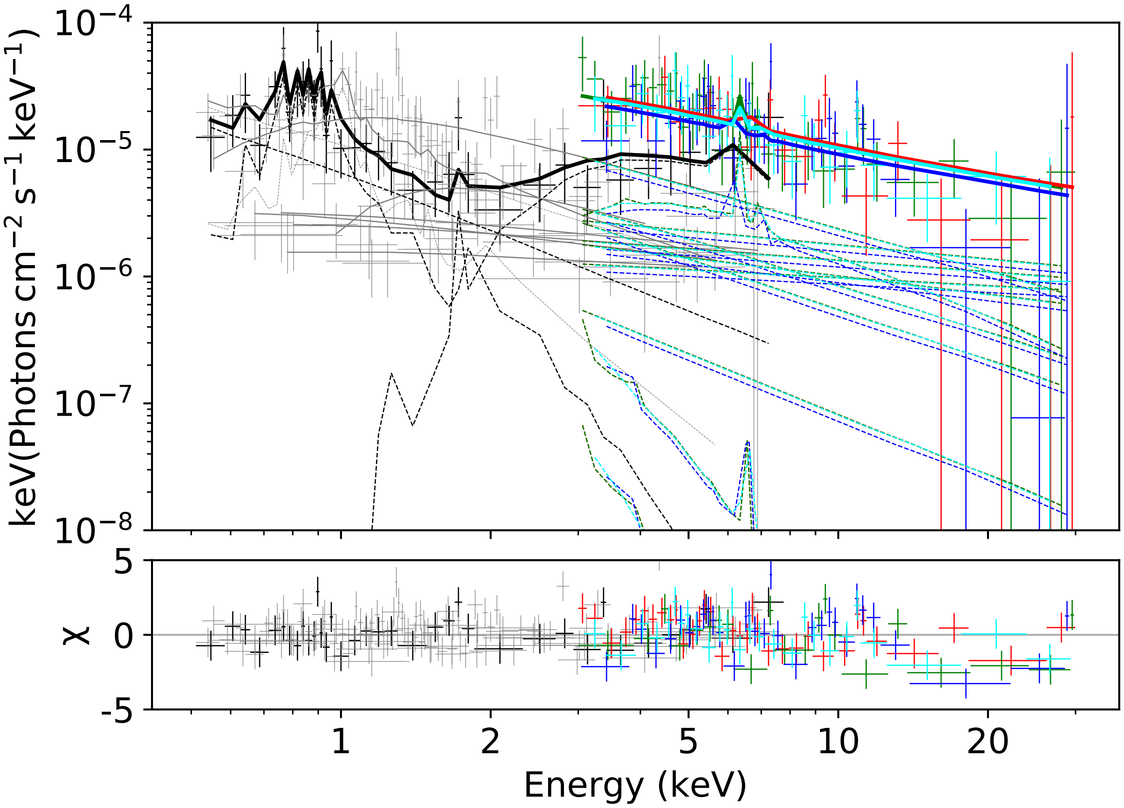

Figure 3.10 Unfolded spectrum and best-fit model for NGC 4501. Black denotes *Chandra* data and model for the AGN core. Red and green denote FPMA and FPMB data and models for *NuSTAR* observation 60375002002, while blue and cyan denote FPMA and FPMB data and models for *NuSTAR* observation 60375002004. The *Chandra* data and models for the extra point sources are depicted in light grey.

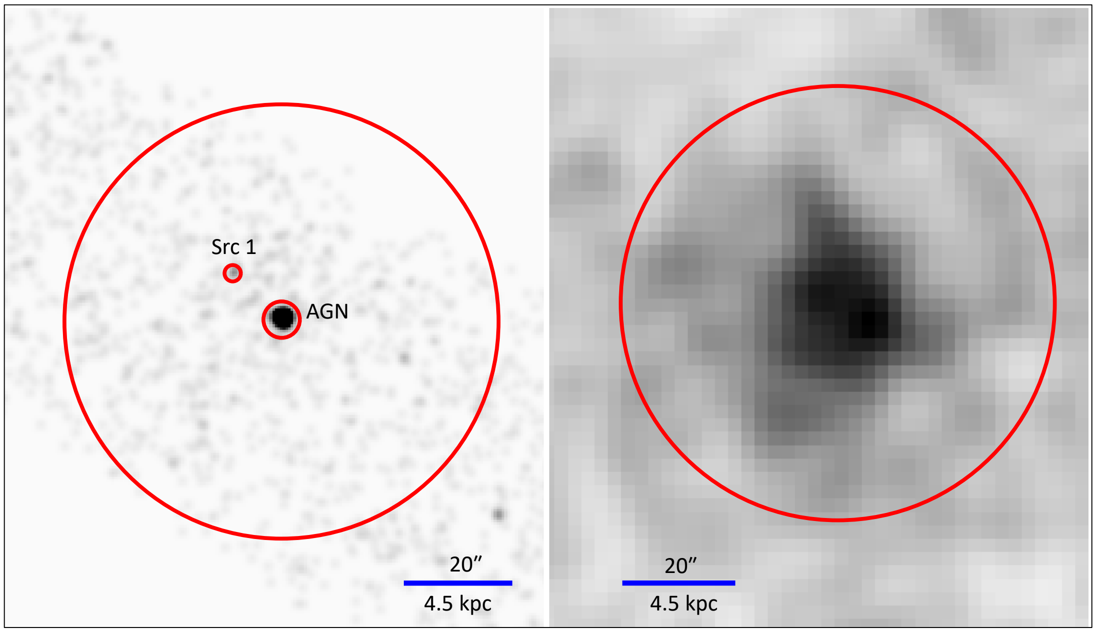

Figure 3.11 *Chandra* and *NuSTAR* FPMA images of IC 3639. The larger, 40” radius circle denotes the *NuSTAR* extraction region, while the smaller circles denote the *Chandra* extraction regions. An off-nuclear point source (Src 1) is visible in the *Chandra* image, but is sufficiently faint to be ignored in the X-ray spectral fitting.

as the AGN in the 40” radius *NuSTAR* beam. The *Chandra* AGN spectrum was extracted with a circular region of 3.35 radius, while Source 1 was extracted with a 1.5” radius region. Since Source 1 has $\leq$10% the net count rate of the AGN, its spectrum is not used in the spectral fitting.

3.3.5.2 X-Ray Spectral Fitting

We first fit the *Chandra* and *NuSTAR* data jointly with a simple absorbed powerlaw (TBABS*POWERLAW model. The resulting C-stat/d.o.f. was 1062.90/830, indicating a poor fit.

Looking at the unfolded spectrum for IC 3639 (Figure 3.12), an extremely strong Fe Kα line can be seen around 6.4 keV. The unfolded spectrum also shows a substantial rise from 10-20 keV, with a pronounced Compton hump at 20 keV. We therefore added a BORUS component to the initial TBABS*POWERLAW model.

Prominent residuals remained at 0.5-2.0 keV, so we also added an APEC component. The resulting best fit model has C-stat/d.o.f. = 606.54/824. The parameter values for the best fit model are tabulated in Table 3.3.5.2. Since the upper error bar for $\mathrm{CF_{tor}}$, the lower error bar for $\cos(\theta_{\mathrm{inc}})$, and the lower error bar for the BORUS normalization were less than 0.005 in value, we have rounded them up to 0.01. The best fit model is plotted over the unfolded spectrum in Figure 3.12. The logarithm of the 2-10 keV luminosity (in units of $\mathrm{erg\,s^{-1}}$) measured from the model is $43.07^{+0.18}_{-0.12}$.

Table 3.6. Parameters for best-fit IC 3639 model.

APEC		BORUS				Powerlaw	
kT (keV)	Norm (10^{-5} cts s^{-1} keV^{-1})	$\log(N_{\rm H})$	CF$_{\rm Tor}$	$\cos(\theta_{\rm inc})$	Norm (cts s^{-1} keV^{-1})	Γ	Norm (10^{-5} cts s^{-1} keV^{-1})
$0.85^{+0.12}_{-0.12}$	$3.06^{+0.69}_{-0.64}$	$25.00^{+0.06}_{-0.26}$	$0.87^{+0.01}_{-0.12}$	$0.77^{+0.07}_{-0.01}$	$0.04^{+0.02}_{-0.01}$	≥ 2.4	$5.01^{+2.59}_{-0.81}$

Note. — Error bars shown are for 90% confidence intervals. The *Chandra* instrumental normalization constant value was $0.59^{+0.24}_{-0.06}$.

3.3.6 NGC 4922

NGC 4922 is a pair of galaxies in the late stages of a merger (Ricci et al., 2017b). The northern galaxy has been classified as a luminous infrared galaxy (Díaz-Santos et al., 2010) and a Seyfert 2 (Yuan et al., 2010). It is also a water megamaser (Braatz et al., 2004). The southern galaxy is an elliptical galaxy with no obvious signs of activity (Alonso-Herrero et al., 1999).

In the X-rays, NGC 4922 was first studied in detail with *ROSAT*, which detected extended soft X-ray emission across the entire merging pair (Alonso-Herrero et al., 1999). Further observations by Ricci et al. (2017b) revealed the northern galaxy is brighter in X-rays, with the southern galaxy's nucleus only detectable in the 0.3-2 keV band by *Chandra*, and it was not detected by*NuSTAR*. Based on joint analysis of *Chandra* and *NuSTAR* observations, Ricci et al. (2017b) reported the northern galaxy to be Compton-thick, with $N_{\rm H} > 4.27 \times 10^{24}\,{\rm cm}^{-2}$.

3.3.6.1 X-Ray Observations and Data Extraction

NGC 4922 was observed once by *NuSTAR* and three times by *Chandra*; the observation dates and exposure times are in Table 3.2.6. The *Chandra* spectra were extracted using circular source regions 3.7" in radius. Figure 3.13 shows the second *Chandra* observation and the *NuSTAR* FPMA observation with the extraction regions overlaid.

3.3.6.2 X-Ray Spectral Fitting

We first fit the *Chandra* and *NuSTAR* data jointly with a simple TBABS*POWERLAW fit, using a Galactic hydrogen column density of $N_{\rm H}^{\rm Gal}= 1.06 \times 10^{20}\,{\rm cm}^{-2}$. The resulting C-stat/d.o.f. was 407.61/423.

The unfolded spectrum (Figure 3.14) shows a less prominent Compton rise than some of the other galaxies in the sample (e.g., NGC 1386), but it is present. A presumed Fe Kα

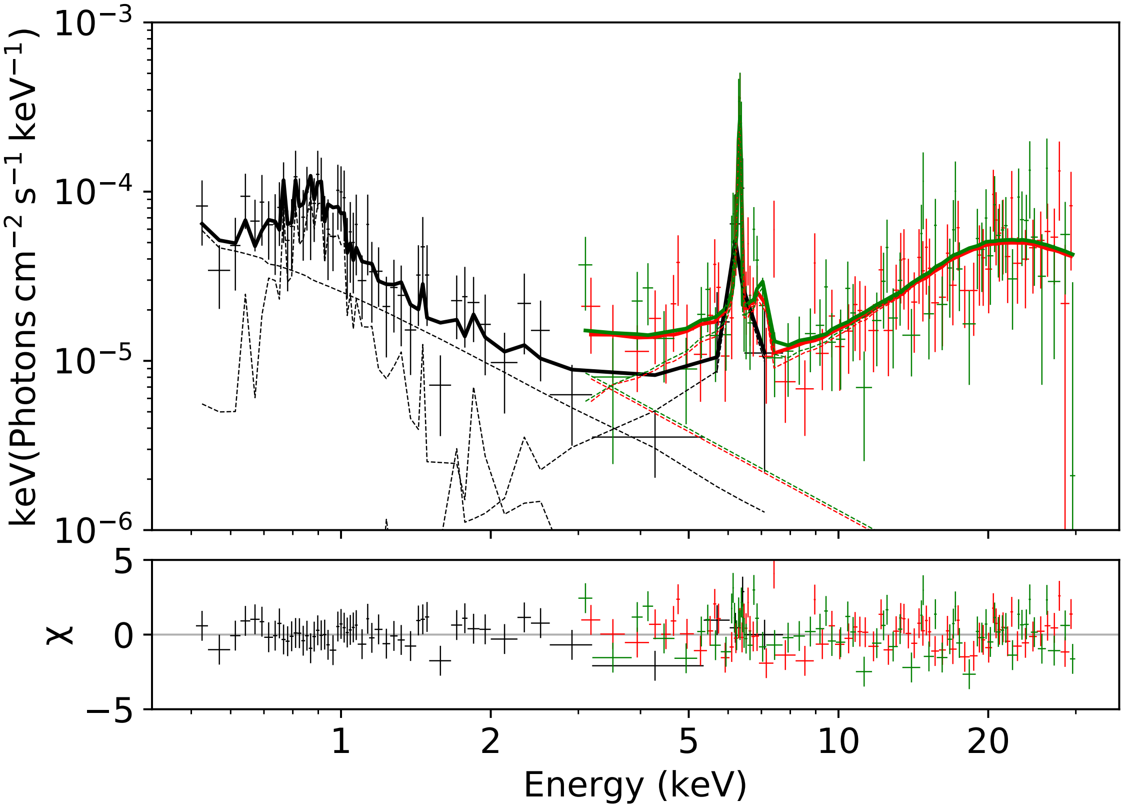

Figure 3.12 Unfolded spectrum and best-fit model for IC 3639. Black denotes *Chandra* data, green denotes *NuSTAR* FPMA data, and red denotes *NuSTAR* FPMB data.

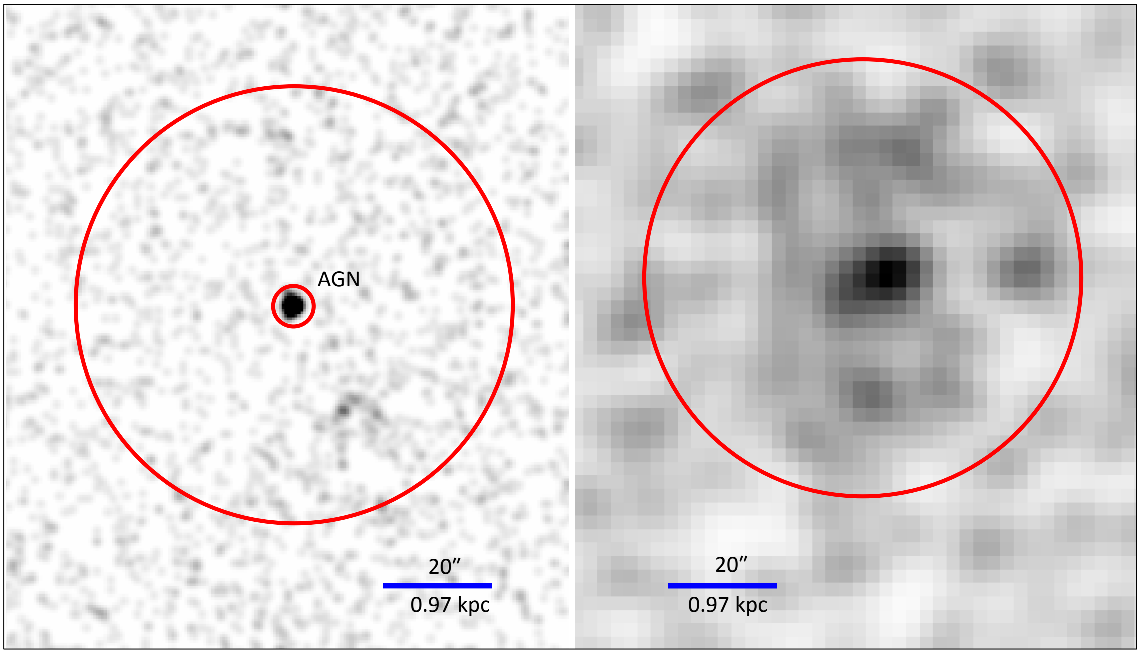

Figure 3.13 *Chandra* (ObsID: 15065) and *NuSTAR* FPMA images of NGC 4922. The larger, 40" radius circle denotes the *NuSTAR* extraction region, while the smaller circle denotes the *Chandra* extraction region.

line is also present at 6.4 keV. While the signal-to-noise is lower than in the aforementioned galaxies, NGC 4922 nonetheless shows the features typical of Compton-thick AGN. We therefore added a BORUS component to the initial TBABS*POWERLAW fit, fixing the BORUS spectral index to the POWERLAW spectral index. This resulted in a C-stat/d.o.f. of 338.44/414. An excess of soft X-ray emission was present from 0.5-2.0 keV, so an APEC component was added, resulting in C-stat/d.o.f. = 324.51/412. Because $\cos(\theta_{\mathrm{inc}})$ was completely unconstrained with these model components, its value was frozen at 0.17 (or $\theta_{\mathrm{inc}} \approx 80°$), representing a near edge-on line of sight. We then refit the model. The final C-stat/d.o.f. was 321.07/412. The resulting values for each of the model parameters are shown in Table 3.3.6.2. The model is plotted over the *Chandra* and *NuSTAR* data as the solid lines in Figure 3.14. The logarithm of the 2-10 keV luminosity (in units of erg s^{-1}) measured from the model is $42.29^{+0.12}_{-0.47}$.

Table 3.7. Parameters for best-fit NGC 4922 model.

APEC		BORUS				POWERLAW	
kT (keV)	Norm (10^{-6} cts s^{-1} keV^{-1})	$\log(N_{\rm H})$	CF$_{\rm Tor}$	$\cos(\theta_{\rm inc})$	Norm (10^{-4} cts s^{-1} keV^{-1})	Γ	Norm (10^{-6} cts s^{-1} keV^{-1})
$1.06^{+0.34}_{-0.21}$	$4.71^{+6.02}_{-2.71}$	$23.89^{+0.11}_{-0.17}$	≥ 0.25	$= 0.17$[a]	$3.96^{+1.02}_{-2.50}$	1.75 ± 0.34	$9.04^{+6.72}_{-3.67}$

Note. — The *Chandra* instrumntal normalization constant values were $1.35^{+0.75}_{-0.52}$ (ObsID: 4775), $1.17^{+0.56}_{-0.41}$ (ObsID: 15065), and $1.69^{+0.87}_{-0.62}$ (ObsID: 18201).

[a] Frozen at this value.

3.3.7 NGC 5005

NGC 5005 is a weakly barred spiral galaxy with a nucleus that is heavily shrouded in dust (Pogge et al., 2000). Its AGN is known to be variable over timescales of months (Younes et al., 2012). NGC 5005's optical classification has been ambiguous. Shuder & Osterbrock (1981) were able to identify Hα, [S II], [O II], and [O III] emission lines in its nuclear spectrum, but no others. They did not specify a classification for it but regarded it as unlikely to be a Seyfert 2. Later papers in the literature have classified it as a LINER (e.g., Huchra & Burg, 1992; Ho et al., 1997; Véron-Cetty & Véron, 2006), a Seyfert 2 (e.g., Audibert et al., 2017), or both a LINER and a Seyfert 2 at the same time (e.g., Spinelli et al., 2006; Malkan et al., 2017). Palomar spectra for NGC 5005 show a broad Hα component blended with narrow Hα and [N II] emission (Rush et al., 1996; Ho et al., 1997), suggesting NGC 5005 is an unobscured AGN. However, Balmaverde & Capetti (2014) were unable to find a broad Hα component in later *Hubble* spectroscopy when using the [O I] line as a template for deblending, and therefore concluded that either the broad Hα detection in the Palomar data was spurious, or NGC 5005 is a changing-look AGN. Constantin et al. (2015) did, in contrast, identify a broad Hα line in the *Hubble* spectra when using the [S II] line as a template for deblending, measuring a broad Hα component with FWHM of $2610\,\mathrm{km\,s^{-1}}$. A detailed analysis of new ground-based spectra as well as the archival *Hubble* spectra for NGC 5005 was published by Cazzoli et al. (2018), who found a broad H-alpha component in the *Hubble* spectra, blended with [S II] and [N II]. The broad Hα component had a FWHM of $2152\,\mathrm{km\,s^{-1}}$, was very weak, and was not visible in their ground-based spectra.

NGC 5005's core is embedded in extended MIR emission that appears to trace out its spiral structure (Asmus et al., 2014). Based on *Spitzer* data, Tommasin et al. (2010) estimated that only 44% of its 19μm emission is from an AGN. Based on the NIR [Fe II] and [P II] forbidden line flux ratios, Terao et al. (2016) found that, unusually, NGC 5005's narrow line region seems to be predominantly shock-ionized rather than UV-ionized.

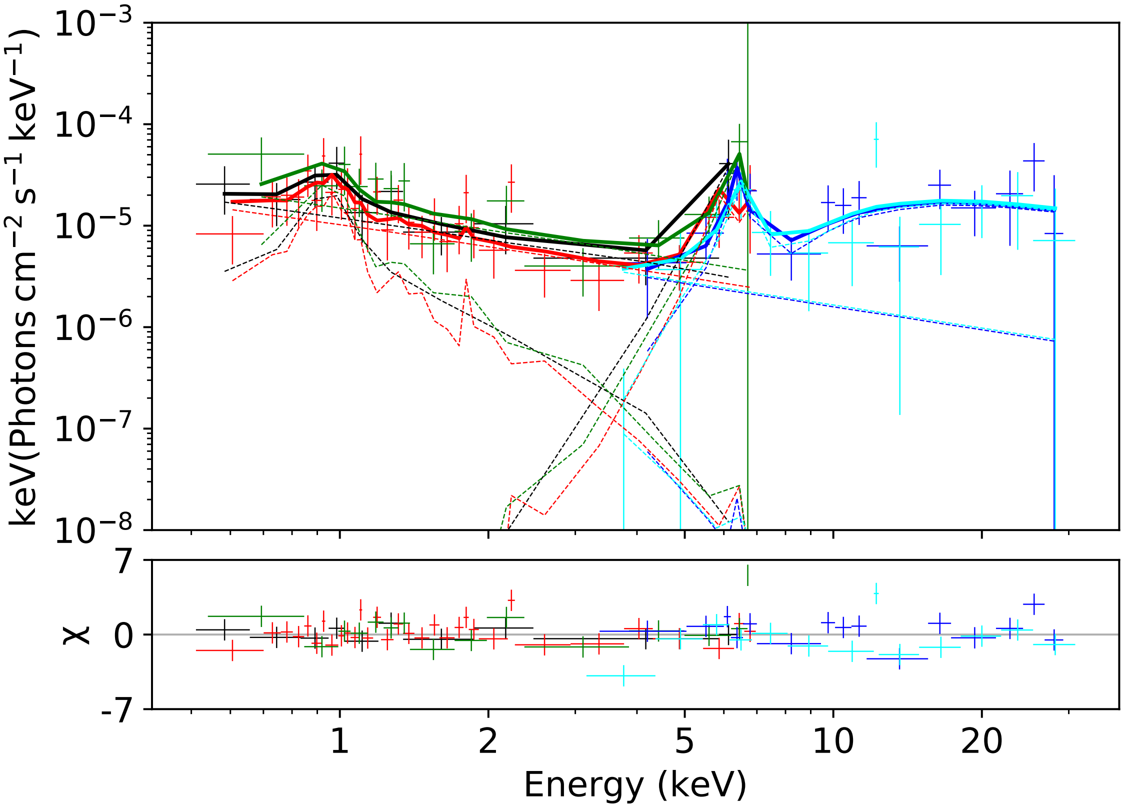

Figure 3.14 Unfolded spectrum and best-fit model for NGC 4922. Black, red and green denote *Chandra* data (ObsIDs 4775, 15065, 18201), while blue and cyan denote FPMA and FPMB data.

In the X-rays, NGC 5005 was first detected by *ASCA*, where its spectrum was analyzed by Risaliti et al. (1999a). They reported a hydrogen column density of $N_{\rm H} > 10^{24}\,{\rm cm}^{-2}$, implying a Compton-thick AGN. Further evidence of NGC 5005's Compton-thick nature comes from the unusually low ratio between its observed 2-10 keV X-ray and [O III] luminosities. Risaliti et al. (1999a) note, however, that NGC 5005 showed no evidence of a reflection component in its *ASCA* spectrum, with an upper limit of 0.9 keV on the equivalent width of the Fe Kα line. They concluded that the hydrogen column density was so thick that the soft X-ray emission from the AGN was completely absorbed, leaving only extended emission from a concurrent starburst to create the *ASCA* spectrum.

Observations by *Chandra* and *XMM-Newton* revealed new features of NGC 5005's X-ray emission. The AGN core was found to be embedded in a background of extended X-ray emission that follows the contours of the galaxy (Guainazzi et al., 2005a), and that might be responsible for a large soft excess observed in its 0.6-1 keV X-ray spectrum (Gallo et al., 2006). Guainazzi et al. (2005a) concluded the X-ray spectrum was unlikely to be dominated by an inverse Compton component, and placed an upper limit on the equivalent width of an Fe Kα line of ≤ 0.24 keV. In contrast to Risaliti et al. (1999a), they measured $N_{\rm H} \simeq 1.5 \times 10^{20}\,{\rm cm}^{-2}$. Furthermore, their search of the available literature at the time (e.g., Shuder & Osterbrock, 1981; Dahari & De Robertis, 1988; Ho et al., 1997) revealed a wide range of reported [O III] fluxes for NGC 5005, some of which were not overluminous compared to the X-ray flux. They therefore claimed NGC 5005 was misidentified as a Compton-thick AGN. These conclusions were further reinforced by later analyses of the *Chandra* and *XMM-Newton* observations, with values of $N_{\rm H}$ closer to $10^{20}\,{\rm cm}^{-2}$ (Brightman & Nandra, 2011b) or $10^{21}\,{\rm cm}^{-2}$ (Younes et al., 2012) than to Compton-thick column densities. In summary, the latest analyses of optical and X-ray observations of NGC 5005 suggest that it might be intrinsically underluminous rather than heavily obscured.

3.3.7.1 X-ray Observations and Data Extraction

NGC 5005 has been observed once each by *NuSTAR*, *Chandra*, and *XMM-Newton*; details of the observations, including the observation dates and exposure times are in Table 3.2.6. *Chandra* and *NuSTAR* images of the galaxy are presented in Figure 3.15. The *Chandra* AGN spectrum was extracted from a 5.5” radius circular source region. Two extranuclear *Chandra* point sources (labeled “Src 1” and “Src 2”) are visible within the *NuSTAR* beam, which we extracted with 1.5” radius circular source regions. Since their count rates were less than 10% the count rate of the AGN, they were ignored in the X-ray spectral fitting.

Since no background flares were evident in the *XMM-Newton* 10-12 keV lightcurve of NGC 5005, the EPIC pn spectrum was extracted from the full dataset. We used 30” circular source regions with 60” radius background regions. For the MOS data, we filtered out times with high background, defined as times when the 10-12 keV count rate was $> 0.35\,\mathrm{ct\,s^{-1}}$. Using patterns 0-12, we extracted the MOS source spectra with 30” radius circular regions and 50” $-$ 80” annular background regions.

3.3.7.2 X-ray Spectral Fitting

We initially began our analysis with the *Chandra* and *NuSTAR* data only. We started with a simple TBABS*POWERLAW fit, with the Galactic hydrogen column density set to $N_{\mathrm{H}}^{\mathrm{Gal}} = 1.17 \times 10^{20}\,\mathrm{cm^{-2}}$. The C-stat/d.o.f. for this fit was 550.23/584, indicating that a powerlaw model captures most of this AGN’s spectrum. Next we added an APEC component to account for the soft excess visible from 0.5-2.0 keV. This reduced C-stat/d.o.f. to 515.15/582, so the APEC component was kept. We then added a BORUS component, as would be appropriate for a Compton-thick AGN, which brought C-stat/d.o.f. down to 504.28/578. However, looking at the unfolded spectrum of NGC 5005 (Figure 3.16), it is unclear whether a BORUS component is truly justified. The hard X-ray emission does not possess the Compton hump characteristic of a reflection-dominated spectrum, but instead

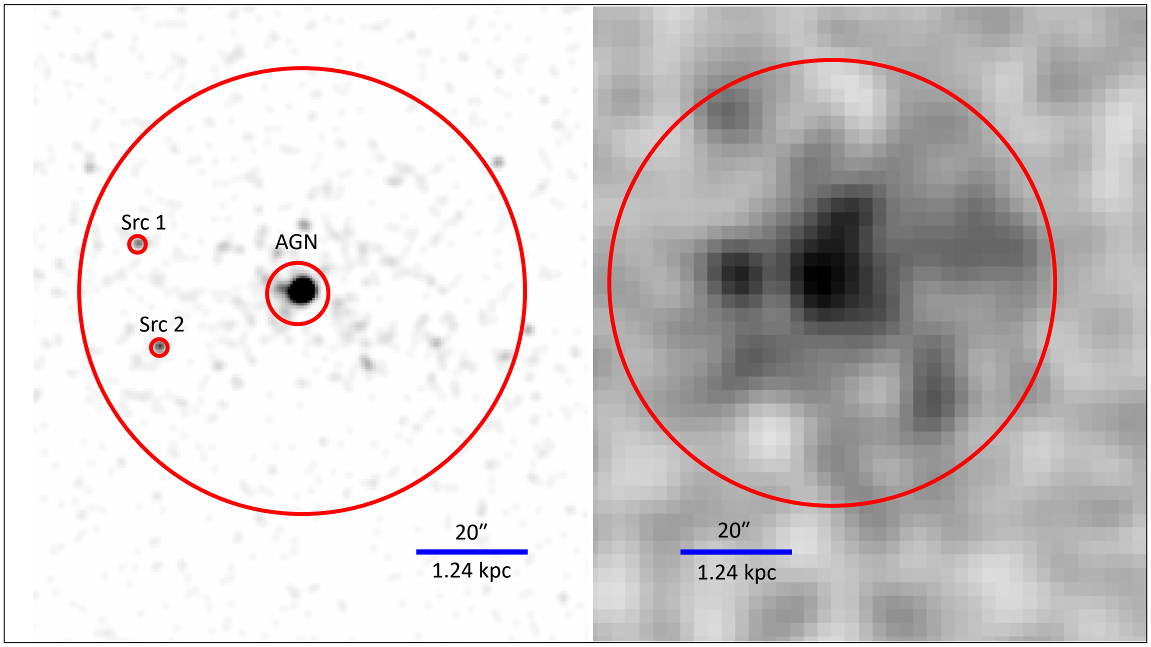

Figure 3.15 *Chandra* and *NuSTAR* FPMA images of NGC 5005. The larger, 40" radius circle denotes the *NuSTAR* extraction region, while the smaller circles denote the *Chandra* extraction regions. Two off-nuclear point sources (Src 1 and Src 2) are visible in the *Chandra* image, but were faint enough to be ignored in the spectral fitting.

appears to be flat or even declining. It may possess a broad line component in the *NuSTAR* spectrum, visible as a bump of emission from 4-8 keV. Together, these facts suggest the AGN spectrum might be better fit with just a ZGAUSS component rather than an entire BORUS component.

We added a ZGAUSS component to the TBABS*(APEC+POWERLAW) model, fixing the line energy at 6.4 keV and fixing the line width at 10^{-3} keV. This did not significantly change C-stat/d.o.f., though freeing the line width to vary in the fitting brought C-stat/d.o.f. down to 497.25/580.

To further ascertain the nature of the unusual bump at 4-8 keV we extracted the *XMM-Newton* observation of NGC 5005. The bump from 4-8 keV seen in the *NuSTAR* spectrum is not clearly seen in its *XMM-Newton* spectra; however the *XMM-Newton* data were taken a decade earlier, so the lack of the line may simply be due to variability. To determine whether the line was truly absent from the *XMM-Newton* and *Chandra* data, we first fit the *NuSTAR* data alone to a TBABS*(ZGAUSS+POWERLAW) model to find the best fit parameters for the line. The C-stat/d.o.f. of this fit was 391.98/468; for comparison, the C-stat/d.o.f. for a TBABS*(BORUS+POWERLAW) fit to the *NuSTAR* data was 394.76/467. The resulting line parameters were an energy of 5.91 keV, a line with of 0.76 keV, and a normalization of 5.26×10^{-6} $\mathrm{cts\,s^{-1}\,keV^{-1}}$. We then fit the *XMM-Newton* and *Chandra* data alone with a TBABS*(APEC+ZGAUSS+POWERLAW) model, with the ZGAUSS energy and width set to the values measured from the *NuSTAR* data alone. The normalizations were left to vary freely. The resulting normalizations were consistent with the *NuSTAR* data for both the *XMM-Newton* and *Chandra* data.

We ran 10,000 Monte Carlo simulations to estimate the false alarm probability for the putative line. We simulated fake *NuSTAR* observations in XSPEC with the parameters of the best fit to the *NuSTAR* data using only a POWERLAW component, then tried fitting the data with both a POWERLAW model and a POWERLAW+ZGAUSS model. The normalization of the ZGAUSS component was left to freely vary, while the line width was fixed at the value measured from *NuSTAR*. We then stepped through the values in line energy and saved the best fit. The resulting decrease in C-stat was greater than the decrease for the real data only in 4 out of 10,000 runs. The same was true if we instead fit it with a POWERLAW+ZGAUSS model where the line was unresolved (width fixed at 3×10^{-3} keV). We therefore estimate the false positivity rate as 0.04%. This is a >3.3 sigma detection, and we treat the line as real.

For the final fit, we froze the ZGAUSS parameters to the best-fit values from the *NuSTAR* data alone. The resulting C-stat/d.o.f. was 1872.72/2130. The parameters for this model are listed in Table 3.3.7.2. It is plotted over the *XMM-Newton*, *Chandra* and *NuSTAR* data in Figure 3.16. The logarithm of the 2-10 keV luminosity (in units of $\mathrm{erg\,s^{-1}}$) measured from the model is $42.29^{+0.12}_{-0.47}$.

Table 3.8. Parameters for best-fit NGC 5005 model.

APEC		ZGAUSS			POWERLAW	
kT (keV)	Norm (10^{-5} cts s^{-1} keV^{-1})	Line Energy (keV)	σ (keV)	Norm (10^{-6} cts s^{-1} keV^{-1})	Γ	Norm (10^{-5} cts s^{-1} keV^{-1})
0.79 ± 0.03	$4.62^{+0.67}_{-0.59}$	$5.91^{+0.60}_{-0.62}$[a]	$0.74^{+0.47}_{-0.48}$[a]	$5.26^{+4.39}_{-3.08}$[a]	1.69 ± 0.05	$6.61^{+0.88}_{-0.79}$

Note. — The *XMM-Newton* pn, MOS1, and MOS2 instrumental normalization constant values were $1.14^{+0.14}_{-0.13}$, $1.14^{+0.15}_{-0.13}$, and $1.17^{+0.15}_{-0.13}$ (ObsID: 0110930501). The *Chandra* normalization constant value was $0.59^{+0.10}_{-0.08}$ (ObsID: 4021). All parameters for APEC and POWERLAW components were measured using a fit with the ZGAUSS components fixed to the values from the *NuSTAR* data alone.

[a] Measured from fit to *NuSTAR* data alone

3.3.8 Mrk 463

Mrk 463 is a complex ongoing merger with two galactic nuclei and prominent tidal tails visible in optical light (Hutchings & Neff, 1989). It has long been known to be an ultraluminous infrared galaxy and possess a Seyfert 2 AGN (Sanders et al., 1988). In fact, Mrk 463 possesses dual AGN (Bianchi et al., 2008a), with the eastern AGN more luminous than the western AGN. The eastern AGN possesses a hidden BLR in polarized light (Tran, 2001). Two-sided conical [O III] outflows extend from the eastern nucleus (Chatzichristou & Vanderriest, 1995), creating an extended emission line region to the south of the galaxy, similar to a voorwerp (Treister et al., 2018). The eastern nucleus and its ionization cones generate radio fluxes comparable to a radio-loud quasar or radio galaxy (Mazzarella et al., 1991), which is highly unusual for a Seyfert AGN. Based on the amount of energy required to create the observed ionization and emission line features, Treister et al. (2018) argued the eastern AGN was ∼3-20 times more luminous ∼40,000 years ago. They argue that it might become a bona fide quasar in the future as the galaxy merger progresses.

Mrk 463 displays prominent photoionized metal lines in its *XMM-Newton* spectra, including from almost fully stripped Fe XXVI (Imanishi & Terashima, 2004) and the O VII radiation recombination continuum (Bianchi et al., 2008a). It also has a neutral Fe Kα line in its *XMM-Newton* spectra (Imanishi & Terashima, 2004). Both Imanishi & Terashima (2004) and Bianchi et al. (2008a) concluded that Mrk 463 is overall Compton thin. Using the *Chandra* data, Bianchi et al. (2008a) detected a strong Fe Kα line in the eastern nucleus (EW $\simeq$ 250 eV), while only an upper limit could be placed on the Fe Kα line from the western nucleus. The eastern nucleus was also more heavily absorbed. They therefore concluded the eastern nucleus is more obscured than the western nucleus, a claim that is also supported by NIR data.

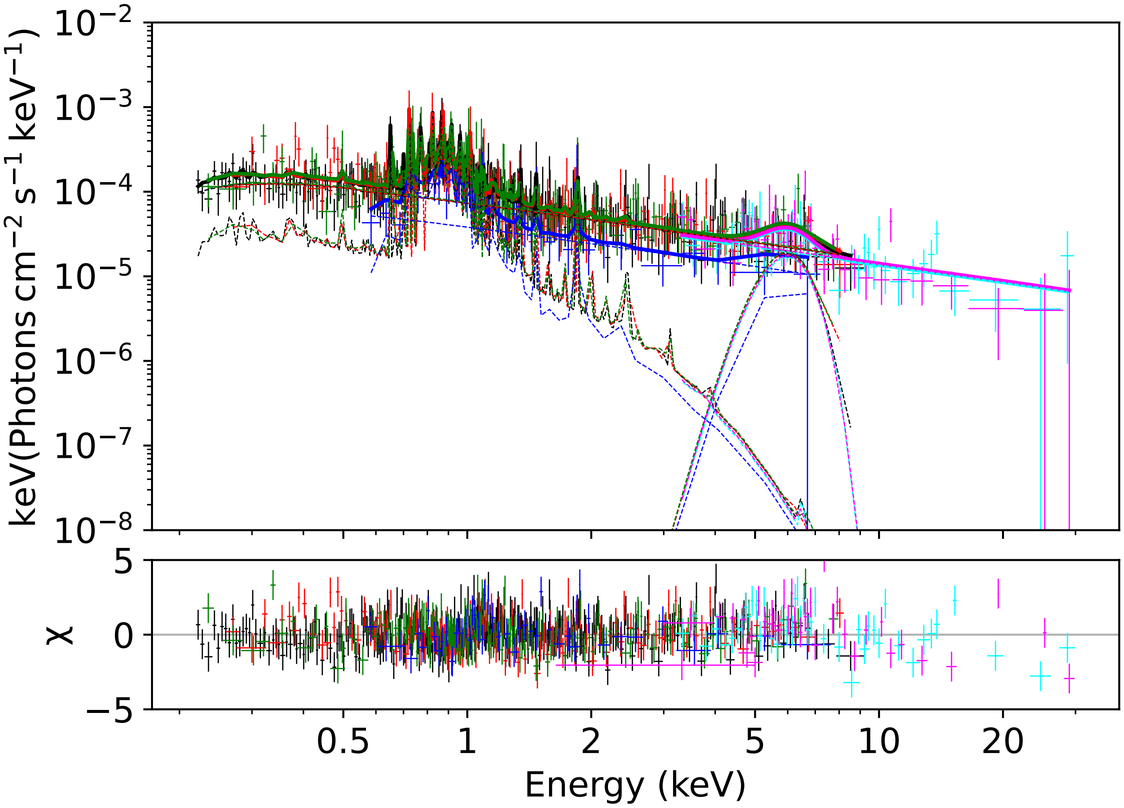

Figure 3.16 Unfolded spectrum and best-fit model for NGC 5005. Black denotes *XMM-Newton* pn data, red denotes *XMM-Newton* MOS1 data, green denotes *XMM-Newton* MOS2 data, blue denotes *Chandra* data, cyan denotes FPMA data, and magenta denotes FPMB data.

3.3.8.1 X-Ray Observations & Data Extraction

Mrk 463 has been observed once by *NuSTAR* and twice by *Chandra*; details of the observations, including the observation dates and exposure times are in Table 3.2.6. The image from the first *Chandra* observation (ObsID: 4913) and the FPMA image from the *NuSTAR* observation are shown side by side in Figure 3.17. The higher resolution *Chandra* image clearly resolves the brighter eastern AGN and the fainter western AGN. An extra-nuclear point source (Source 1) is present in the *NuSTAR* beam. While at first glance the eastern AGN appears to be an elongated ellipse (and indeed was extracted as such by Bianchi et al., 2008a), closer inspection reveals the northern lobe of the ellipse is not part of the AGN, but rather an area of fainter, extended emission that is not detected above 2 keV in energy. It was therefore extracted as a separate source, labeled Source 2. Both extra-nuclear sources have more than 10% the count rate of the fainter, western AGN in the 0.5-8.0 keV band, so they were ultimately used in the fitting.

The eastern and western AGNs were extracted with circular source regions of radius 2" and 1.76", respectively, while Source 1 and Source 2 were extracted with circular source regions of radius 2" and 1.77", respectively.

3.3.8.2 X-ray Spectral Fitting

Similarly to NGC 3627 and NGC 4501, we jointly fit the data freezing Source 1's and Source 2's parameters to the best-fit values from *Chandra* alone. We began with a fit that was simply four POWERLAW components. The soft X-ray spectra of the two AGN and Source 2 (see Figure 3.18) suggest the need for an APEC component, though this is not necessarily true for Source 1. We therefore added APEC components to all the sources but Source 1. The resulting C-stat/d.o.f. was 1673.97/1669.

The *NuSTAR* spectra (see Figure 3.18) show a prominent Fe Kα line and Compton hump, while the *Chandra* spectra for both AGN show a pronounced rise towards the Fe Kα line

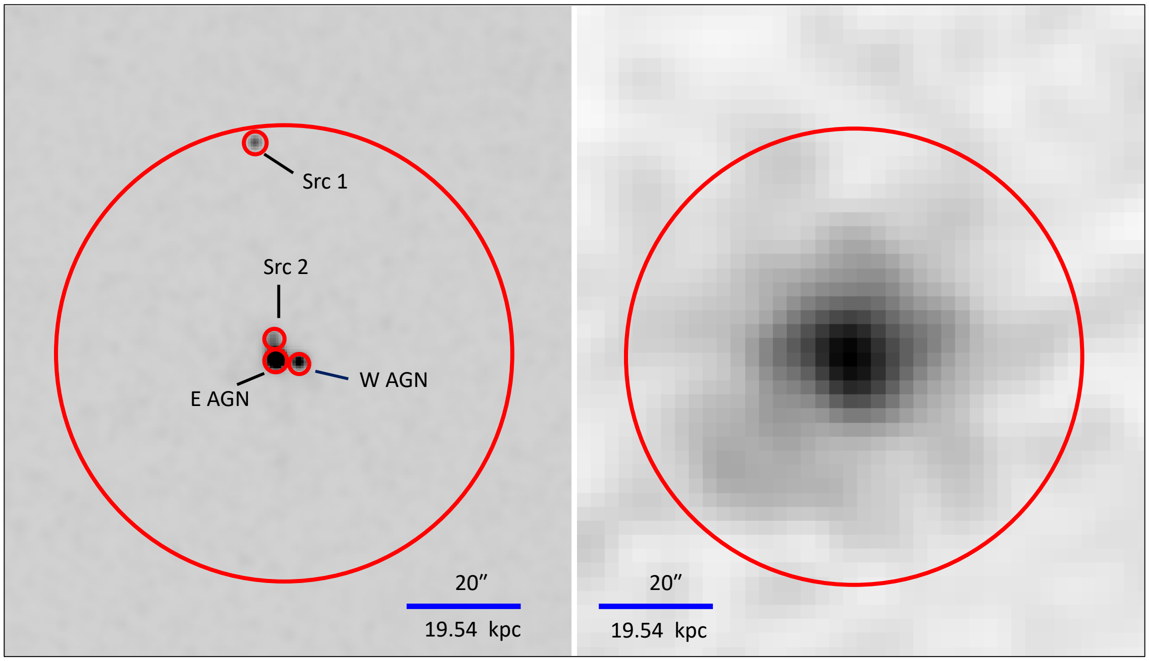

Figure 3.17 *Chandra* (ObsID: 4913) and *NuSTAR* FPMA images of Mrk 463. The larger, 40” radius circle denotes the *NuSTAR* extraction region, while the smaller circles denote the *Chandra* extraction regions. Two extra-nuclear point sources (Source 1 and Source 2) were visible in all *Chandra* observations and were used in the fitting process.

from 4-6 keV. We therefore added a BORUS component to both AGN. Adding it to the east AGN brought C-stat/d.o.f. down to 1517.85/1610, while adding it to the west AGN brought C-stat/d.o.f. down to 1504.83/1610. However, this caused the APEC kT on the east AGN to become implausibly small ($\approx 8 \times 10^{-3}$ keV), APEC kT on the west AGN to be implausibly large (≈ 62 keV), and the constant on the west AGN to be implausibly large ($\approx 4.65 \pm 14$). To resolve these issues we fixed the normalization constants of the west AGN to have an upper limit of 2 and a lower limit of 0.5. C-stat/d.o.f. was brought down to 1469.63/1606. Most of the BORUS parameters remained unconstrained, however, so we froze $\cos(\theta_{\rm inc})$ to 0.17 (i.e., $\theta_{\rm inc} = 80°$). This provided some improvement in C-stat/d.o.f., but some of the BORUS parameters were still not converging. We therefore froze the APEC kT and normalization of both AGN. The final estimates for each parameter are tabulated in Table 3.3.8.2. The best fit model is plotted over the data as the solid lines in Figure 3.18. The logarithm of the 2-10 keV luminosity (in units of $\mathrm{erg\,s^{-1}}$) measured from the model is $44.01^{+0.03}_{-0.10}$ for the eastern AGN and $43.57^{+0.19}_{-0.76}$ for the western AGN.

Table 3.9. Parameters for best-fit Mrk463 model.

Source	APEC		BORUS[a]				POWERLAW	
	kT (keV)	Norm	$\log(N_{\rm H})$	$\mathrm{CF}_{\rm Tor}$	$\cos(\theta_{\rm inc})$	Norm	Γ	Norm
E AGN	$0.91^{+0.10}_{-0.08}$	$12.8^{+3.7}_{-8.2}$	$23.86^{+0.12}_{-0.07}$	$0.27^{+0.09}_{-0.07}$	$0.17^{\rm b}$	$2.73^{+0.18}_{-0.59}$	≤ 1.54	$27.8^{+5.8}_{-15.9}$
W AGN	$1.11^{+0.23}_{-0.20}$	$1.42^{+7.34}_{-0.66}$	$23.50^{+0.10}_{-0.22}$	$0.28^{+0.43}_{-0.03}$	$0.17^{\rm b}$	$4.50^{+2.39}_{-3.73}$	≥ 1.58	$1.30^{+6.00}_{-0.54}$
Src 1							$2.17^{\rm b}$	$4.03^{\rm b}$
Src 2	$0.55^{\rm b}$	$2.6^{\rm b}$					$2.49^{\rm b}$	$2.76^{\rm b}$

Note. — The instrumental normalization constants for *Chandra* observations 4913 and 18194 were $0.66^{+2.96}_{-0.08}$ and $0.65^{+2.68}_{-0.11}$ for the East AGN, $1.00^{+0.16}_{-0.14}$ and $0.71^{+0.45}_{-0.32}$ for Source 1, and $1.01^{+0.13}_{-0.12}$ and $1.61^{+0.69}_{-0.54}$ for Source 2. No errors on the normalization constants for the West AGN could be calculated because a hard lower limit of 0.5 and a hard upper limit of 2.0 were placed on them. The normalizations of the model components are in units of 10^{-6} cts s^{-1} keV^{-1} for APEC, 10^{-3}cts s^{-1} keV^{-1} for BORUS, and 10^{-6} cts s^{-1} keV^{-1} for POWERLAW.

[a] Parameters for this component recovered by freezing APEC component and refitting.

[b] Frozen at this value

3.3.9 NGC 6890

NGC 6890 is a spiral galaxy. Its optical activity has traditionally been classified as Seyfert 2 (e.g., Rush et al., 1996), but it has also been more specifically classified as a S1.9 (Véron-Cetty & Véron, 2006).

NGC 6890's MIR spectrum is dominated by a red continuum suggestive of cool dust and polycyclic aromatic hydrocarbon features (Buchanan et al., 2006), where the latter is indicative of star formation (Deo et al., 2009). Based on its *Spitzer* IRS spectrum, Tommasin et al. (2010) argued roughly 90% of the 19μm emission is due to the AGN. Its MIR morphology is circular and centered on the nucleus (Asmus et al., 2014) but might be somewhat extended (Asmus et al., 2016).

The *XMM-Newton* observations of NGC 6890 were first analyzed by Shu et al. (2007), who fitted it with an unabsorbed powerlaw. However, since its 2-10 keV X-ray flux was significantly depressed compared to its [O III] flux, they still regarded it as a Compton-thick AGN. In contrast, LaMassa et al. (2011) found that the spectrum was best fit with two absorbed powerlaws. They also detected an Fe Kα line at the 93% confidence level. The equivalent width was 1.21 keV if they used a global fit, and 0.93 keV if they used a local fit.

Brightman & Nandra (2011a) presented a more detailed analysis of the *XMM-Newton* data, including fits with PEXMON and TORUS models to account for a reflection component. They measured a hydrogen column density of 10^{21} cm^{-2} for this reflection component, which would put it outside the Compton-thick regime.

3.3.9.1 X-Ray Observations & Data Extraction

NGC 6890 has not been observed by *Chandra*, but has been observed by *XMM-Newton* once, by *Swift* twice, and by *NuSTAR* once. The *NuSTAR* observation was concurrent with the second *Swift* observation. Details of these observations, including their observation dates

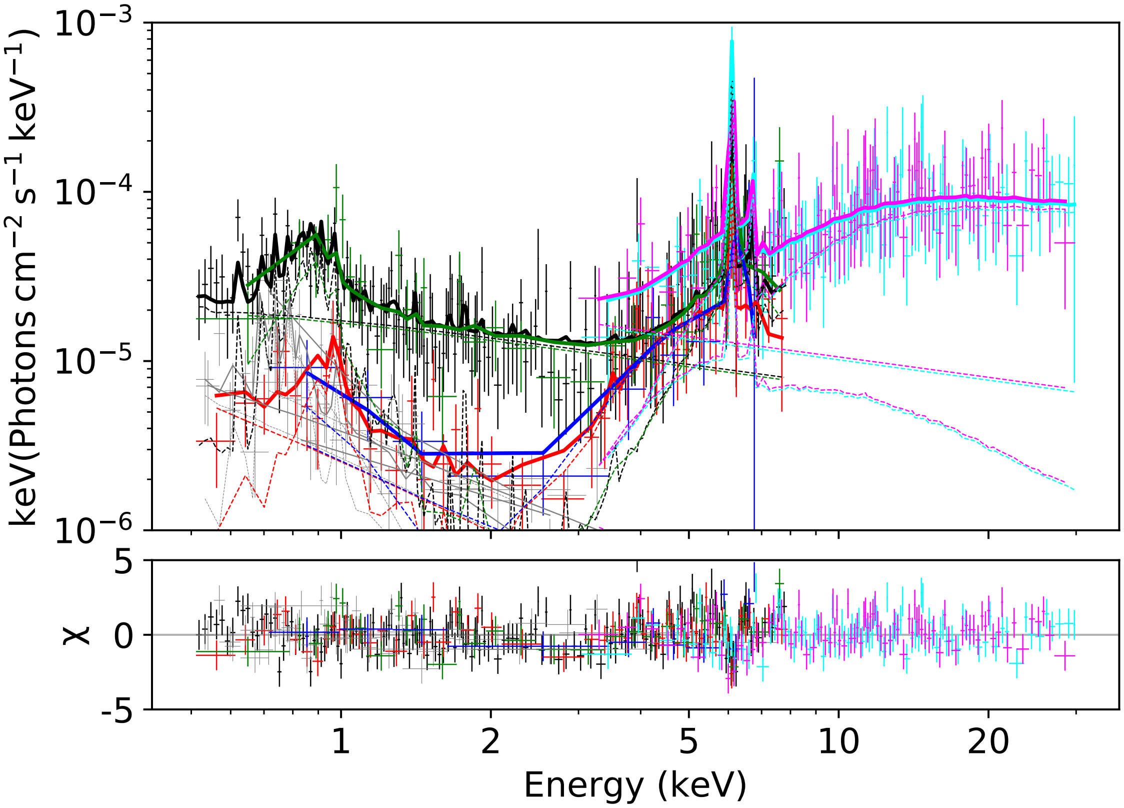

Figure 3.18 Unfolded spectrum and model for Mrk 463. The model shown is the fit with all the APEC parameters frozen (i.e. the fit that was used to recover the BORUS parameters). Black denotes *Chandra* observation 4913 of the east AGN. Red denotes *Chandra* observation 4913 of the west AGN. Green denotes *Chandra* observation 18194 of the east AGN. Blue denotes *Chandra* observation 18194 of the west AGN. Cyan and magenta represent *NuSTAR* FPMA and FPMB data respectively. The *Chandra* observations of Source 1 and Source 2 are depicted in light grey.

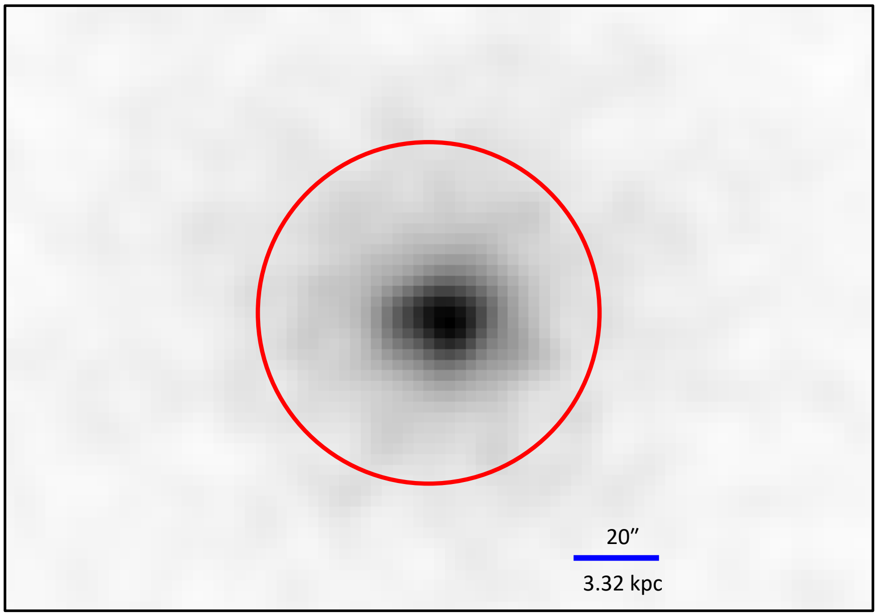

Figure 3.19 *NuSTAR* FPMA image of NGC 6890. The *XMM-Newton* data, which have lower anguler resolution than *Chandra*, did not detect any off-nuclear point sources within the *NuSTAR* beam (shown in red).

and exposure times, are in Table 3.2.6.

For the *XMM-Newton* data, we filtered out times with high background, defined as when the count rate in the 10–12 keV range was >0.4 cts s^{-1} for the pn and >0.35 cts s^{-1} for the MOS cameras. We extracted the source spectra with 30” radius circular regions, and background spectra from an annulus of 50” − 80” with pattern 0–4 for the pn and pattern 0–12 for the MOS cameras.

3.3.9.2 X-ray Spectral Fitting

We began with a simple CONSTANT*TBABS*POWERLAW model. The C-stat/d.o.f. for this fit was 1951.31/1580, implying room for improvement. A BORUS component improved C-stat/d.o.f. to 1736.27/1576. We then added an APEC component, which improved C-stat/d.o.f. to 1724.84/1574. Looking at the unfolded spectrum (Figure 3.20), the BORUS component seems to have a higher intensity in the *Swift* and *NuSTAR* data than in the *XMM-Newton* data. The APEC component of the *XMM-Newton* data is of similar flux density to the *NuSTAR* data, but energies in the *XMM-Newton* data above 1 keV do not match up with the *NuSTAR* data.

To test the possibility that the BORUS component was varying, we created fits where $N_{\rm H}$ and the BORUS normalization varied between each observation. When these parameters were left free to vary, their values for the *XMM-Newton* MOS1 and MOS2 data were tied to the EPIC pn value, and their *NuSTAR* FPMB and FPMA values were tied together. The values for the *Swift* observations were left to freely vary independently. We set the cross-normalization constants all to 1. For the case of $N_{\rm H}$ varying, C-stat/d.o.f. was 1886.20/1576. For the case of the BORUS normalization varying, C-stat/d.o.f. was 1828.16/1576. And for the case of both $N_{\rm H}$ and the BORUS normalization varying, C-stat/d.o.f. was 1836.111/1573.

The best fit seemed to be the one where only the BORUS normalization varied. However, adding $N_{\rm H}$ variability should not have made the fit worse than the fit with the normalization varying alone. We therefore freed $N_{\rm H}$. We then reset $\log(N_{\rm H}/{\rm cm}^{-2})$ to be 25.5 for *XMM-Newton* and 23 for *Swift* and *NuSTAR* and refit. This led to a C-stat/d.o.f. = 1810.31/1573. However, the POWERLAW component was underestimating the *XMM-Newton* data. We therefore untied the POWERLAW spectral index from the BORUS spectral index. This allowed the scattered powerlaw to differ from the intrinsic powerlaw input to the BORUS model. This fit had a C-stat/d.o.f. of 1711.07/1572.

We next tied the values of $N_{\rm H}$ and the BORUS normalization for the second *Swift* observation and *NuSTAR* together, since these observations were contemporaneous. Lastly we thawed the cross-normalization constants, setting limits of 0.5-2.0 on all of them. The final C-stat/d.o.f. was 1699.97/1569, the parameters of the final fit are in Table 3.3.9.2, and the fit is plotted over the data in Figure 3.20. The logarithms of the 2-10 keV luminosities (in units of $\rm erg\,s^{-1}$) measured from the model from each epoch are $42.25^{+0.89}_{-0.24}$ for September 2009,

$42.73^{+0.33}_{-0.48}$ for March 2018, and $43.66^{+0.09}_{-0.01}$ for May 2018.

Table 3.10. Parameters for best-fit NGC 6890 model.

Observation	APEC		BORUS					POWERLAW	
	kT (keV)	Norm	Γ	$\log(N_{\rm H})$	$\rm CF_{Tor}$	$\cos(\theta_{\rm inc})$	Norm	Γ	Norm
XMM-Newton	$0.73^{+0.14}_{-0.15}$	$7.14^{+9.64}_{-3.54}$	≤ 1.41	$24.12^{+0.29}_{-1.10}$	≤ 0.10	≤ 0.10	$1.89^{+13.1}_{-0.78}$	$2.71^{+0.15}_{-0.20}$	$2.95^{+4.28}_{-0.27}$
1st *Swift*				$23.40^{+0.86}_{-0.88}$			$5.81^{+6.67}_{-3.88}$		
2nd *Swift*/*NuSTAR*				$23.01^{+0.02}_{-0.12}$			$49.5^{+11.4}_{-1.3}$		

Note. — The instrumental normalization constant for *XMM-Newton* MOS2 was $1.46^{+0.19}_{-0.18}$. The rest were pegged at the upper limit of 2. The BORUS Γ and $\rm CF_{Tor}$ constraints were derived by freezing the BORUS $\log(N_{\rm H})$ and Normalization at their best fit values in all observations. The normalizations are in units of 10^{-6} cts s^{-1} keV^{-1} for APEC, 10^{-3} cts s^{-1} keV^{-1} for BORUS, and 10^{-5} cts s^{-1} keV^{-1} for POWERLAW.

3.4 Discussion

In this section we discuss the implications of our results. § 4.1 discusses how the intrinsic luminosities of the AGN were derived. § 4.2 compares these luminosities to those expected from scaling relations. § 4.3 discusses the obscuration levels measured from the X-ray spectral fits. § 4.4 describes how Eddington ratios were computed and whether there are any correlations observed with Eddington ratio. Lastly § 4.5 explains in further detail special features observed in the individual galaxies.

3.4.1 Intrinsic Luminosities

The 9 AGN in the sample have low observed *XMM-Newton* 2-10 keV luminosities. Recall this can mean one of two things: that the AGN is heavily obscured, or that the AGN is recently deactivated. Observations in the hard X-ray band from *NuSTAR* are essential for distinguishing between the two scenarios. With hard X-ray data, we can model the spectrum more accurately, and from that model we can estimate the true intrinsic 2-10 keV luminosity. In the case of an obscured AGN, we would expect to see additional flux at higher energies, where the photons have enough energy to penetrate the obscuring torus. This would lead to a modeled intrinsic X-ray luminosity that is higher than that originally derived from observed 2-10 keV fluxes. If an AGN has recently deactivated, we will not observe additional X-rays from the AGN at higher energies. This means the 2-10 keV band will capture most of the AGN's X-rays, and so the intrinsic luminosity inferred from the model will be similar to that inferred with the 2-10 keV observed fluxes alone.

For most of the AGN in the sample, there was a jump by several orders of magnitude between the observed and intrinsic X-ray luminosities. This indicates that they are obscured AGN, as the hard X-ray data indicate their modeled spectra have to be more luminous in the 2-10 keV band than directly observed. For NGC 3627 and NGC 5005 however, the change in X-ray luminosity between observed and intrinsic was within an order of magnitude. This

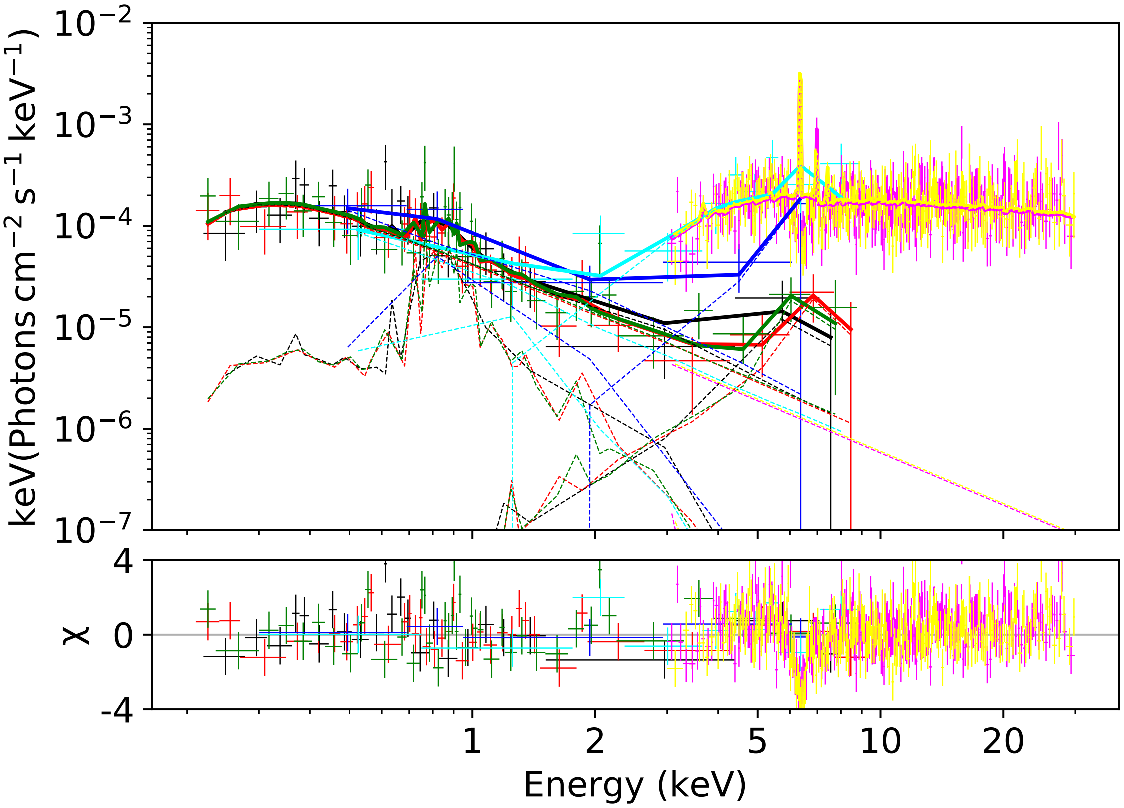

Figure 3.20 Unfolded spectrum and best-fit model for NGC 6890. Black denotes *XMM-Newton* pn data, red denotes *XMM-Newton* MOS1 data, green denotes *XMM-Newton* MOS2 data, blue denotes data from *Swift* observation 00088188001, cyan denotes data from *Swift* observation 0008818800, and magenta and yellow denote *NuSTAR* FPMA and FPMB data, respectively.

Table 3.11. Summary of AGN Properties.

Object	Type	$\log(M_{\rm BH})$ ($M_\odot$)	$\log(N_{\rm H})$ ($\rm cm^{-2}$)	$\log(L_{2-10})$ ($\rm erg\,s^{-1}$)	$\log(L_{\rm [OIII]})$ ($\rm erg\,s^{-1}$)	$\log(L_{\rm MIR})$ ($\rm erg\,s^{-1}$)	$L_{\rm bol}/L_{\rm Edd}$	Refs
NGC 1386	S1i	7.24	≥ 24.5	42.29 ± 0.05	40.16	42.39 ± 0.08	1.38×10^{-2}	1,2,6,10
NGC 3627	S3	6.93	-	$38.38^{+0.16}_{-0.10}$	39.40	40.60 ± 0.11	3.67×10^{-6}	1,3,6,10
NGC 3982	S1.9	6.95	≥ 25.3	$42.83^{+0.13}_{-0.08}$	39.87	41.56 ± 0.06	9.50×10^{-2}	1,4,6,10
NGC 4501	S2	7.30	$22.87^{+0.25}_{-0.15}$	$41.50^{+0.25}_{-0.11}$	39.86	40.56 ± 0.06	1.93×10^{-3}	1,3,6,10
IC 3639	S1h	7.01	$25.00^{+0.06}_{-0.26}$	$43.07^{+0.18}_{-0.12}$	42.0	43.52 ± 0.04	0.146	1,4,7,10
NGC 4922	S2		$23.89^{+0.11}_{-0.17}$	$42.29^{+0.12}_{-0.47}$	42.3			1,8
NGC 5005	S3b[a]	8.27	-	$40.17^{+0.04}_{-0.05}$	39.03	40.78 ± 0.12	9.67×10^{-6}	1,4,6,10
Mrk 463	E: S1h		$23.86^{+0.12}_{-0.07}$	$44.01^{+0.03}_{-0.10}$	42.62[b]	44.83		1,9,11
	W: S2		$23.50^{+0.10}_{-0.22}$	$43.57^{+0.19}_{-0.76}$				
NGC 6890	S1.9	7.07			42.02	42.60 ± 0.09		1,5,6,10
— 2009 Sep			$24.12^{+0.29}_{-1.10}$	$42.25^{+0.89}_{-0.24}$			1.86×10^{-2}	
— 2018 Mar			$23.40^{+0.86}_{-0.88}$	$42.73^{+0.33}_{-0.48}$			5.70×10^{-2}	
— 2018 May			$23.01^{+0.02}_{-0.12}$	$43.66^{+0.09}_{-0.01}$			0.530	

[a] Broad component detected in Hα, no others.

[b] Combined $\log(L_{\rm [OIII]})$ for E and W components of Mrk 463, not corrected for intrinsic dust extinction.

Note. — S1i indicates a Seyfert 2 with broad lines detected in the infrared, S1h indicates a Seyfert 2 with a hidden BLR detected in polarized light, S1.9 denotes a Seyfert with broad Hα but no broad Hβ, and S3 indicates a LINER. L_{2-10} is the intrinsic absorption-corrected X-ray luminosity. MIR luminosities are at 12 μm. Bolometric luminosities were computed using $K_X(L_X)$ from Table 1 of Duras et al. (2020). Error bars on luminosities are given if available. Ref is references for optical classification, $M_{\rm BH}$, $L_{\rm [OIII]}$, and $L_{\rm MIR}$. NGC 6890's entries are written in temporal order order: 2009 Sep = *XMM-Newton* observation; 2018 Mar = first *Swift* observation; 2018 May = second *Swift* observation + *NuSTAR* observation.

References. — (1) Véron-Cetty & Véron (2010), (2) Woo & Urry (2002), (3) Saglia et al. (2016), (4) van den Bosch (2016) & references therein, (5) Meléndez et al. (2010), (6) Brightman & Nandra (2011b) and references therein, (7) Boorman et al. (2016), (8) Luo et al. (2021) and references therein, (9) Heckman et al. (2005) and references therein, (10) Asmus et al. (2015), (11) Alonso-Herrero et al. (2016).

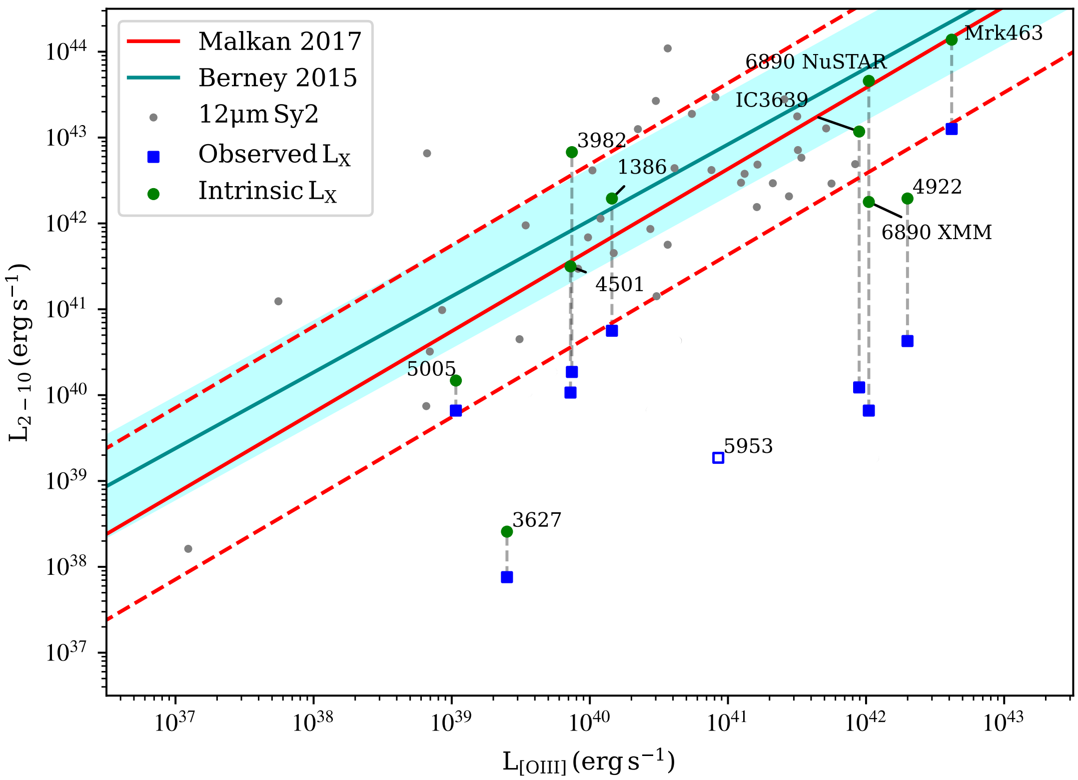

Figure 3.21 Intrinsic 2-10 keV X-ray luminosities versus updated [O III] luminosities for the galaxies in our sample. The instrinsic luminosities are plotted alongside their former positions from Figure 3.1. The Mrk 463 2-10 keV luminosity is the combined luminosity of the eastern and western AGNs. IC 3639 has been moved slightly to the left to better distinguish it from NGC 6890.

indicates that they are not as heavily obscured as the other AGN in the sample.

3.4.2 Scaling Relations

The hard X-ray continuum from an AGN is believed to originate from the corona, located very close to the central black hole ($\leq$ 0.1pc Ichikawa & Tazaki, 2017), which translates to a light-crossing time of the corona of less than 3 months, and it is known from observations that the corona can vary in timescales of days (e.g., Wilkins et al., 2014; Keck et al., 2015; Ricci et al., 2020). In contrast, the MIR emission from the torus and the [O III] emission

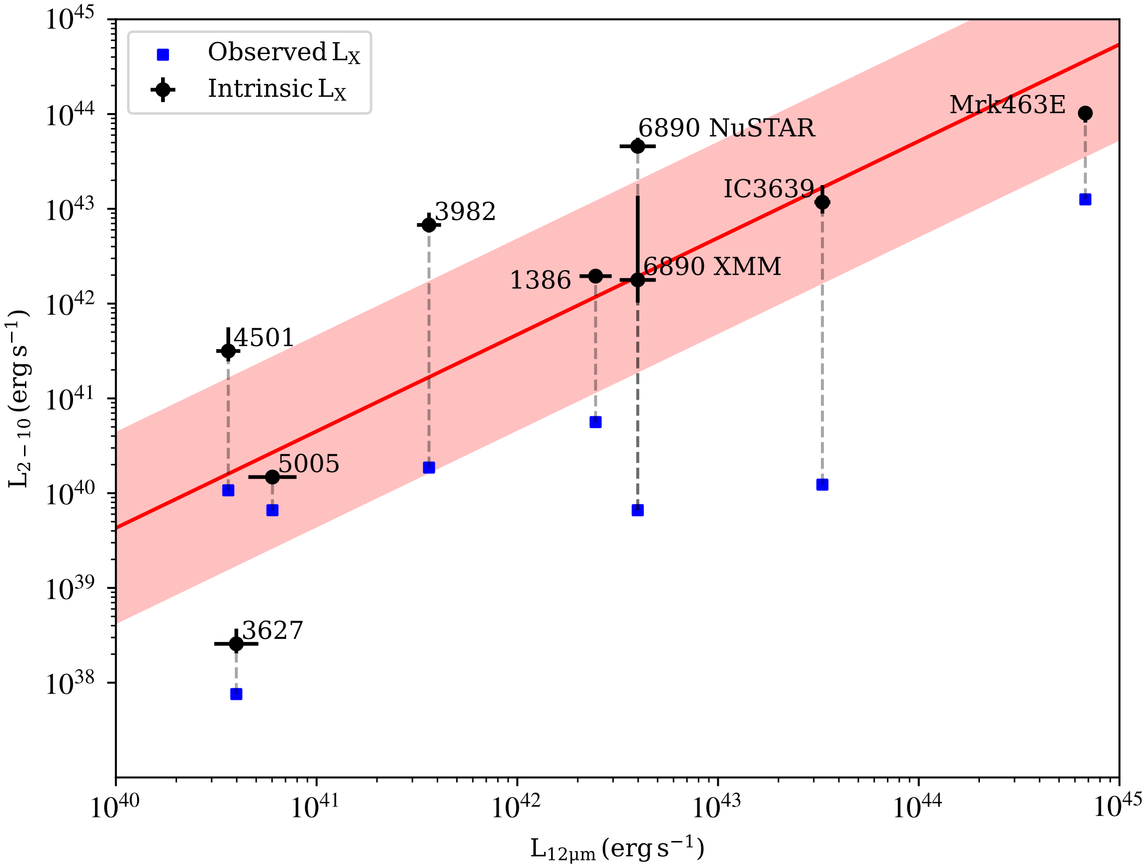

Figure 3.22 Intrinsic 2-10 keV X-ray luminosities versus 12μm luminosities for the galaxies in our sample. The blue squares are the galaxies plotted with observed 2-10 keV luminosities. The black points with errorbars use the intrinsic 2-10 keV luminosities. The red line is the mean L_{2-10} vs $L_{12\mu m}$ relation for the complete reliable sample in Asmus et al. (2015). The scatter of this relation is 0.33 dex which is depicted as the light red shaded region. L_{2-10} errors were derived from our measurements as explained in Section 4. Errors on $L_{12\mu m}$ are derived from the literature.

from the NLR originate from much further out could only vary *much* more slowly. Therefore, when an AGN deactivates, the corona will fade out well before the torus and NLR do, on timescales far shorter than theirs (i.e. days vs. decades and centuries). We therefore expect a recently deactivated AGN to have an intrinsic X-ray luminosity well below that which is expected based on its [O III] and MIR luminosities. If, in contrast, the AGN is merely heavily obscured, we would expect to find an intrinsic X-ray luminosity consistent with its [O III] and MIR luminosities.

In Figure 3.21 we plot the intrinsic 2-10 keV luminosities of our sample on 3.1. The red line is the mean $L_{[\mathrm{OIII}]}$ vs L_{2-10} relation for Seyfert 1 galaxies in the 12 μm sample, and the dashed red lines represent one dex above and below it. It is derived from the observed luminosities in Malkan et al. (2017). Most of the galaxies lie within 1 dex of the mean relation when the intrinsic 2-10 keV luminosity is considered. NGC 3982 does lie more than one dex above it. However, it is still placed within the scatter of the other Seyfert 2 galaxies in the 12 μm sample. NGC 4922 is more than 1 dex below the mean relation. But by far the furthest outlying galaxy is NGC 3627, located more than 2 dex below from the mean correlation. This makes it the strongest candidate for its corona having faded relative to the luminosity inferred from the NLR.

In Figure 3.22, we plot the observed and intrinsic 2-10 keV luminosities of our sample versus their 12μm luminosities. The 12μm luminosities are derived mostly from Asmus et al. (2015), which had the subarcsecond resolution necessary to resolve the nuclear MIR emission and separate it from the overall host galaxy emission. The exceptions to this are NGC 4922, for which no 12μm luminosities could be found in the literature, and Mrk 463, for which the 12μm luminosity was taken from Alonso-Herrero et al. (2016).

The red line is from Asmus et al. (2015) and represents their estimate of the $L_{12\mu\mathrm{m}}$ vs L_{2-10} correlation using their entire reliable sample. This relation has an intrinsic scatter of 0.33 dex, which is shown as the light red shaded region. With the original observed estimates of the 2-10 keV luminosity, all the AGN except for NGC 4501 are located more than 0.33 dex below the mean relation. With the absorption-corrected intrinsic 2-10 keV luminosity, NGC 3982, NGC 4501, and NGC 6890 lie more than 1 dex above it. For NGC 6890 this is clearly due to the increase in luminosity observed in the X-ray data. Because the torus is located further out than the corona, this could imply the corona has gotten brighter in recent years for the other two X-ray overluminous AGN as well, while the torus has yet to respond to the increase in luminosity.

Once again, NGC 3627 is the furthest below the mean relation, more than 1 dex below it. This can be taken to represent deactivation of the corona while the torus continues to be emitting. According to Ichikawa & Tazaki (2017) the torus fading timescale is dominated by the light crossing time. This leads to a fading timescale of around 10-100 years based on typical sizes of the torus. This would imply that NGC 3627 deactivated no more than 10-100 years ago, since this galaxy still preserves torus emission. Indeed, the conclusion of Esparza-Arredondo et al. (2020) was that NGC 3627 has faded on timescales of decades. However, NGC 3627's 12μm emissions are distributed throughout the galaxy, so it is unclear how much of the nuclear 12μm contribution is from an AGN torus as opposed to star formation.

3.4.3 Obscuration

Of the galaxies in our sample, all but two have the X-ray spectra typical of obscured AGN, displaying the soft thermal emission from 0.5-2 keV, a hard reflection component and narrow Fe Kα line, and the Compton hump at ~ 20 keV (for examples, see NGC 1386 or IC 3639). The hydrogen column densities of the AGN are summarized in Table 3.11. We replicate the result that NGC 1386 and IC 3639 are Compton-thick. NGC 3982 is also Compton-thick. NGC 4501, NGC 4922, and both AGNs in Mrk 463 are obscured, but not quite at the Compton-thick level. NGC 6890 was nearly Compton-thick during the time of its *XMM-Newton* observations, but became definitively Compton-thin during later observations. This makes it a new X-ray changing-look AGN (e.g. Matt et al., 2003). NGC 3627 and NGC 5005 are unobscured.

It is noteworthy that our selection method (searching for AGN that are underluminous in soft X-rays relative to their [O III] luminosity), which is a common method of selecting Compton thick AGN candidates, resulted in a sample where only 33% of the objects were actually Compton thick at the time of their *NuSTAR* observations. Most (77%) of the AGN are indeed heavily obscured ($N_{\rm H} > 10^{23}\,{\rm cm}^{-2}$).

3.4.4 Eddington Ratios

We computed the bolometric luminosities from the intrinsic 2-10 keV luminosities using the general expression for $\kappa_X = L_{\rm bol}/L_X$ from Table 1 of Duras et al. (2020). We then converted these to Eddington ratios using the most recent black hole masses available in the literature.

We find that the obscured AGN are accreting at a higher rate (i.e. $L_{\rm bol}/L_{\rm Edd} > 10^{-3}$) than the two AGN that do not show evidence of obscuration (NGC 3627 and NGC5005; $L_{\rm bol}/L_{\rm Edd} \sim 10^{-6}$). Of note is that the most heavily obscured AGN, IC 3639, has an Eddington ratio of 0.146, more typical of quasars than Seyfert galaxies, and that NGC 6890's Eddington ratio increased by an order of magnitude between its *XMM-Newton* and *NuSTAR* observations, for a final ratio of 0.530.

There is no clear correlation between Eddington ratio and the position of the AGN on the $L_{\rm [OIII]}$ vs L_{2-10} relation for the sample as a whole, as the high Eddington ratio AGN IC 3639 and NGC 6890 are near the mean relation (as are low Eddington ratio AGN NGC 1386, NGC 4501, and Mrk 463) while low Eddington ratio NGC 3982 lies more than 1 dex above it. The very lowest Eddington ratio AGN (NGC 3627 and NGC 5005) are located at two very different positions in the graph, with NGC 5005 being only 1 dex away from the mean relation, while NGC 3627 lies more than 2 dex away.

The same is true for the $L_{12\mu{\rm m}}$ vs L_{2-10} relation, as low Eddington ratio NGC 3982 and NGC

4501 lie more than 1 dex above the mean relation like high Eddington ratio NGC 6890. NGC 5005 is within the intrinsic scatter of the relation, but NGC 3627 is not.

3.4.5 Notes about Individual Galaxies

3.4.5.1 NGC 3627

The *NuSTAR* data for NGC 3627 were recently analyzed and concluded to show evidence of a Compton-thick nature for this AGN (Esparza-Arredondo et al., 2020). However, this is clearly not the case for our analysis of the data (§ 3.2), which shows no evidence for a reflection component, and thus no evidence for obscuration. This would seem to favor the fading AGN scenario for this galaxy, since it is well below the X-ray luminosity expected for its MIR luminosity. However, it is still possible that a stronger AGN could be hidden behind extremely high levels of obscuration (such that not even the hard X-rays are able to escape). This scenario can not be completely ruled out by *NuSTAR*; a more sensitive hard X-ray telescope could potentially do so. In the case of a strong, extremely obscured AGN, we would still expect strong MIR emission, as the dusty torus would still be heated. Given the AGN in NGC 3627 does not dominate above the MIR background of its host galaxy, it seems likely this AGN is intrinsically low-luminosity. If we accept the measured 2-10 keV luminosity of $10^{38.38}\,\mathrm{erg\,s^{-1}}$ as the true intrinsic luminosity, NGC 3627's luminosity is below the Eddington luminosity of a stellar black hole ($1.26 \times 10^{39}\,\mathrm{erg\,s^{-1}}$ for a 10 $M_{\odot}$ black hole). It therefore might not even be a currently active AGN by some definitions, even though it does present as one on the BPT diagram.

Many correlations between AGN [O III] luminosity and NLR size have been published. Following the prescription of Ichikawa & Tazaki (2017), we use the correlation from Bae et al. (2017) which spatially separated AGN [O III] emission from larger, star formation driven [O III] emission based on integral-field unit spectroscopy of nearby type 1 and type 2 AGN. That prescription is:

$$\log(R_{\mathrm{NLR}}) = 0.41\,\log(L_{\mathrm{[OIII]}}) - 14.00, \tag{3.2}$$

where the NLR radius R_{NLR} is in units of parsec and the luminosity is in units of $\mathrm{erg\,s^{-1}}$. Plugging in the non-reddening corrected [O III] luminosity for NGC 3627, we get a NLR radius of 27.2 pc.

The overall size of the [OIII] emitting region can be estimated as well. We use the relation for Seyfert galaxies from Schmitt et al. (2003):

$$\log(R_{\mathrm{[OIII]}}) = 0.33\,\log(L^{\mathrm{int}}_{\mathrm{[OIII]}}) - 10.78, \tag{3.3}$$

where the radius is in units of parsec and the luminosity is in units of $\mathrm{erg\,s^{-1}}$ and is intrinsic (i.e. reddening-corrected). Plugging in our reddening-corrected [O III] luminosity, this relation gives $R_{\mathrm{[OIII]}} = 67.3$ pc. The resulting timescale for fading based on light-crossing times implies that the central AGN in NGC 3627 deactivated no earlier than 87 - 220 years ago.

3.4.5.2 NGC 5005

Lacking a prominent hard X-ray reflection component, NGC 5005 does not present a typical obscured AGN X-ray spectrum (§ 3.7). This could indicate that the AGN is currently inactive, and we are only seeing softer X-ray emission from star formation. However, since its optical spectrum exhibits a broad Hα component, the simplest conclusion is that this AGN is actually unobscured. This is in contrast to many of its classifications in the literature, which refer to it as a Seyfert 2. It is hypothetically conceivable that the central black hole in this source has faded relative to the BLR, but the extreme rapidity of the timescale of which this would occur given the 10s-100s of light days size of the BLR makes this very unlikely.

As noted previously, *NuSTAR* data on NGC 5005 show a broad emission line centered on 5.91 keV, but this is not seen in the *XMM-Newton* and *Chandra* data. Based on our MC simulations, this line is a real feature. In being broad it resembles the relativistic iron lines that have been observed in other AGN (e.g., Brenneman & Reynolds, 2006; Risaliti et al., 2013; Walton et al., 2020), and the centroid energy lower than the rest-frame energy transition at 6.4 keV of the line suggests it is gravitationally redshifted, like some of the relativistically broadened lines observed in Seyfert galaxies (e.g., Nandra et al., 2007).

We fit the *NuSTAR* spectra of NGC 5005 with the relativistic reflection model RELXILL (version 1.4.3; García et al., 2014; Dauser et al., 2014, 2016). We first used all the default parameter values for the model except for the iron abundance and redshift, which we froze to solar and the redshift of the galaxy. The fit was better than both a BORUS+POWERLAW model fit just to the *NuSTAR* data, and the ZGAUSS*POWERLAW fit used in Section 3. However, the black hole spin parameter, a, could not be well constrained, and the reflection fraction was too high to be physical (i.e. reflection fraction > 10 for spin $a < 0.9$). The reflection fraction is defined as the ratio of the amount of observed radiation reflected off of the accretion disk to the amount of radiation directly transmitted to the observer from the corona. For a given spin value of the black hole there is a maximum possible value of this fraction (see Figure 3 in Dauser et al., 2014). We therefore fit the spectrum with the black hole spin fixed to a variety of values, and set the upper limit on the reflection fraction set to the upper limits from Dauser et al. (2014). The C-stat declined continuously as the spin increased, and the best fit was obtained with a near-maximum spin value ($a = 0.998$). Given the strength of the broad line in NGC 5005, a high spin is clearly favored, as this allows a higher reflection fraction (in this case, > 12). We have plotted that fit in Figure 3.23. The C-stat/d.o.f. for this fit was comparable to that of the ZGAUSS+POWERLAW fit, but not lower.

3.4.5.3 NGC 6890

NGC 6890 varied in both obscuration and luminosity between the time of its *XMM-Newton* and *NuSTAR* observations (§ 3.9). The observed change in luminosity makes NGC 6890

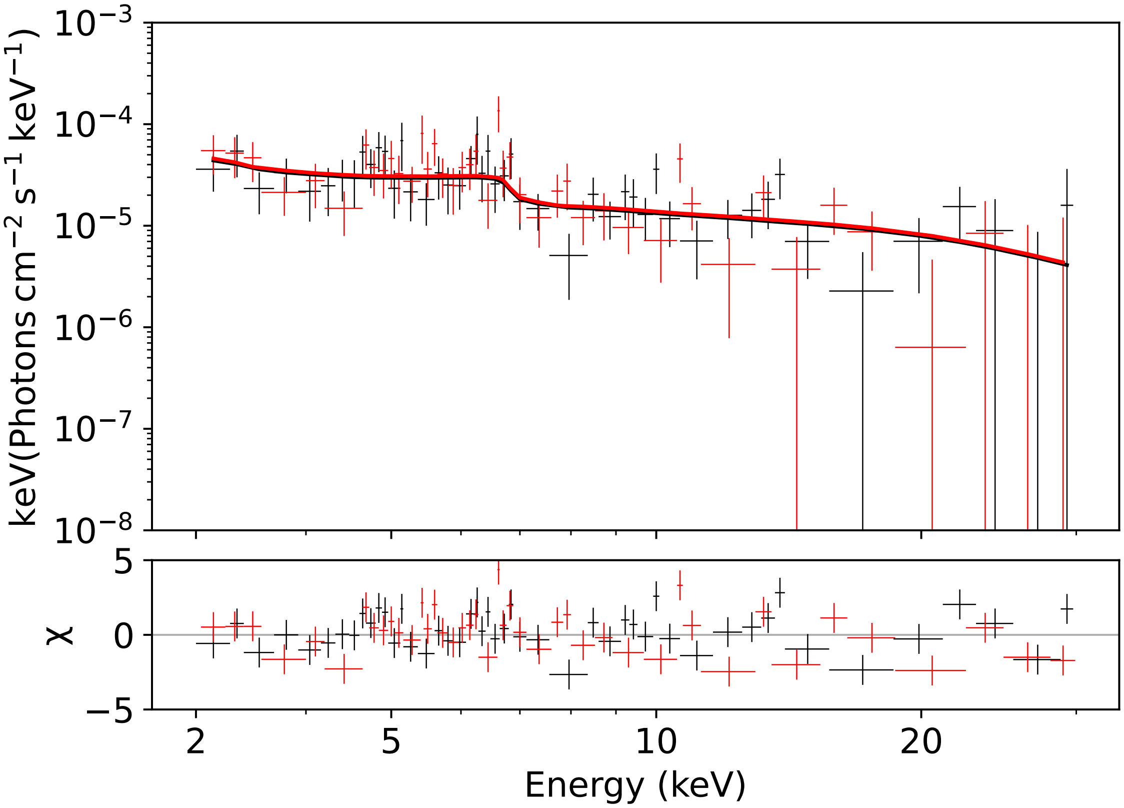

Figure 3.23 Unfolded spectrum and best-fit model for NGC 5005 *NuSTAR* data using a TBABS*RELXILL model and realistic reflection fraction values. Black is FPMA data, red is FPMB data. The spin in this case is a=0.998.

different from many other X-ray changing-look Seyfert galaxies, which have been traditionally interpreted as varying in obscuration alone (e.g. Risaliti et al., 2002), the most famous of which is NGC 1365, which shows rapid variability in absorption levels (Risaliti et al., 2002; Walton et al., 2014; Rivers et al., 2015). However, other types of changing-look AGN, such as changing-look quasars (which vary between optical classifications; e.g. Graham et al., 2020), are thought to indeed be due to physical changes in the accretion disk (e.g. Stern et al., 2018; Ross et al., 2018; Ai et al., 2020) and/or accretion rate (e.g. LaMassa et al., 2015; Runnoe et al., 2016; MacLeod et al., 2016; Gezari et al., 2017; Wang et al., 2018). NGC 6890's increase in luminosity by an order of magnitude implies a change in the central engine. This might make it more similar to optical-changing look AGN than to NGC 1365, and/or lend credence to the hypothesis that a decrease in the magnitude of an X-ray reflection component could also be caused by AGN brightening in addition to reduced obscuration (Matt et al., 2003).

3.4.6 Implications for AGN Variability and Duty Cycle

Previous attempts to search for fading AGN have often relied on finding extended emission line regions, such as the Voorwerpen (e.g., Lintott et al., 2009; Keel et al., 2012b,a; Sartori et al., 2018) and green beans (e.g., Schirmer et al., 2013; Davies et al., 2015). These have probed fading timescales of $10^4 - 10^5$ years. Because our sample, which is a subset of the *IRAS* 12 μm Seyfert sample, identified AGN with strong MIR torus emission but apparently lacking coronal X-ray emission, we have probed much shorter fading timescales (decades and centuries). While our sample does include one Voorwerp in Mrk 463E, it is distinctly different from the green beans sample, probing a lower [O III] luminosity than that sample (i.e., $L_{\rm [OIII]} > 10^{43}\,{\rm erg\,s^{-1}}$ for the green beans).

The Malkan et al. (2017) X-ray and [O III] data that was used as the initial starting point for our sample included 39 Seyfert 1 AGN and 47 Seyfert 2 AGN. We can presume the Seyfert 1 AGN are currently active, and of the 47 Seyfert 2 AGN, we found one candidate recently deactivated AGN. This is a rate of approximately 1%. That we were able to find one recently deactivated AGN in a sample of 86 AGN suggests that recently deactivated AGN may be more common than previously thought.

A majority of our sources are mergers in progress (Mrk 463, NGC 4922) or located close to other galaxies and thereby potentially interacting (NGC 1386, NGC 3627, IC 3639). These results together could be understood in a context of merger/interaction-induced AGN activity (e.g., Hopkins et al., 2008).

The timescale of NGC 3627's fading is shorter than the $\sim 10^4 - 10^5$ year viscous timescale for AGN but it is also longer than the ~10 year thermal timescales used to explain changing-look AGN (Stern et al., 2018). This could imply that AGN can vary on timescales intermediate between these two timescales, but it could also simply be we are observing the beginning of a viscous-timescale-related fading.

3.5 Conclusions

In this paper, we presented *NuSTAR* observations of 9 AGN underluminous in the 2-10 keV X-rays from the 12 μm galaxy sample. We combined these *NuSTAR* data with *Chandra*, *Swift*, and *XMM-Newton* data as necessary to perform broad-band X-ray spectral fitting and determine whether these AGN were truly intrinsically underluminous and potentially deactivated, or simply heavily obscured. We find that all but NGC 5005 and NGC 3627 are obscured AGN, whereas NGC 5005 and NGC 3627 are intrinsically low luminosity. Of the two low-luminosity AGN, NGC 3627 appears to not be active. Since this galaxy preserves NLR [O III] emission and nuclear MIR emission, we conclude that it is a candidate recently deactivated AGN, having turned off no more than 87-220 years ago.

CHAPTER 4

NuSTAR Observations of Candidate Binary Supermassive Black Holes[1]

4.1 Introduction

Binary supermassive black holes (SMBHs) are expected to be a ubiquitous consequence of galaxy mergers. When two galaxies merge, their corresponding SMBHs will pair up into binaries. The binary separation will shrink due to gravitational interactions with stars (Berczik et al., 2006; Gualandris et al., 2017) and gas (Mayer et al., 2007) in the merged galaxy. When the binary reaches sub-parsec separation, gravitational waves become the dominant mode by which the binary shrinks, allowing the two black holes to spiral together and merge (Begelman et al., 1980). In the process they will release gravitational waves that could be detected by future observatories such as the *Laser Interferometric Space Antenna* (*LISA*; Amaro-Seoane et al., 2017), as well as pulsar timing arrays (Xin et al., 2020).

Candidate binary SMBHs have been identified in active galactic nuclei (AGN) through a variety of methods, including unusual jet morphologies (e.g., Lobanov & Roland, 2005; Caproni et al., 2013; Tsai et al., 2013; Kun et al., 2014; Krause et al., 2019), emission line profiles (e.g., Eracleous et al., 2012; Ju et al., 2013; Shen et al., 2013; Liu et al., 2014; Li et al., 2016; Guo et al., 2019), and candidate periodic features in AGN light curves (e.g., Lehto &

---

[1] This Chapter reproduces Saade et al. (2023; arXiv:2304.06144) subject only to formatting changes to adhere to the PhD thesis stylistic requirements.

Valtonen, 1996; Graham et al., 2015a,b; Charisi et al., 2016; Liu et al., 2019; O'Neill et al., 2022; Chen et al., 2020; Liao et al., 2021; Chen et al., 2022). For a recent review of this field, see Bogdanović et al. (2022). Of the candidates identified, the current strongest candidates are OJ 287, which displays periodic flares that are well explained by a model in which a secondary black hole passes through a primary black hole's accretion disk once per decade (Lehto & Valtonen, 1996), and PG 1302-102, which shows some evidence for consistent periodicity in its optical (Graham et al., 2015a), ultraviolet (D'Orazio et al., 2015b; Xin et al., 2020), and mid-infrared light curves (Jun et al., 2015a), as well as in the precession of its radio jet (Qian et al., 2018). In particular, the ratio of the amplitudes in the UV and optical matches expectations under the assumption that the sinusoidal variation is due to relativistic Doppler modulation from binary orbital motion given the UV and optical spectral slopes (D'Orazio et al., 2015b; Xin et al., 2020).

Another potential way to detect binary SMBHs is through X-ray emissions. Since X-rays probe the portion of an AGN closest to the central black hole(s), the presence of a subparsec SMBH binary could potentially have a large imprint on the high-energy emission. Several models have predicted the X-ray emissions of binary SMBH AGN, though they differ in their predictions in part because current simulations are unable to simulate thin disks and thus make ad-hoc approximations about the thermodynamics. Some analyses predict a notch in the X-ray spectrum (e.g. Tang et al., 2018) and/or for the spectral shape of the high-energy continuum to be harder (e.g., Roedig et al., 2014; Ryan & MacFadyen, 2017; Tang et al., 2018; Krolik et al., 2019), while others predict more modest differences, if any (e.g., d'Ascoli et al., 2018; Gutiérrez et al., 2022). Many models predict increased X-ray luminosity as well (e.g., 10x higher in the 10-100 keV band, Farris et al., 2015a).

In our previous paper, Saade et al. (2020) (henceforth referred to as SA20), we observed 7 AGN identified as potentially periodic by Graham et al. (2015b) from the Catalina Real-Time Transient Survey (CRTS; Drake et al., 2009). We used *Chandra* observations to test theoretical models of accreting binary SMBHs and potentially determine whether the AGN were binary SMBHs. We did not find any significant differences between the spectra of these AGN and the spectra of single-SMBH AGN. While there are many possible reasons for this result (discussed at length in SA20), one potential reason is that the differences in X-rays could be modest in the soft X-rays, but more dramatic in the harder X-rays, as predicted by some calculations (e.g. Roedig et al., 2014).

Three of the AGN in Saade et al. (2020) have *NuSTAR* (Harrison et al., 2013) observations through a combination of our own proposal and archival data. In this work we analyze these *NuSTAR* spectra to see if there is any evidence that the predicted differences between binary SMBH AGN and single SMBH AGN show up in the hard X-rays.

4.2 Observations and Data Analysis

The X-ray observations used in this paper are listed in Table 4.1. We use all available *NuSTAR* data for the objects in the SA20 sample. This amounted to three objects: 2MASXi J0729087+400836, PG 1302-102, and FBQS J163302.6+234928. 2MASXi J0729087+400836 and PG 1302-102 have *NuSTAR* data from our Cycle 6 proposal (P.I. M. Saade). The FBQS J163302.6+234928 *NuSTAR* observations were obtained from the archive (P.I. E. Kammoun).

For soft X-ray data, we preferentially used data taken simultaneously with *NuSTAR*. For PG 1302-102, this was *Swift* (Gehrels et al., 2004) data; for FBQS J163302.6+234928, this was *XMM-Newton* (Jansen et al., 2001) data. 2MASXi J0729087+400836 did not have any simultaneous observations, so we re-use the *Chandra* (Weisskopf et al., 2002) observation reported in SA20. All the high-energy observations were background-subtracted and fit in XSPEC (Arnaud, 1996, version 12.12.1). The spectra were grouped by a minimum of one count per bin. In this situation, XSPEC uses a modified version of the C-statistic known as the W-statistic. Below we describe the specific details of each observatory's data analysis.

4.2.1 *NuSTAR*

We reduced and extracted the *NuSTAR* data with HEASOFT (version 6.30.1), NuSTARDAS (version 2.1.2), and *NuSTAR* CALDB (version 20220525). We used $40''$ radius circular regions centered on each source for the extraction, and $100''$ radius background regions. In fitting the spectra, we fixed the cross-normalization constant of FPMA to 1.0, and that of FPMB to 1.04, where the latter is based on calibration observations of the bright source 3C 273 reported in Madsen et al. (2015). For FBQS J163302.6+234928, we did this only for the first *NuSTAR* observation; the second observation's cross-normalization constants were left to vary freely. The *NuSTAR* background dominates the source above 30 keV, so we used the 3-30 keV range for the spectral fitting.

4.2.2 *Swift*

The HEASARC archive includes a *Swift* observation contemporaneous with the *NuSTAR* observation of PG 1302-102. We reduced and extracted the XRT data with HEASOFT (version 6.30.1), the *Swift* XRT CALDB (version 20210915), and the *Swift* XRT Data Analysis Software (version 3.7.0). We used a circular source region of $25''$ radius and a circular background region of $50''$ radius. We used the 0.3-10 keV range for the spectral fitting.

4.2.3 *XMM-Newton*

FBQS J163302.6+234928 has a simultaneous *XMM-Newton* observation for both *NuSTAR* observations. We extracted the data using the *XMM-Newton* Scientific Analysis Software (version 20.0.0). For all *XMM-Newton* cameras we used circular source regions $50''$ in radius. These were centered on the quasar in the MOS cameras, but were offset slightly in the PN camera to avoid chip edges. We used a circular background region $80''$ in radius for the MOS cameras and $60''$ in radius for the PN camera. The latter was smaller in order to avoid chip edges and extra sources.

For all *XMM-Newton* observations, we filtered out times with high background, defined as when the count rate in the 10–12 keV range was $> 0.4\,\mathrm{cts\,s^{-1}}$ for the PN and $> 0.35\,\mathrm{cts\,s^{-1}}$ for the MOS cameras. The first observation suffered from a large background flare, with count rates of up to 18 cts $\mathrm{s^{-1}}$ in the PN camera, and 7–8 cts $\mathrm{s^{-1}}$ in the MOS cameras. The flare continued for longer in the MOS cameras, such that while only 42% of the PN exposure time was lost due to background flaring, 78% of the MOS1 exposure time and 85% of the MOS2 exposure time was lost to background flaring. In addition to background filtering, a known flare star (2MASS J16330429+2349464) is present within $30''$ of the quasar in the PN image. It was not visible in the MOS images due to most of the MOS time being lost to background flares. We removed additional time from the PN image to filter out the star's flares, corresponding to time intervals with a count rate $> 0.15\,\mathrm{cts\,s^{-1}}$. In total, 45% of the PN exposure time was lost to background flares and activity by the flare star.

The second observation had discrete background flares instead of the overall high levels of the first observation, resulting in little time lost to background flares. As such, the flare star appeared in all three cameras even after background flare filtering. To avoid activity from the flare star, we filtered out times with $> 0.15\,\mathrm{cts\,s^{-1}}$ for the PN camera and $> 0.08\,\mathrm{cts\,s^{-1}}$ for the MOS cameras. Combining the filtering for both background and stellar flares, 31% of the PN exposure time and 3% of the MOS1 and MOS2 exposure times were lost.

This did not completely eliminate the star from the filtered *XMM-Newton* images. We therefore only fit the combined spectrum over the observed 2-30 keV range, with the exception of when we calculated the rest frame 2-10 keV spectral index, which necessitated using observed frame 1.10-5.49 keV data. The X-ray spectra of flare stars are substantially softer than that of AGN, and are typically fit with a thermal plasma with a temperature below 2 keV (e.g., Gorenstein & Tucker, 1976; Robrade & Schmitt, 2005; Pandey & Singh, 2008). We therefore expect that the AGN dominates over the star in the *NuSTAR* bands, and we did not apply any filtering to the *NuSTAR* data. As an additional check, we extracted background-subtracted 3-8 keV light curves of FBQS J163302.6+234928 from both *NuSTAR* observations and confirmed that no flares were evident.

4.2.4 *Chandra*

For 2MASXi J0729087+400836, there were no soft X-ray observations contemporaneous with the *NuSTAR* observation, so we used the earlier *Chandra* data reported in SA20. We used the spectrum from that paper, grouped to have a minimum of 1 count per bin. Details on the *Chandra* data analysis are in SA20.

Table 4.1. Target sample and observation details.

Target	Observatory	ObsID	Date	Net Exposure Time (ks)	Net Count Rate (cts ks^{-1})
2MASXi J0729087+400836	*Chandra*	19528	2017-04-28	7.6	267.5
	NuSTAR	60601029002	2021-05-16	21.5/21.3	44.2/40.0
PG 1302-102	*Swift*	00089146001	2021-06-08	1.7	144.7
	NuSTAR	60601030002	2021-06-08	36.5/36.3	68.1/65.7
FBQS J163302.6+234928	*XMM-Newton*	0870910101	2020-08-08	56.8/5.8/3.6	141.0/31.21/47.55
		0870910301	2021-01-31	71.9/103.2/103.5	152.1/56.7/55.6
	NuSTAR	60601012002	2020-08-09	102.2/101.2	21.2/19.5
		60601012004	2021-01-31	101.1/100.0	22.9/20.8

Note. — *NuSTAR* net exposure times and net count rates are written as FPMA/FPMB. *XMM-Newton* net exposure times and net count rates are written as PN/MOS1/MOS2.

4.3 X-ray Properties

The unfolded spectra of the AGN are shown in Figures 4.1, 4.2, and 4.3. We fit all three with a CONSTANT*TBABS*ZPHABS*POWERLAW model, with the CONSTANT term representing the cross-normalization constant between multiple observations, TBABS representing photoelectric absorption within our Galaxy, ZPHABS representing photoelectric absorption in the host galaxy, and the POWERLAW model representing the intrinsic spectrum of the black hole corona, which radiates approximately as a powerlaw spectrum. Including ZPHABS did not improve the fit for PG 1302-102 over a CONSTANT*TBABS*POWERLAW model, so the ZPHABS component was dropped for that source. The C-stat/d.o.f. values for each fit are tabulated in Table 2 and the fits are plotted over the unfolded spectra in the figures. The sources are well-fit by the model, with C-stat/d.o.f. values ≈1, though 2MASXi J0729087+400836 shows some soft excess above the powerlaw component, a feature found in most AGN spectra below about 2 keV (Ballantyne & Xiang, 2020). The physical origin of this soft excess is not clear but has been proposed to be smeared reflected emission lines (Crummy et al., 2006; Walton et al., 2013) or a warm ($\sim 0.1\,\mathrm{keV}$) component of the corona (Mehdipour et al., 2011; Done et al., 2012). FBQS J163302.6+234928 shows $\sim 10\% - 20\%$ variability between its two *NuSTAR* observations.

From the XSPEC models, we measure the spectral index, Γ, for the entire range of energies fit, as well as specifically for the rest frame 2-10 keV energy band, Γ_{2-10}. These are presented in Table 2. Taking into account the *NuSTAR* data, the values are softer than measured in the *Chandra* data alone in SA20. However there is overlap between the 90% confidence intervals for Γ with and without *NuSTAR* data for all three sources, so the measurements are consistent. The spectral index values all lie within the typical 1.5-2.0 range of AGN (Nandra & Pounds, 1994; Shemmer et al., 2008; Brightman et al., 2013).

We first compare the indices of our sample to the 0.3-10 keV spectral indices of the BAT AGN Spectroscopic Survey (BASS) sample (Table 15 in Ricci et al., 2017a). This sample includes

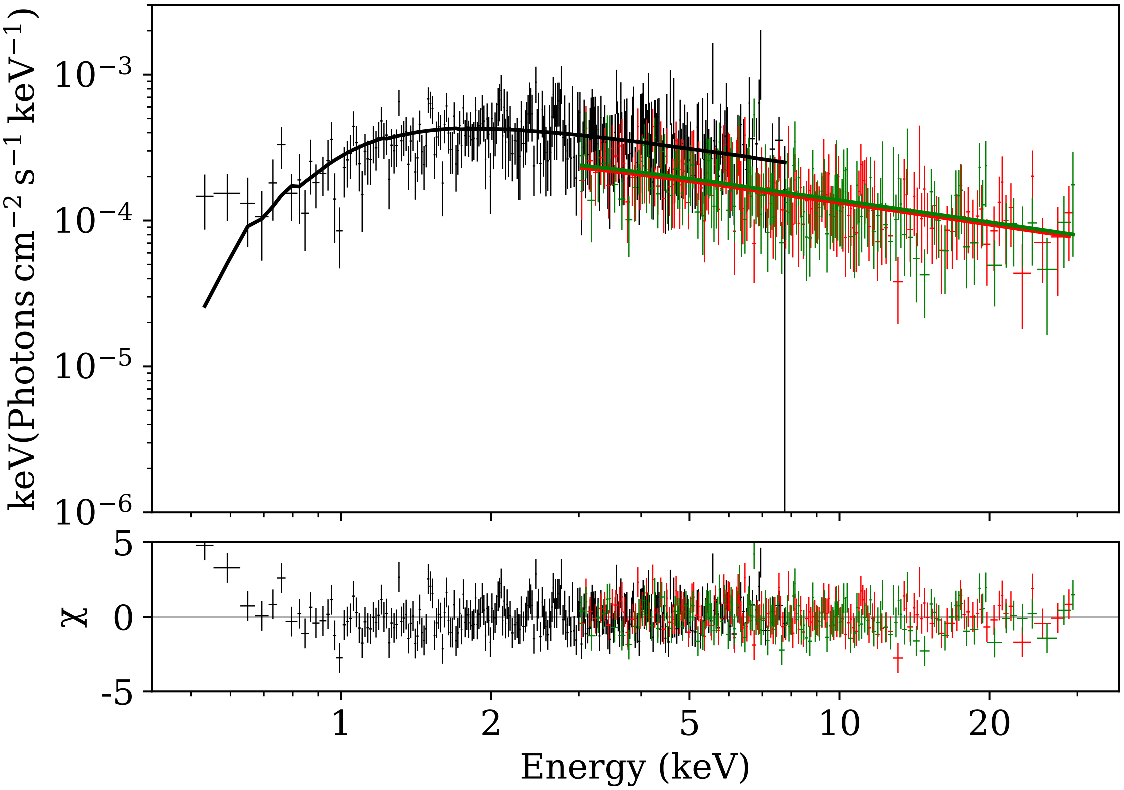

Figure 4.1 Unfolded spectrum and best-fit models for 2MASXi J0729087+400836. Black corresponds to *Chandra* data; red and green correspond to *NuSTAR* FPMA and FPMB data.

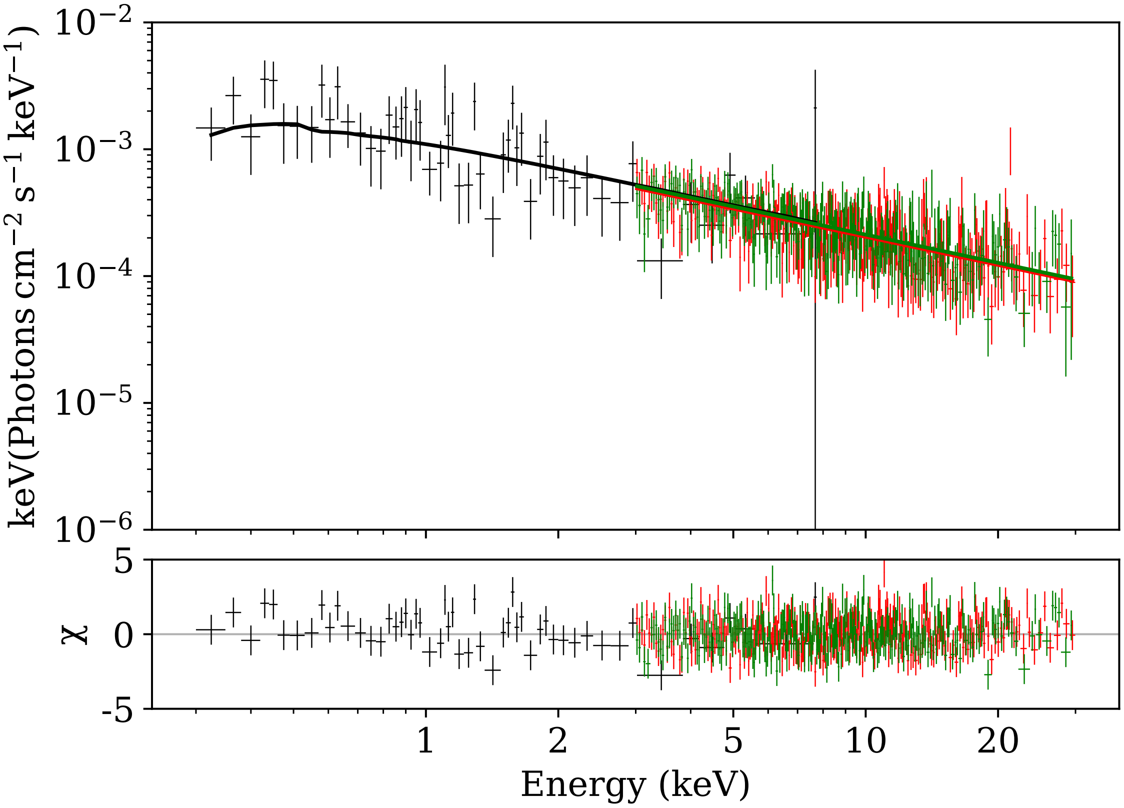

Figure 4.2 Unfolded spectrum and best-fit models for PG 1302-102. Black corresponds to *Swift* XRT data; red and green correspond to *NuSTAR* FPMA and FPMB data.

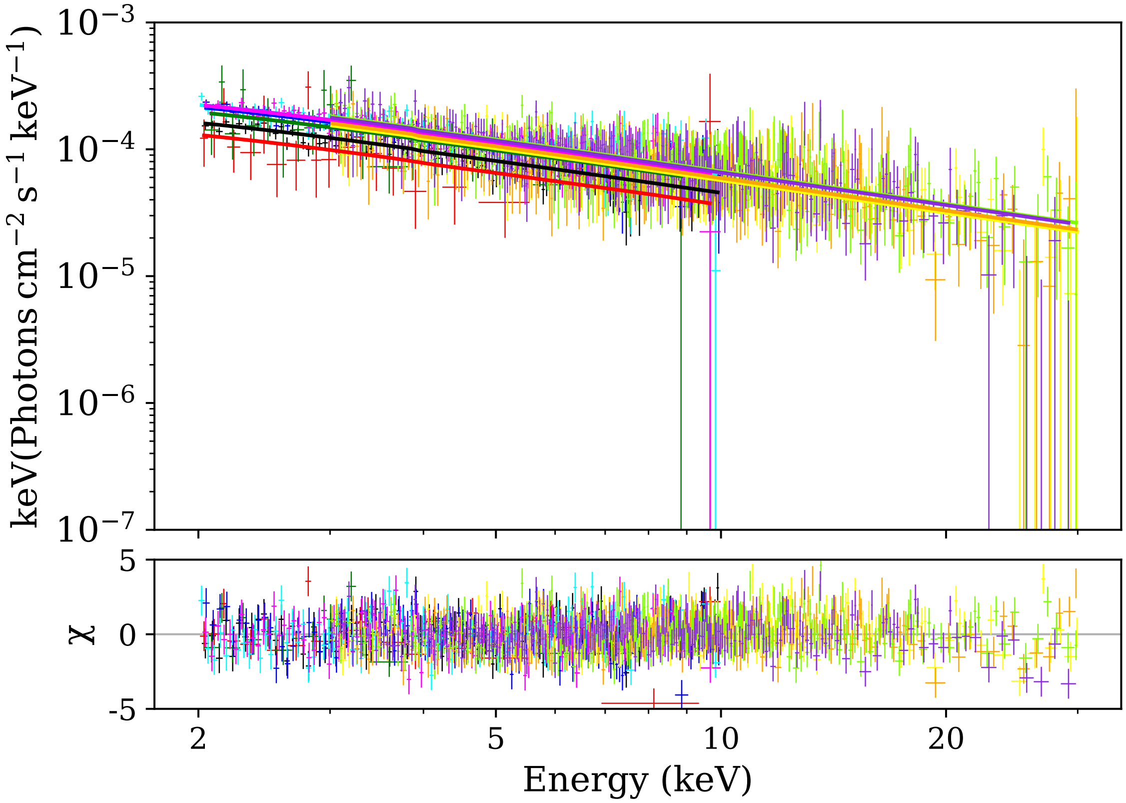

Figure 4.3 Unfolded spectrum and best-fit models for FBQS J163302.6+234928. Black, red and green correspond to PN, MOS1, and MOS2 data from *XMM-Newton* observation 0870910101. Blue, cyan, and magenta correspond to PN, MOS1 and MOS2 data from *XMM-Newton* observation 0870910301. Yellow and orange correspond to FPMA and FPMB data from *NuSTAR* observation 60601012002. Chartreuse and purple correspond to FPMA and FPMB data from *NuSTAR* observation 60601012004.

838 AGN at redshift $0.003 \leq z \leq 3.6$, with 2-10 keV luminosities $38.4 \leq \log(L_{2-10}/\mathrm{erg\,s^{-1}}) \leq 47.6$. The BASS sample properties envelope the three targets discussed here. The Γ_{2-10} values for our sample are compared to the BASS $\Gamma_{0.3-10}$ values in the left panel of Figure 4.4; the difference in energy range should have negligible effect on the intrinsic spectral index values. We performed a Kolmogorov-Smirnoff test comparing the three candidate binary SMBH sources grouped together as a distribution against the BASS sample. The resulting p-value of 0.958 is too high to reject the null hypothesis that our three candidate binary SMBH AGN are drawn from the same distribution as the BASS sample. This, together with their clear placement near the mean of the histogram, indicates they are indistinguishable from the larger AGN population. This is the same conclusion we came to in SA20 for a larger sample with only soft X-ray data.

We then investigated how the sample compares to the general AGN population when including *NuSTAR* data above 10 keV. For this comparison we used the sample of 195 unobscured AGN in Kamraj et al. (2022). These AGN are a subset of the BASS sample and have *NuSTAR* observations in addition to *Swift* XRT and *XMM-Newton* observations, with derived spectral indices measured over the entire energy range of their observations. The redshifts for this sample range over $0.002 \leq z \leq 0.197$, and the Eddington ratios range over $0.003 \leq L/L_{\mathrm{Edd}} \leq 2.0$. Though two of the candidate binary SMBH AGN are outside this redshift range, their Eddington ratios are consistent with the larger sample (Table 2.2). Kamraj et al. (2022) fit their sample with a CONSTANT*TBABS*ZPHABS*CUTOFFPL model, where CUTOFFPL models a powerlaw with an exponential cutoff. We fit our data with the same model over the full range of energies and measured the spectral index, referred to as Γ_{ABS} to distinguish it from the soft X-ray spectral indices discussed above. The resultant values are presented in Table 2.2. The Γ_{ABS} values for our sample are plotted over a histogram of the Kamraj et al. (2022) Γ_{ABS} values in the right panel of Figure 4.4. We performed a Kolmogorov-Smirnoff test to compare our measured spectral indices to the Kamraj et al. (2022) sample. The resulting p-value of 0.889 is too high to reject the null

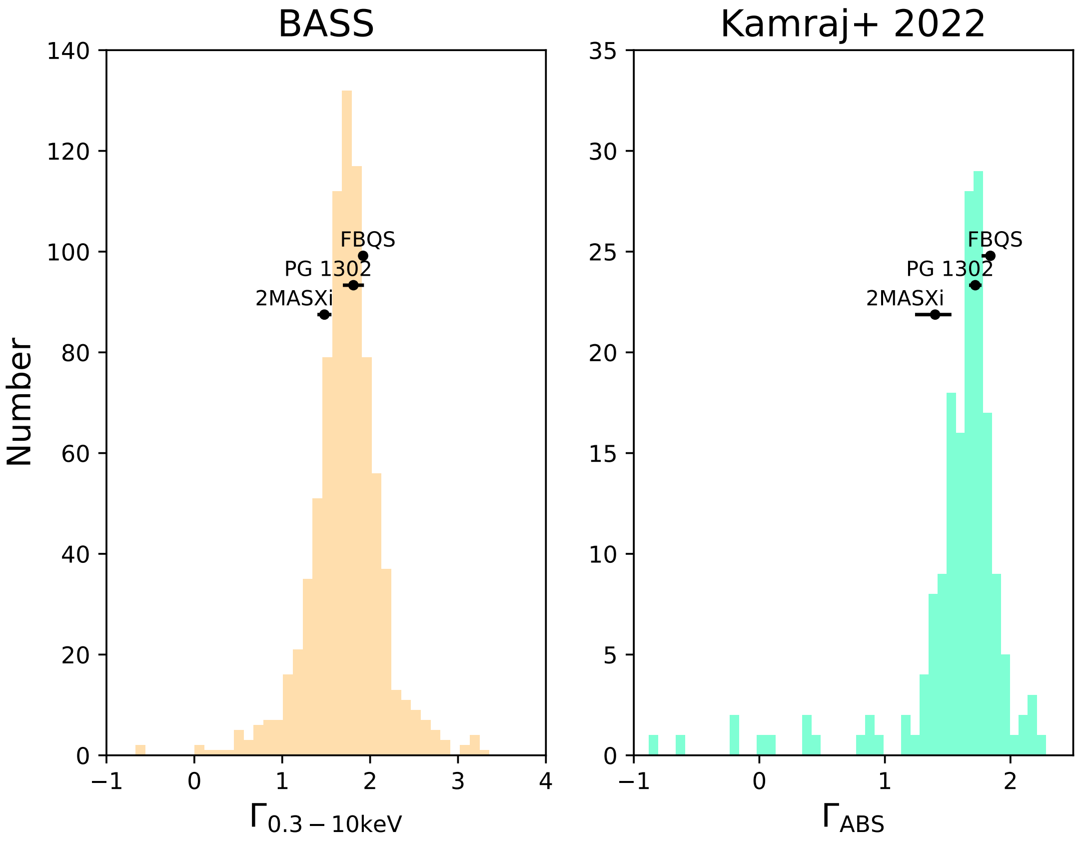

Figure 4.4 Spectral indices for the three AGN in our sample compared to histograms of the $\Gamma_{0.3-10}$ values from the BASS sample (Ricci et al., 2017a) (left panel) and the $\Gamma_{\rm ABS}$ values from Kamraj et al. (2022) (right panel). In both cases, the candidate binary SMBH AGN are indistinguishable from the larger general AGN populations.

hypothesis that our three AGN and the Kamraj et al. (2022) AGN are drawn from the same distribution. Once again, as is made clear by the histogram in Figure 4.4, the spectral indices of the candidate binary SMBH AGN are not distinguishable from the general AGN population.

Some models predict a notch in the X-ray spectra of binary SMBH AGN (e.g., Roedig et al., 2014). At energies below ~ 1, keV, emission from the viscously heated circumbinary disc dominates, while the higher energy spectrum is dominated by shock-heated gas in the minidiscs around each SMBH, streams, and near the cavity wall at the inner edge of the circumbinary disk. This could lead to a small depression at a few keV (e.g., Tang et al., 2018). However, as seen in the unfolded X-ray spectra presented in Figures 1-3, there is no evidence of notches in the high-energy spectra of any of the sources. This could be due to the notch signature being too subtle for the signal-to-noise ratio of our data, or due to the sources not in fact being binary SMBH AGN. Alternatively, more recent theoretical work predicts the notch to be at much lower energies, in the UV/optical/IR range (Krolik et al., 2019).

We also tested fits to these AGN with two powerlaws, under the assumption that if two black holes were present, their coronae would not necessarily have the same spectral indices. As expected for the additional degree of freedom, we did get improvements in the C-stat/d.o.f, but the second powerlaw invariably became extremely soft, much steeper than the expectations of coronal emission. This suggested the additional parameter was picking up a soft excess component of the spectrum, rather than a second corona. We added a third powerlaw to the fits, but they did not improve C-stat/d.o.f. We therefore do not find any evidence of two coronae in these data.

4.4 Discussion

There is no evidence that these spectra are harder than typical AGN spectra, as predicted by some models. In particular, Roedig et al. (2014) predict that binary SMBH systems will have excess shock-heated gas with temperature on the order ~ 100 keV for a separation of $\sim 100\, r_g$, where the gravitational radius $r_g \equiv GM/c^2$, G is the gravitational constant, M is the total binary mass, and c is the speed of light. This leads to a thermal spectrum that differs from the standard coronal powerlaw. Following Foord et al. (2017), we can estimate the temperature of the shocked gas of the binary SMBH using the proportionality from Roedig et al. (2014): $T_{\rm sh} \propto (a/100\, r_g)^{-1}(1+q^{0.7})^{-1}$, where a is the binary separation and q is the binary mass ratio. Using values for a and q from SA20, we find rest frame shocked gas temperatures of 3.4 keV for 2MASXi J0729087+400836, 12.0 keV for PG 1302-102, and 108.5 keV for FBQS J163302.6+234928, corresponding to energies of 3.2 keV, 9.37 keV, and 59.63 keV in the observed frame. This implies we would expect a substantially softer spectrum in 2MASXi J0729087+400836, and substantially harder spectra in PG 1302-102 and FBQS J163302.6+234928. However, §3 shows that none of the X-ray spectra show strong deviations from the larger AGN population at either soft or hard energies.

The predicted binary separations for these sources (listed in Table 3 of SA20) are all greater than $100\,r_g$, other than FBQS J163302.6+234928. Enhancements to the X-ray emission due to a binary SMBH are predicted to decrease with increasing binary separation. For example, Roedig et al. (2014) predict that separations greater than 100 r_g will have spectra indistinguishable from single SMBHs. Therefore it is possible that 2MASXi J0729087+400836 and PG 1302-102 have binary separations too wide to enhance their hard X-ray emissions to a level that is detectably distinct from single SMBH AGN. Krolik et al. (2019), however, claim that enhanced hard X-ray emission should be detectable for binary separations up to 1000 r_g, a range which PG 1302-102 falls under. Our data therefore suggest that these predictions are incorrect, if PG 1302-102 is indeed a binary SMBH with the reported orbital separation.

We have shown that broadband X-ray spectra, spanning the soft X-rays observed by *Chandra*, *Swift*, and *XMM-Newton* to the hard X-rays observed by *NuSTAR*, do not exhibit any evidence that the three candidate binary SBMH AGN studied here are different from the typical (single) AGN population. Neither the soft nor broadband X-ray spectral indices are distinct from larger AGN populations, despite some theoretical predictions that enhanced X-ray emission should be expected. We also find no evidence for a notch in their X-ray spectra, nor do we find evidence for multiple X-ray coronae. There are multiple potential explanations for this non-result. First, the signatures of a binary SMBH might be too subtle given the quality of our data. In that case, deeper observations or future, more sensitive facilities might detect indications of binarity missed in the current data. Second, as emphasized in SA20, theoretical predictions of high-energy emission from binary SMBH AGN are relatively immature as a field, with models still highly idealized. In that case, observations such as these test current models and will help direct future theoretical modeling.

Finally, it is possible the three AGN investigated in this paper are not in fact binary SMBHs. Indeed, we know that not all binary SMBH candidates can truly be binaries, since this would overpredict the gravitational wave background seen by pulsar timing arrays (Sesana et al., 2018). The literature is rife with claimed periodicity in AGN light curves, though follow-up analyses find many claims to be statistically lacking (e.g., Vaughan et al., 2016; Barth & Stern, 2018). Recent work shows that PG 1302-102's variations cannot be explained by random noise, and there is very strong support for periodicity or, at least, quasiperiodicity (Zhu & Thrane, 2020), where the latter is an expected consequence of SMBH binaries (Bowen et al., 2019; Combi et al., 2022). We also note that even if the periodicity (or quasiperiodicity) is real, it might not be due to a binary SMBH system. Similar to the mechanism that causes quasi-periodic oscillations (QPOs) in systems with a stellar mass compact object (e.g., Zhu & Thrane, 2020), periodicity could potentially be due to precession of the accretion disk or jet (e.g., Dotti et al., 2022). However, as noted by Graham et al. (2015b), the timescale for a warped accretion disk (such that it would undergo precession) to remain before self-gravity undoes the warp is much shorter than the typical AGN lifetime. It is therefore unlikely that precession due to a warped accretion disk explains the behavior of the three AGN studied here.

Ongoing and future synoptic surveys will improve and extend the light curves for candidate periodic AGN, testing their unusual variability with increasing statistical accuracy. Some current candidates will likely fall, while new candidates will be identified. X-ray emission, coming from the innermost regions around the SMBH(s), should, in principle, provide a strong test if observed periodicity is due to binarity. Our results, emphasizing soft X-ray data in SA20 and broadband X-ray data here, do not find evidence for unusual X-ray properties for some of the strongest and X-ray brightest binary SMBH candidates currently known. However, we are still in the early stages of this field, both observationally and theoretically. The non-detections reported here can help motivate future, more sensitive observations (and observatories), while simultaneously helping direct theoretical work.

Table 4.2. Properties and X-ray model parameters of the sample.

Target	z	L/L_{Edd}[a]	Γ[b]	Γ_{2-10}[c]	$\log(L_{2-10})$[d]	C-stat/d.o.f.	Γ_{ABS}[e]
2MASXi J0729087+400836	0.074	0.18	1.51 ± 0.07	1.48 ± 0.08	43.52 ± 0.02	1038.16/1145	$1.40^{+0.13}_{-0.16}$
PG 1302-102	0.278	0.30	1.74 ± 0.05	1.81 ± 0.12	45.02 ± 0.02	1101.91/1123	1.72 ± 0.05
FBQS J163302.6+234928	0.821	0.12	1.82 ± 0.04	1.92 ± 0.02	45.51 ± 0.02	2760.64/2630	$1.84^{+0.01}_{-0.07}$

Note. — d.o.f. stands for 'degrees of freedom'. Error bars represent 90% confidence intervals.

[a] From Table 3 of SA20.

[b] Measured over full range of energies for each source.

[c] Measured using rest-frame 2-10 keV band.

[d] Measured using model flux in rest-frame 2-10 keV band, in units of erg s^{-1}.

[e] Gamma measured from CONSTANT*TBABS*ZPHABS*CUTOFFPL model.

CHAPTER 5

Conclusion

While there is much evidence for SMBH-galaxy coevolution, the details still are uncertain. With this thesis we have presented studies of candidate binary SMBHs and recently deactivated AGN. These studies contribute to the vast body of research that has gone into understanding how SMBHs grow and evolve together with their host galaxies.

In Chapters 2 and 4, we found that the X-ray spectra of candidate binary SMBHs were not distinctly different from those of the general AGN population, throughout the 0.5-30 keV energy range. As mentioned in those chapters, this could be potential evidence that theoretical models predicting dramatic departures from typical AGN spectra are incorrect, or that the AGN in question are not binary SMBHs. However, the result is not fully conclusive. In particular, if the predicted excess X-ray emission occurs at very high energies (e.g. 100-500 keV, as seen in Roedig et al., 2014; Krolik et al., 2019) then we would not expect to see many differences in the parts of the X-ray spectrum observable with *NuSTAR*. Fortunately, future missions capable of observing this energy range are in development, such as the Small Explorer-class *Compton Spectrometer and Imager* (*COSI*; Tomsick & COSI Collaboration, 2022) and the Probe-class *High Energy X-ray Probe* (*HEX-P*; Madsen et al., 2018). The experiment of searching for excess X-ray emission in candidate binary SMBHs is likely to be done again using these missions. Our research therefore motivates future observations, in addition to theory development.

In Chapter 3 we reported an AGN that likely deactivated on timescales of decades to hundreds of years. Given our small sample size, this suggests that recently deactivated AGN are more common than thought, and that they might be turning off on timescales faster than previously thought. Many new time domain surveys are coming online, such as the Rubin Observatory's Legacy Survey of Space and Time (LSST), which will survey tens of millions of AGN (Brandt, 2022). With these large numbers, more recently deactivated AGN are sure to be identified, and on timescales shorter than that probed in our paper. Existing telescopes such as the *Wide Field Infrared Explorer* (*WISE* Wright et al., 2010) and its current NeoWISE Reactivation survey (Mainzer et al., 2014) could be leveraged to search for the very beginnings of fading after an AGN deactivates, and we are in fact working on a project about this right now. The successor to *WISE*, *NEO Surveyor* could also be used in a similar manner in the future to detect the beginnings of torus fading in AGN. eROSITA (Merloni et al., 2012), if it is taken out of safe mode, would be able to detect newly deactivated AGN. These time domain studies could also be used to identify many more binary SMBH candidates, which could then be tested using X-ray observations.

Overall this is an exciting time to be working on binary SMBHs and AGN duty cycles. The variability of AGN will be scrutinized like never before, and this will undoubtedly lead to many new discoveries.

Bibliography

Ai, Y., Dou, L., Yang, C., et al. 2020, ApJ, 890, L29

Akylas, A., & Georgantopoulos, I. 2009, A&A, 500, 999

Alexander, D. M., & Hickox, R. C. 2012, New A Rev., 56, 93

Alexander, D. M., Bauer, F. E., Brandt, W. N., et al. 2003, AJ, 126, 539

Alexander, P., & Leahy, J. P. 1987, MNRAS, 225, 1

Alonso-Herrero, A., Ward, M. J., Aragon-Salamanca, A., & Zamorano, J. 1999, MNRAS, 302, 561

Alonso-Herrero, A., Poulton, R., Roche, P. F., et al. 2016, MNRAS, 463, 2405

Amaro-Seoane, P., Audley, H., Babak, S., et al. 2017, arXiv e-prints, arXiv:1702.00786

Anglés-Alcázar, D., Faucher-Giguère, C.-A., Quataert, E., et al. 2017, MNRAS, 472, L109

Anglés-Alcázar, D., Quataert, E., Hopkins, P. F., et al. 2021, ApJ, 917, 53

Annuar, A., Gandhi, P., Alexander, D. M., et al. 2015, ApJ, 815, 36

Armitage, P. J., & Natarajan, P. 2002, ApJ, 567, L9

Arnaud, K. A. 1996, in Astronomical Society of the Pacific Conference Series, Vol. 101, Astronomical Data Analysis Software and Systems V, ed. G. H. Jacoby & J. Barnes, 17

Artymowicz, P., & Lubow, S. H. 1994, ApJ, 421, 651

Asmus, D., Gandhi, P., Hönig, S. F., Smette, A., & Duschl, W. J. 2015, MNRAS, 454, 766

Asmus, D., Hönig, S. F., & Gandhi, P. 2016, ApJ, 822, 109

Asmus, D., Hönig, S. F., Gandhi, P., Smette, A., & Duschl, W. J. 2014, MNRAS, 439, 1648

Audibert, A., Riffel, R., Sales, D. A., Pastoriza, M. G., & Ruschel-Dutra, D. 2017, MNRAS, 464, 2139

Bae, H.-J., Woo, J.-H., Karouzos, M., et al. 2017, ApJ, 837, 91

Baldwin, J. A., Phillips, M. M., & Terlevich, R. 1981, PASP, 93, 5

Ballantyne, D. R., & Xiang, X. 2020, MNRAS, 496, 4255

Balmaverde, B., & Capetti, A. 2014, A&A, 563, A119

Baloković, M., Brightman, M., Harrison, F. A., et al. 2018, ApJ, 854, 42

Bardeen, J. M., & Petterson, J. A. 1975, ApJ, 195, L65

Barnes, D. G., & Webster, R. L. 2001, MNRAS, 324, 859

Barth, A. J., & Stern, D. 2018, ApJ, 859, 10

Barth, A. J., Bennert, V. N., Canalizo, G., et al. 2015, ApJS, 217, 26

Baruteau, C., Ramirez-Ruiz, E., & Masset, F. 2012, MNRAS, 423, L65

Begelman, M. C., Blandford, R. D., & Rees, M. J. 1980, Nature, 287, 307

Benke, P., Frey, S., Gabanyi, K., et al. 2018, in 14th European VLBI Network Symposium & Users Meeting (EVN 2018), 98

Bennert, N., Falcke, H., Schulz, H., Wilson, A. S., & Wills, B. J. 2002, ApJ, 574, L105

Bennert, N., Jungwiert, B., Komossa, S., Haas, M., & Chini, R. 2006, A&A, 456, 953

Berczik, P., Merritt, D., Spurzem, R., & Bischof, H.-P. 2006, ApJ, 642, L21

Berney, S., Koss, M., Trakhtenbrot, B., et al. 2015, MNRAS, 454, 3622

Bianchi, L., Shiao, B., & Thilker, D. 2017, ApJS, 230, 24

Bianchi, S., Chiaberge, M., Piconcelli, E., Guainazzi, M., & Matt, G. 2008a, MNRAS, 386, 105

Bianchi, S., Corral, A., Panessa, F., et al. 2008b, MNRAS, 385, 195

Bianchi, S., Guainazzi, M., & Chiaberge, M. 2006, A&A, 448, 499

Bieri, R., Dubois, Y., Silk, J., Mamon, G. A., & Gaibler, V. 2016, MNRAS, 455, 4166

Blecha, L., Snyder, G. F., Satyapal, S., & Ellison, S. L. 2018, MNRAS, 478, 3056

Bogdanović, T., Miller, M. C., & Blecha, L. 2022, Living Reviews in Relativity, 25, 3

Boorman, P. G., Gandhi, P., Alexander, D. M., et al. 2016, ApJ, 833, 245

Bowen, D. B., Campanelli, M., Krolik, J. H., Mewes, V., & Noble, S. C. 2017, ApJ, 838, 42

Bowen, D. B., Mewes, V., Noble, S. C., et al. 2019, ApJ, 879, 76

Braatz, J., Greenhill, L., Moran, J., Wilson, A., & Herrnstein, J. 1997, in American Astronomical Society Meeting Abstracts, Vol. 191, American Astronomical Society Meeting Abstracts, 104.02

Braatz, J. A., Henkel, C., Greenhill, L. J., Moran, J. M., & Wilson, A. S. 2004, ApJ, 617, L29

Brandt, W. 2022, in 44th COSPAR Scientific Assembly. Held 16-24 July, Vol. 44, 2301

Brenneman, L. W., & Reynolds, C. S. 2006, ApJ, 652, 1028

Brightman, M., & Nandra, K. 2008, MNRAS, 390, 1241

Brightman, M., & Nandra, K. 2011a, MNRAS, 413, 1206

Brightman, M., & Nandra, K. 2011b, MNRAS, 414, 3084

Brightman, M., Silverman, J. D., Mainieri, V., et al. 2013, MNRAS, 433, 2485

Brightman, M., Baloković, M., Stern, D., et al. 2015, ApJ, 805, 41

Brum, C., Riffel, R. A., Storchi-Bergmann, T., et al. 2017, MNRAS, 469, 3405

Buchanan, C. L., Gallimore, J. F., O'Dea, C. P., et al. 2006, AJ, 132, 401

Burlon, D., Ajello, M., Greiner, J., et al. 2011, ApJ, 728, 58

Burtscher, L., Meisenheimer, K., Tristram, K. R. W., et al. 2013, A&A, 558, A149

Buta, R. J. 2017, MNRAS, 471, 4027

Cappi, M., Panessa, F., Bassani, L., et al. 2006, A&A, 446, 459

Caproni, A., Abraham, Z., & Monteiro, H. 2013, MNRAS, 428, 280

Carrillo, R., Masegosa, J., Dultzin-Hacyan, D., & Ordoñez, R. 1999, Rev. Mexicana Astron. Astrofis., 35, 187

Cazzoli, S., Márquez, I., Masegosa, J., et al. 2018, MNRAS, 480, 1106

Chang, P., Strubbe, L. E., Menou, K., & Quataert, E. 2010, MNRAS, 407, 2007

Charisi, M., Bartos, I., Haiman, Z., et al. 2016, MNRAS, 463, 2145

Chatzichristou, E. T., & Vanderriest, C. 1995, A&A, 298, 343

Chen, Y.-C., Liu, X., Liao, W.-T., et al. 2020, MNRAS, 499, 2245

Chen, Y.-J., Zhai, S., Liu, J.-R., et al. 2022, arXiv e-prints, arXiv:2206.11497

Cisternas, M., Jahnke, K., Inskip, K. J., et al. 2011, ApJ, 726, 57

Cisternas, M., Gadotti, D. A., Knapen, J. H., et al. 2013, ApJ, 776, 50

Combi, L., Lopez Armengol, F. G., Campanelli, M., et al. 2022, ApJ, 928, 187

Comerford, J. M., Gerke, B. F., Stern, D., et al. 2012, ApJ, 753, 42

Comerford, J. M., Pooley, D., Barrows, R. S., et al. 2015, ApJ, 806, 219

Comerford, J. M., Schluns, K., Greene, J. E., & Cool, R. J. 2013, ApJ, 777, 64

Constantin, A., Shields, J. C., Ho, L. C., et al. 2015, ApJ, 814, 149

Cresci, G., Mainieri, V., Brusa, M., et al. 2015, ApJ, 799, 82

Croft, S., van Breugel, W., de Vries, W., et al. 2006, ApJ, 647, 1040

Crummy, J., Fabian, A. C., Gallo, L., & Ross, R. R. 2006, MNRAS, 365, 1067

Dahari, O., & De Robertis, M. M. 1988, ApJS, 67, 249

Dahlem, M., Weaver, K. A., & Heckman, T. M. 1998, ApJS, 118, 401

d'Ascoli, S., Noble, S. C., Bowen, D. B., et al. 2018, ApJ, 865, 140

Dauser, T., Garcia, J., Parker, M. L., Fabian, A. C., & Wilms, J. 2014, MNRAS, 444, L100

Dauser, T., García, J., Walton, D. J., et al. 2016, A&A, 590, A76

Davies, R. L., Schirmer, M., & Turner, J. E. H. 2015, MNRAS, 449, 1731

Dayal, P., Rossi, E. M., Shiralilou, B., et al. 2019, MNRAS, 486, 2336

de La Calle Pérez, I., Longinotti, A. L., Guainazzi, M., et al. 2010, A&A, 524, A50

De Rosa, A., Vignali, C., Bogdanović, T., et al. 2019, New A Rev., 86, 101525

Delvecchio, I., Daddi, E., Aird, J., et al. 2020, ApJ, 892, 17

Deo, R. P., Richards, G. T., Crenshaw, D. M., & Kraemer, S. B. 2009, ApJ, 705, 14

Dey, L., Valtonen, M. J., Gopakumar, A., et al. 2018, ApJ, 866, 11

Di Matteo, T., Springel, V., & Hernquist, L. 2005, Nature, 433, 604

Díaz-Santos, T., Charmandaris, V., Armus, L., et al. 2010, ApJ, 723, 993

Dickey, J. M., & Lockman, F. J. 1990, ARA&A, 28, 215

Done, C., Davis, S. W., Jin, C., Blaes, O., & Ward, M. 2012, MNRAS, 420, 1848

D'Orazio, D. J., & Di Stefano, R. 2018, MNRAS, 474, 2975

D'Orazio, D. J., Haiman, Z., Duffell, P., Farris, B. D., & MacFadyen, A. I. 2015a, MNRAS, 452, 2540

D'Orazio, D. J., Haiman, Z., & MacFadyen, A. 2013, MNRAS, 436, 2997

D'Orazio, D. J., Haiman, Z., & Schiminovich, D. 2015b, Nature, 525, 351

D'Orazio, D. J., & Loeb, A. 2018, ApJ, 863, 185

Dorn-Wallenstein, T., Levesque, E. M., & Ruan, J. J. 2017, ApJ, 850, 86

Dotti, M., Bonetti, M., Rigamonti, F., et al. 2022, arXiv e-prints, arXiv:2205.06275

Drake, A. J., Djorgovski, S. G., Mahabal, A., et al. 2009, ApJ, 696, 870

Dudik, R. P., Satyapal, S., Gliozzi, M., & Sambruna, R. M. 2005, ApJ, 620, 113

Duffell, P. C., D'Orazio, D., Derdzinski, A., et al. 2020, ApJ, 901, 25

Dunn, R. J. H., & Fabian, A. C. 2008, MNRAS, 385, 757

Duras, F., Bongiorno, A., Ricci, F., et al. 2020, A&A, 636, A73

Eracleous, M., Boroson, T. A., Halpern, J. P., & Liu, J. 2012, ApJS, 201, 23

Esparza-Arredondo, D., Osorio-Clavijo, N., González-Martín, O., et al. 2020, ApJ, 905, 29

Fabian, A. C. 2012, ARA&A, 50, 455

Fabian, A. C., Sanders, J. S., Taylor, G. B., et al. 2006, MNRAS, 366, 417

Farris, B. D., Duffell, P., MacFadyen, A. I., & Haiman, Z. 2014, ApJ, 783, 134

Farris, B. D., Duffell, P., MacFadyen, A. I., & Haiman, Z. 2015a, MNRAS, 447, L80

Farris, B. D., Duffell, P., MacFadyen, A. I., & Haiman, Z. 2015b, MNRAS, 446, L36

Ferguson, H. C. 1989, AJ, 98, 367

Fernández-Ontiveros, J. A., Tristram, K. R. W., Hönig, S., Gandhi, P., & Weigelt, G. 2018, A&A, 611, A46

Ferrarese, L., & Merritt, D. 2000, ApJ, 539, L9

Ferruit, P., Wilson, A. S., & Mulchaey, J. 2000, ApJS, 128, 139

Fitzpatrick, E. L. 1999, PASP, 111, 63

Fitzpatrick, E. L., & Massa, D. 1990, ApJS, 72, 163

Foord, A., Gültekin, K., Nevin, R., et al. 2020, ApJ, 892, 29

Foord, A., Gültekin, K., Reynolds, M., et al. 2017, ApJ, 851, 106

Fruscione, A., McDowell, J. C., Allen, G. E., et al. 2006, in Society of Photo-Optical Instrumentation Engineers (SPIE) Conference Series, Vol. 6270, Society of Photo-Optical Instrumentation Engineers (SPIE) Conference Series, ed. D. R. Silva & R. E. Doxsey, 62701V

Fu, H., Myers, A. D., Djorgovski, S. G., et al. 2015, ApJ, 799, 72

Fu, H., Zhang, Z.-Y., Assef, R. J., et al. 2011, ApJ, 740, L44

Gabriel, C., Denby, M., Fyfe, D. J., et al. 2004, in Astronomical Society of the Pacific Conference Series, Vol. 314, Astronomical Data Analysis Software and Systems (ADASS) XIII, ed. F. Ochsenbein, M. G. Allen, & D. Egret, 759

Gaibler, V., Khochfar, S., Krause, M., & Silk, J. 2012, MNRAS, 425, 438

Gallimore, J. F., Elitzur, M., Maiolino, R., et al. 2016, ApJ, 829, L7

Gallo, L. C., Lehmann, I., Pietsch, W., et al. 2006, MNRAS, 365, 688

García, J., Dauser, T., Lohfink, A., et al. 2014, ApJ, 782, 76

García-Burillo, S., Combes, F., Ramos Almeida, C., et al. 2016, ApJ, 823, L12

Gebhardt, K., Kormendy, J., Ho, L. C., et al. 2000, ApJ, 543, L5

Gehrels, N., Chincarini, G., Giommi, P., et al. 2004, ApJ, 611, 1005

George, I. M., & Fabian, A. C. 1991, MNRAS, 249, 352

Gezari, S., Hung, T., Cenko, S. B., et al. 2017, ApJ, 835, 144

Ghosh, H., Pogge, R. W., Mathur, S., Martini, P., & Shields, J. C. 2007, ApJ, 656, 105

Gold, R., Paschalidis, V., Ruiz, M., et al. 2014, Phys. Rev. D, 90, 104030

González Delgado, R. M., Heckman, T., Leitherer, C., et al. 1998, ApJ, 505, 174

González-Martín, O., Masegosa, J., Márquez, I., & Guainazzi, M. 2009a, ApJ, 704, 1570

González-Martín, O., Masegosa, J., Márquez, I., Guainazzi, M., & Jiménez-Bailón, E. 2009b, A&A, 506, 1107

Gorenstein, P., & Tucker, W. H. 1976, ARA&A, 14, 373

Goulding, A. D., Pardo, K., Greene, J. E., et al. 2019, ApJ, 879, L21

Gower, A. C., Gregory, P. C., Unruh, W. G., & Hutchings, J. B. 1982, ApJ, 262, 478

Graham, M. J., Djorgovski, S. G., Stern, D., et al. 2015a, Nature, 518, 74

Graham, M. J., Djorgovski, S. G., Stern, D., et al. 2015b, MNRAS, 453, 1562

Graham, M. J., Ross, N. P., Stern, D., et al. 2020, MNRAS, 491, 4925

Grier, C. J., Mathur, S., Ghosh, H., & Ferrarese, L. 2011, ApJ, 731, 60

Gross, E., & Vitells, O. 2010, European Physical Journal C, 70, 525

Guainazzi, M., Fabian, A. C., Iwasawa, K., Matt, G., & Fiore, F. 2005a, MNRAS, 356, 295

Guainazzi, M., Matt, G., & Perola, G. C. 2005b, A&A, 444, 119

Gualandris, A., Read, J. I., Dehnen, W., & Bortolas, E. 2017, MNRAS, 464, 2301

Guo, H., & Gu, M. 2014, ApJ, 792, 33

Guo, H., Liu, X., Shen, Y., et al. 2019, MNRAS, 482, 3288

Guo, H., Liu, X., Zafar, T., & Liao, W.-T. 2020, MNRAS, 492, 2910

Gupta, K. K., Ricci, C., Tortosa, A., et al. 2021, MNRAS, 504, 428

Gutiérrez, E. M., Combi, L., Noble, S. C., et al. 2022, ApJ, 928, 137

Haiman, Z. 2017, Phys. Rev. D, 96, 023004

Harrison, F. A., Craig, W. W., Christensen, F. E., et al. 2013, ApJ, 770, 103

Harwood, J. J., Hardcastle, M. J., Croston, J. H., & Goodger, J. L. 2013, MNRAS, 435, 3353

Harwood, J. J., Croston, J. H., Intema, H. T., et al. 2016, MNRAS, 458, 4443

Heckman, T. M., Ptak, A., Hornschemeier, A., & Kauffmann, G. 2005, ApJ, 634, 161

Heisler, C. A., Lumsden, S. L., & Bailey, J. A. 1997, Nature, 385, 700

Hernán-Caballero, A., & Hatziminaoglou, E. 2011, MNRAS, 414, 500

Hernández-García, L., González-Martín, O., Márquez, I., & Masegosa, J. 2013, A&A, 556, A47

HI4PI Collaboration, Ben Bekhti, N., Flöer, L., et al. 2016, A&A, 594, A116

Hickox, R. C., & Alexander, D. M. 2018, ARA&A, 56, 625

Hickox, R. C., Mullaney, J. R., Alexander, D. M., et al. 2014, ApJ, 782, 9

Hirschmann, M., Khochfar, S., Burkert, A., et al. 2010, MNRAS, 407, 1016

Ho, L. C., Darling, J., & Greene, J. E. 2008, ApJS, 177, 103

Ho, L. C., Filippenko, A. V., & Sargent, W. L. W. 1997, ApJS, 112, 315

Ho, L. C., Feigelson, E. D., Townsley, L. K., et al. 2001, ApJ, 549, L51

Hong, J., Im, M., Kim, M., & Ho, L. C. 2015, ApJ, 804, 34

Hopkins, P. F., Hernquist, L., Cox, T. J., & Kereš, D. 2008, ApJS, 175, 356

Hopkins, P. F., Hernquist, L., Hayward, C. C., & Narayanan, D. 2012, MNRAS, 425, 1121

Hopkins, P. F., & Quataert, E. 2010, MNRAS, 407, 1529

Hopkins, P. F., Torrey, P., Faucher-Giguère, C.-A., Quataert, E., & Murray, N. 2016, MNRAS, 458, 816

Hou, M., Liu, X., Guo, H., et al. 2019, ApJ, 882, 41

Huchra, J., & Burg, R. 1992, ApJ, 393, 90

Hughes, D. H., Appleton, P. N., & Schombert, J. M. 1991, ApJ, 370, 176

Hutchings, J. B., & Neff, S. G. 1989, AJ, 97, 1306

Ichikawa, K., & Tazaki, R. 2017, ApJ, 844, 21

Imanishi, M., Nakanishi, K., & Izumi, T. 2016, ApJ, 822, L10

Imanishi, M., & Terashima, Y. 2004, AJ, 127, 758

Ingram, A., & Done, C. 2011, MNRAS, 415, 2323

Ingram, A., Done, C., & Fragile, P. C. 2009, MNRAS, 397, L101

Isbell, J. W., Burtscher, L., Asmus, D., et al. 2021, ApJ, 910, 104

Ishibashi, W., & Fabian, A. C. 2016, MNRAS, 457, 2864

Jahnke, K., & Macciò, A. V. 2011, ApJ, 734, 92

Jansen, F., Lumb, D., Altieri, B., et al. 2001, A&A, 365, L1

Jones, M. L., Parker, K., Fabbiano, G., et al. 2021, ApJ, 910, 19

Ju, W., Greene, J. E., Rafikov, R. R., Bickerton, S. J., & Badenes, C. 2013, ApJ, 777, 44

Jun, H. D., Stern, D., Graham, M. J., et al. 2015a, ApJ, 814, L12

Jun, H. D., Im, M., Lee, H. M., et al. 2015b, ApJ, 806, 109

Just, D. W., Brandt, W. N., Shemmer, O., et al. 2007, ApJ, 665, 1004

Kaastra, J. S., & Roos, N. 1992, A&A, 254, 96

Kammoun, E. S., Miller, J. M., Koss, M., et al. 2020, ApJ, 901, 161

Kamraj, N., Brightman, M., Harrison, F. A., et al. 2022, ApJ, 927, 42

Kaspi, S., Maoz, D., Netzer, H., et al. 2005, ApJ, 629, 61

Kaspi, S., Smith, P. S., Netzer, H., et al. 2000, ApJ, 533, 631

Keck, M. L., Brenneman, L. W., Ballantyne, D. R., et al. 2015, ApJ, 806, 149

Keel, W. C., Chojnowski, S. D., Bennert, V. N., et al. 2012a, MNRAS, 420, 878

Keel, W. C., Lintott, C. J., Schawinski, K., et al. 2012b, AJ, 144, 66

Kelley, L. Z., Haiman, Z., Sesana, A., & Hernquist, L. 2019, MNRAS, 485, 1579

Khan, F. M., Capelo, P. R., Mayer, L., & Berczik, P. 2018, ApJ, 868, 97

Kharb, P., Lal, D. V., & Merritt, D. 2017, Nature Astronomy, 1, 727

King, A., & Nixon, C. 2015, MNRAS, 453, L46

King, A. R., Pringle, J. E., & Livio, M. 2007, MNRAS, 376, 1740

Kocsis, B., Haiman, Z., & Loeb, A. 2012a, MNRAS, 427, 2680

Kocsis, B., Haiman, Z., & Loeb, A. 2012b, MNRAS, 427, 2660

Komossa, S., Burwitz, V., Hasinger, G., et al. 2003, ApJ, 582, L15

Komossa, S., Grupe, D., Kraus, A., et al. 2023, MNRAS, 522, L84

Kormendy, J., & Ho, L. C. 2013, ARA&A, 51, 511

Koss, M., Mushotzky, R., Treister, E., et al. 2012, ApJ, 746, L22

Koss, M., Mushotzky, R., Treister, E., et al. 2011, ApJ, 735, L42

Koss, M., Trakhtenbrot, B., Ricci, C., et al. 2017, ApJ, 850, 74

Kraan-Korteweg, R. C. 1982, A&AS, 47, 505

Krause, M. G. H., Shabala, S. S., Hardcastle, M. J., et al. 2019, MNRAS, 482, 240

Krolik, J. H., Volonteri, M., Dubois, Y., & Devriendt, J. 2019, ApJ, 879, 110

Kun, E., Gabányi, K. É., Karouzos, M., Britzen, S., & Gergely, L. Á. 2014, MNRAS, 445, 1370

Kushwaha, P., Gupta, A. C., Wiita, P. J., et al. 2018, MNRAS, 479, 1672

Laine, S., Dey, L., Valtonen, M., et al. 2020, ApJ, 894, L1

LaMassa, S. M., Heckman, T. M., & Ptak, A. 2012, ApJ, 758, 82

LaMassa, S. M., Heckman, T. M., Ptak, A., et al. 2010, ApJ, 720, 786

LaMassa, S. M., Heckman, T. M., Ptak, A., et al. 2011, ApJ, 729, 52

LaMassa, S. M., Cales, S., Moran, E. C., et al. 2015, ApJ, 800, 144

Lehto, H. J., & Valtonen, M. J. 1996, ApJ, 460, 207

Lena, D., Robinson, A., Storchi-Bergman, T., et al. 2015, ApJ, 806, 84

Li, Y.-R., Wang, J.-M., Ho, L. C., et al. 2016, ApJ, 822, 4

Liao, W.-T., Chen, Y.-C., Liu, X., et al. 2021, MNRAS, 500, 4025

Lintott, C. J., Schawinski, K., Keel, W., et al. 2009, MNRAS, 399, 129

Lira, P., Videla, L., Wu, Y., et al. 2013, ApJ, 764, 159

Liu, R., Pooley, G., & Riley, J. M. 1992, MNRAS, 257, 545

Liu, T., Gezari, S., & Miller, M. C. 2018, ApJ, 859, L12

Liu, T., Gezari, S., Heinis, S., et al. 2015, ApJ, 803, L16

Liu, T., Gezari, S., Burgett, W., et al. 2016, ApJ, 833, 6

Liu, T., Gezari, S., Ayers, M., et al. 2019, ApJ, 884, 36

Liu, X., Shen, Y., Bian, F., Loeb, A., & Tremaine, S. 2014, ApJ, 789, 140

Liu, X., Shen, Y., & Strauss, M. A. 2011, ApJ, 736, L7

Lobanov, A. P., & Roland, J. 2005, A&A, 431, 831

Lobanov, A. P., & Zensus, J. A. 2001, Science, 294, 128

Lumsden, S. L., Heisler, C. A., Bailey, J. A., Hough, J. H., & Young, S. 2001, MNRAS, 327, 459

Luo, R., Woo, J.-H., Karouzos, M., et al. 2021, ApJ, 908, 221

Lusso, E., & Risaliti, G. 2016, ApJ, 819, 154

Lusso, E., Comastri, A., Vignali, C., et al. 2010, A&A, 512, A34

Lusso, E., Comastri, A., Vignali, C., et al. 2011, A&A, 534, A110

MacLeod, C. L., Ross, N. P., Lawrence, A., et al. 2016, MNRAS, 457, 389

Madsen, K. K., Harrison, F. A., Markwardt, C. B., et al. 2015, ApJS, 220, 8

Madsen, K. K., Harrison, F., Broadway, D., et al. 2018, in Society of Photo-Optical Instrumentation Engineers (SPIE) Conference Series, Vol. 10699, Space Telescopes and Instrumentation 2018: Ultraviolet to Gamma Ray, ed. J.-W. A. den Herder, S. Nikzad, & K. Nakazawa, 106996M

Mainzer, A., Bauer, J., Cutri, R. M., et al. 2014, ApJ, 792, 30

Makino, J., & Funato, Y. 2004, ApJ, 602, 93

Malkan, M. A., Jensen, L. D., Rodriguez, D. R., Spinoglio, L., & Rush, B. 2017, ApJ, 846, 102

Marconi, A., & Hunt, L. K. 2003, ApJ, 589, L21

Marconi, A., Risaliti, G., Gilli, R., et al. 2004, MNRAS, 351, 169

Marscher, A. P., & Jorstad, S. G. 2011, ApJ, 729, 26

Masini, A., Comastri, A., Baloković, M., et al. 2016, A&A, 589, A59

Matt, G., Guainazzi, M., & Maiolino, R. 2003, MNRAS, 342, 422

Mayer, L., Kazantzidis, S., Madau, P., et al. 2007, Science, 316, 1874

Mazzarella, J. M., Gaume, R. A., Soifer, B. T., et al. 1991, AJ, 102, 1241

McKernan, B., Ford, K. E. S., Kocsis, B., & Haiman, Z. 2013, MNRAS, 432, 1468

McNamara, B. R., Kazemzadeh, F., Rafferty, D. A., et al. 2009, ApJ, 698, 594

Mehdipour, M., Branduardi-Raymont, G., Kaastra, J. S., et al. 2011, A&A, 534, A39

Meléndez, M., Kraemer, S. B., & Schmitt, H. R. 2010, MNRAS, 406, 493

Menou, K., & Quataert, E. 2001, ApJ, 552, 204

Merloni, A., Predehl, P., Becker, W., et al. 2012, arXiv e-prints, arXiv:1209.3114

Merritt, D., & Ferrarese, L. 2001, MNRAS, 320, L30

Miller, B. P., Brandt, W. N., Schneider, D. P., et al. 2011, ApJ, 726, 20

Milosavljević, M., & Merritt, D. 2003, in American Institute of Physics Conference Series, Vol. 686, The Astrophysics of Gravitational Wave Sources, ed. J. M. Centrella, 201

Moran, E. C., Kay, L. E., Davis, M., Filippenko, A. V., & Barth, A. J. 2001, ApJ, 556, L75

Motta, S. E. 2016, Astronomische Nachrichten, 337, 398

Müller-Sánchez, F., Comerford, J. M., Nevin, R., et al. 2015, ApJ, 813, 103

Müller-Sánchez, F., Prieto, M. A., Hicks, E. K. S., et al. 2011, ApJ, 739, 69

Murphy, K. D., & Yaqoob, T. 2009, MNRAS, 397, 1549

Nandra, K., O'Neill, P. M., George, I. M., & Reeves, J. N. 2007, MNRAS, 382, 194

Nandra, K., & Pounds, K. A. 1994, MNRAS, 268, 405

Nasa High Energy Astrophysics Science Archive Research Center (Heasarc). 2014, HEAsoft: Unified Release of FTOOLS and XANADU, Astrophysics Source Code Library, record ascl:1408.004

Nehlig, F., Vollmer, B., & Braine, J. 2016, A&A, 587, A108

Netzer, H., & Laor, A. 1993, ApJ, 404, L51

Neugebauer, G., Habing, H. J., van Duinen, R., et al. 1984, ApJ, 278, L1

Nguyen, K., & Bogdanović, T. 2016, ApJ, 828, 68

Nguyen, K., Bogdanović, T., Runnoe, J. C., et al. 2019, ApJ, 870, 16

Noble, S. C., Mundim, B. C., Nakano, H., et al. 2012, ApJ, 755, 51

Novak, G. S., Ostriker, J. P., & Ciotti, L. 2011, ApJ, 737, 26

Oh, K., Yi, S. K., Schawinski, K., et al. 2015, ApJS, 219, 1

O'Neill, S., Kiehlmann, S., Readhead, A. C. S., et al. 2022, ApJ, 926, L35

Packham, C., Radomski, J. T., Roche, P. F., et al. 2005, ApJ, 618, L17

Pal, M., Kushwaha, P., Dewangan, G. C., & Pawar, P. K. 2020, ApJ, 890, 47

Pandey, J. C., & Singh, K. P. 2008, MNRAS, 387, 1627

Panessa, F., Bassani, L., Cappi, M., et al. 2006, A&A, 455, 173

Panessa, F., Bassani, L., de Rosa, A., et al. 2008, A&A, 483, 151

Parma, P., Murgia, M., Morganti, R., et al. 1999, A&A, 344, 7

Pfeifle, R. W., Satyapal, S., Manzano-King, C., et al. 2019a, ApJ, 883, 167

Pfeifle, R. W., Satyapal, S., Secrest, N. J., et al. 2019b, ApJ, 875, 117

Phillips, M. M., & Frogel, J. A. 1980, ApJ, 235, 761

Piana, O., Dayal, P., Volonteri, M., & Choudhury, T. R. 2021, MNRAS, 500, 2146

Pogge, R. W., Maoz, D., Ho, L. C., & Eracleous, M. 2000, ApJ, 532, 323

Pott, J.-U., Malkan, M. A., Elitzur, M., et al. 2010, ApJ, 715, 736

Qian, S. J., Britzen, S., Witzel, A., Krichbaum, T. P., & Kun, E. 2018, A&A, 615, A123

Radomski, J. T., Packham, C., Levenson, N. A., et al. 2008, ApJ, 681, 141

Rafikov, R. R. 2013, ApJ, 774, 144

Rafikov, R. R. 2016, ApJ, 827, 111

Ramos Almeida, C., & Ricci, C. 2017, Nature Astronomy, 1, 679

Remillard, R. A., & McClintock, J. E. 2006, ARA&A, 44, 49

Repetto, P., Faúndez-Abans, M., Freitas-Lemes, P., Rodrigues, I., & de Oliveira-Abans, M. 2017, MNRAS, 464, 293

Reuter, H. P., Sievers, A. W., Pohl, M., Lesch, H., & Wielebinski, R. 1996, A&A, 306, 721

Ricci, C., Ueda, Y., Koss, M. J., et al. 2015, ApJ, 815, L13

Ricci, C., Bauer, F. E., Treister, E., et al. 2016, ApJ, 819, 4

Ricci, C., Trakhtenbrot, B., Koss, M. J., et al. 2017a, ApJS, 233, 17

Ricci, C., Bauer, F. E., Treister, E., et al. 2017b, MNRAS, 468, 1273

Ricci, C., Kara, E., Loewenstein, M., et al. 2020, ApJ, 898, L1

Risaliti, G., Elvis, M., & Nicastro, F. 2002, ApJ, 571, 234

Risaliti, G., Maiolino, R., & Salvati, M. 1999a, ApJ, 522, 157

Risaliti, G., Bassani, L., Comastri, A., et al. 1999b, Mem. Soc. Astron. Italiana, 70, 73

Risaliti, G., Harrison, F. A., Madsen, K. K., et al. 2013, Nature, 494, 449

Rivers, E., Risaliti, G., Walton, D. J., et al. 2015, ApJ, 804, 107

Roberts, T. P., Schurch, N. J., & Warwick, R. S. 2001, MNRAS, 324, 737

Robrade, J., & Schmitt, J. H. M. M. 2005, A&A, 435, 1073

Rodriguez, C., Taylor, G. B., Zavala, R. T., et al. 2006, ApJ, 646, 49

Rodríguez-Ardila, A., Prieto, M. A., Mazzalay, X., et al. 2017, MNRAS, 470, 2845

Roedig, C., Krolik, J. H., & Miller, M. C. 2014, ApJ, 785, 115

Romero, G. E. 1995, Ap&SS, 234, 49

Ross, N. P., Ford, K. E. S., Graham, M., et al. 2018, MNRAS, 480, 4468

Rubinur, K., Das, M., & Kharb, P. 2019, MNRAS, 484, 4933

Rumbaugh, N., Shen, Y., Morganson, E., et al. 2018, ApJ, 854, 160

Runnoe, J. C., Cales, S., Ruan, J. J., et al. 2016, MNRAS, 455, 1691

Ruschel-Dutra, D., Pastoriza, M., Riffel, R., Sales, D. A., & Winge, C. 2014, MNRAS, 438, 3434

Rush, B., Malkan, M. A., Fink, H. H., & Voges, W. 1996, ApJ, 471, 190

Rush, B., Malkan, M. A., & Spinoglio, L. 1993, ApJS, 89, 1

Ryan, G., & MacFadyen, A. 2017, ApJ, 835, 199

Ryu, T., Perna, R., Haiman, Z., Ostriker, J. P., & Stone, N. C. 2018, MNRAS, 473, 3410

Saade, M. L., Stern, D., Brightman, M., et al. 2020, ApJ, 900, 148

Saglia, R. P., Opitsch, M., Erwin, P., et al. 2016, ApJ, 818, 47

Sanders, D. B., Soifer, B. T., Elias, J. H., Neugebauer, G., & Matthews, K. 1988, ApJ, 328, L35

Sandrinelli, A., Covino, S., Dotti, M., & Treves, A. 2016, AJ, 151, 54

Sartori, L. F., Schawinski, K., Koss, M. J., et al. 2018, MNRAS, 474, 2444

Satyapal, S., Dudik, R. P., O'Halloran, B., & Gliozzi, M. 2005, ApJ, 633, 86

Satyapal, S., Secrest, N. J., Ricci, C., et al. 2017, ApJ, 848, 126

Schawinski, K., Koss, M., Berney, S., & Sartori, L. F. 2015, MNRAS, 451, 2517

Schawinski, K., Urry, C. M., Simmons, B. D., et al. 2014, MNRAS, 440, 889

Schirmer, M., Diaz, R., Holhjem, K., Levenson, N. A., & Winge, C. 2013, ApJ, 763, 60

Schlafly, E. F., & Finkbeiner, D. P. 2011, ApJ, 737, 103

Schmelz, J. T., Baan, W. A., & Haschick, A. D. 1987, ApJ, 320, 145

Schmitt, H. R., Donley, J. L., Antonucci, R. R. J., et al. 2003, ApJ, 597, 768

Sesana, A., Haiman, Z., Kocsis, B., & Kelley, L. Z. 2018, ApJ, 856, 42

Sesana, A., Volonteri, M., & Haardt, F. 2007, MNRAS, 377, 1711

Severgnini, P., Cicone, C., Della Ceca, R., et al. 2018, MNRAS, 479, 3804

Shakura, N. I., & Sunyaev, R. A. 1973, A&A, 24, 337

Shemmer, O., Brandt, W. N., Netzer, H., Maiolino, R., & Kaspi, S. 2008, ApJ, 682, 81

Shen, Y., Liu, X., Loeb, A., & Tremaine, S. 2013, ApJ, 775, 49

Shen, Y., & Loeb, A. 2010, ApJ, 725, 249

Shi, J.-M., & Krolik, J. H. 2015, ApJ, 807, 131

Shi, J.-M., Krolik, J. H., Lubow, S. H., & Hawley, J. F. 2012, ApJ, 749, 118

Shin, J., Woo, J.-H., & Mulchaey, J. S. 2016, ApJS, 227, 31

Shu, X. W., Wang, J. X., Jiang, P., Fan, L. L., & Wang, T. G. 2007, ApJ, 657, 167

Shuder, J. M., & Osterbrock, D. E. 1981, ApJ, 250, 55

Smith, R. K., Brickhouse, N. S., Liedahl, D. A., & Raymond, J. C. 2001, ApJ, 556, L91

Soltan, A. 1982, MNRAS, 200, 115

Spinelli, P. F., Storchi-Bergmann, T., Brandt, C. H., & Calzetti, D. 2006, ApJS, 166, 498

Spinoglio, L., & Malkan, M. A. 1989, ApJ, 342, 83

Springel, V., Di Matteo, T., & Hernquist, L. 2005, ApJ, 620, L79

Steinborn, L. K., Dolag, K., Hirschmann, M., Prieto, M. A., & Remus, R.-S. 2015, MNRAS, 448, 1504

Stern, D., McKernan, B., Graham, M. J., et al. 2018, ApJ, 864, 27

Strickland, D. K., Heckman, T. M., Colbert, E. J. M., Hoopes, C. G., & Weaver, K. A. 2004, ApJS, 151, 193

Sturm, E., González-Alfonso, E., Veilleux, S., et al. 2011, ApJ, 733, L16

Tananbaum, H., Avni, Y., Branduardi, G., et al. 1979, ApJ, 234, L9

Tang, Y., Haiman, Z., & MacFadyen, A. 2018, MNRAS, 476, 2249

Temporin, S., Ciroi, S., Rafanelli, P., et al. 2003, ApJS, 148, 353

Terao, K., Nagao, T., Hashimoto, T., et al. 2016, ApJ, 833, 190

Terashima, Y., Ho, L. C., & Ptak, A. F. 2000, ApJ, 539, 161

Tombesi, F., Cappi, M., Reeves, J. N., et al. 2013, MNRAS, 430, 1102

Tommasin, S., Spinoglio, L., Malkan, M. A., & Fazio, G. 2010, ApJ, 709, 1257

Tomsick, J., & COSI Collaboration. 2022, in 37th International Cosmic Ray Conference, 652

Trakhtenbrot, B., Ricci, C., Koss, M. J., et al. 2017, MNRAS, 470, 800

Tran, H. D. 2001, ApJ, 554, L19

Treister, E., Privon, G. C., Sartori, L. F., et al. 2018, ApJ, 854, 83

Tremaine, S., & Davis, S. W. 2014, MNRAS, 441, 1408

Tsai, C.-W., Jarrett, T. H., Stern, D., et al. 2013, ApJ, 779, 41

Ulubay-Siddiki, A., Gerhard, O., & Arnaboldi, M. 2009, MNRAS, 398, 535

Valtonen, M. J., Ciprini, S., & Lehto, H. J. 2012, MNRAS, 427, 77

Valtonen, M. J., Lehto, H. J., Nilsson, K., et al. 2008, Nature, 452, 851

van Breugel, W., Filippenko, A. V., Heckman, T., & Miley, G. 1985, ApJ, 293, 83

van den Bosch, R. C. E. 2016, ApJ, 831, 134

Vaughan, S. 2012, Philosophical Transactions of the Royal Society of London Series A, 371, 20110549

Vaughan, S., Uttley, P., Markowitz, A. G., et al. 2016, MNRAS, 461, 3145

Véron-Cetty, M. P., & Véron, P. 2006, A&A, 455, 773

Véron-Cetty, M. P., & Véron, P. 2010, A&A, 518, A10

Videla, L., Lira, P., Andrews, H., et al. 2013, ApJS, 204, 23

Voges, W., Aschenbach, B., Boller, T., et al. 1999, A&A, 349, 389

Vollmer, B. 2009, A&A, 502, 427

Vollmer, B., Soida, M., Chung, A., et al. 2008, A&A, 483, 89

Volonteri, M., Haardt, F., & Madau, P. 2003, ApJ, 582, 559

Walton, D. J., Nardini, E., Fabian, A. C., Gallo, L. C., & Reis, R. C. 2013, MNRAS, 428, 2901

Walton, D. J., Roberts, T. P., Mateos, S., & Heard, V. 2011, MNRAS, 416, 1844

Walton, D. J., Risaliti, G., Harrison, F. A., et al. 2014, ApJ, 788, 76

Walton, D. J., Alston, W. N., Kosec, P., et al. 2020, MNRAS, 499, 1480

Wang, J., Xu, D. W., & Wei, J. Y. 2018, ApJ, 858, 49

Wang, L., Greene, J. E., Ju, W., et al. 2017, ApJ, 834, 129

Weinberger, R., Springel, V., Pakmor, R., et al. 2018, MNRAS, 479, 4056

Weisskopf, M. C., Brinkman, B., Canizares, C., et al. 2002, PASP, 114, 1

Wijnands, R., & van der Klis, M. 1999, ApJ, 514, 939

Wilkins, D. R., Kara, E., Fabian, A. C., & Gallo, L. C. 2014, MNRAS, 443, 2746

Wilms, J., Allen, A., & McCray, R. 2000, ApJ, 542, 914

Woo, J.-H., & Urry, C. M. 2002, ApJ, 579, 530

Wright, E. L., Eisenhardt, P. R. M., Mainzer, A. K., et al. 2010, AJ, 140, 1868

Xin, C., Charisi, M., Haiman, Z., et al. 2020, MNRAS, 496, 1683

Yan, S.-P., Ding, G.-Q., Wang, N., Qu, J.-L., & Song, L.-M. 2013, MNRAS, 434, 59

Yang, G., Brandt, W. N., Alexander, D. M., et al. 2019, MNRAS, 485, 3721

Yaqoob, T. 2012, MNRAS, 423, 3360

Younes, G., Porquet, D., Sabra, B., Reeves, J. N., & Grosso, N. 2012, A&A, 539, A104

Yu, Q., & Tremaine, S. 2002, MNRAS, 335, 965

Yuan, T. T., Kewley, L. J., & Sanders, D. B. 2010, ApJ, 709, 884

Zamorani, G., Henry, J. P., Maccacaro, T., et al. 1981, ApJ, 245, 357

Zhang, J. S., Henkel, C., Kadler, M., et al. 2006, A&A, 450, 933

Zhang, W. M., Soria, R., Zhang, S. N., Swartz, D. A., & Liu, J. F. 2009, ApJ, 699, 281

Zhang, X., Wright, M., & Alexander, P. 1993, ApJ, 418, 100

Zhu, X.-J., & Thrane, E. 2020, ApJ, 900, 117

Zoghbi, A., Fabian, A. C., Reynolds, C. S., & Cackett, E. M. 2012, MNRAS, 422, 129

Zubovas, K., & Bourne, M. A. 2017, MNRAS, 468, 4956